ABSTRACT

Title of Dissertation:	EXPLORING BEYOND STANDARD MODEL PHYSICS WITH COSMOLOGICAL AND TERRESTRIAL PROBES
	Saurav Das Doctor of Philosophy, 2023
Dissertation Directed by:	Professor Anson Hook Department of Physics

The standard model for particle physics has been extremely successful as a description of nature. Despite this success, there remain many unsolved puzzles both observationally and theoretically. In this thesis we explore a few ideas in search of beyond the standard model physics, especially we focus on the Higgs mass, magnetic monopole and vector dark matter.

In the first part of the thesis, we show that the Goldstone bosons of discrete symmetry can be parametrically lighter than otherwise expected. While non-linear realizations of continuous symmetries feature derivative interactions and have no potential, non-linear realizations of discrete symmetries feature non-derivative interactions and have a highly suppressed potential. These Goldstone bosons of discrete symmetries have a non-zero potential, but the potential generated from quantum corrections is inherently very highly suppressed. We explore various discrete symmetries and to what extent the potential is suppressed for each of them.

In the second part, we showed that in the early universe, evaporating black holes heat up the surrounding plasma and create a temperature profile around the black hole that can be

more important than the black hole itself. As an example, we demonstrate how the hot plasma surrounding evaporating black holes can efficiently produce monopoles via the Kibble-Zurek mechanism. In the case where black holes reheat the universe, reheat temperatures above ~ 500 GeV can already lead to monopoles overclosing the universe.

In the last part of the thesis, we showed that vector Dark Matter (VDM) that couples to lepton flavor (L_e, L_μ, L_τ) acts similarly to a chemical potential for the neutrino flavor eigenstates and modifies neutrino oscillations. VDM imparts unique signatures such as time and directional dependence with longer baselines giving better sensitivity. We use the non-observation of such a signal at Super-Kamiokande to rule out the existence of VDM in a region of parameter space several orders of magnitude beyond other constraints and show the projected reach of future experiments such as DUNE.

Exploring Beyond Standard Model physics with cosmological and terrestrial probes

by

Saurav Das

Dissertation submitted to the Faculty of the Graduate School of the
University of Maryland, College Park in partial fulfillment
of the requirements for the degree of
Doctor of Philosophy
2023

Advisory Committee:
Professor Anson Hook, Chair/Advisor
Professor Kaustubh Agashe
Professor Zackaria Chacko
Professor Kara Hoffman
Professor Richard Wentworth

Dedication

To my parents, Dipak Kumar Das and Kalpana Das, and all my family members.

Acknowledgments

The journey through the last few years has been only possible due to support of my colleagues, friends and family.

I would like to thank my advisor Prof. Anson Hook. He has been patient with my work and has endured many of my ideas, however foolish they may have been.

I would like to thank Prof. Kaustubh Agashe, for his support in my work and career in general. My interaction with him has always been comforting, especially during the most difficult times.

I would like to thank my other collaborators. My collaboration with Dr. Gustavo Marques Tavares has been exceptionally productive. I would like to thank Edward Broadberry, Dawid Brzeminski, Clayton Ristow and Sagar Airen for their collaboration and discussions.

I would like to thank Prof. Zackaria Chacko, Prof. Kara Hoffman and Prof. Richard Wentworth for agreeing to be on my dissertation committee and for useful feedback on this thesis.

I would like to thank other members of the EPT group, whose discussion and vigorous enthusiasm for physics I have enjoyed. In this regard I would like to thank Prof. Raman Sundrum, Prof. Zackaria Chacko, Prof. Rabindra Mohapatra, Prof. Kieth Dienes, Prof. Drew Baden, Yushin Tsai, Zhen Liu, Michael Geller, Manuel A. Buen-Abad, Jae Hyeok Chang, Peizhi Du, Soubhik Kumar, Majid Ekhterachian, Abhish Dev, Arushi Bodas, Deepak Sathyan, Reza Ebadi, Ina Flood.

The past six years have enriched my life in many different ways. This journey would be impossible without Sohitri Ghosh and her help. The driving lessons, countless hikes and fun evenings were the highlights of this period. I would like to thank Tamoghna Barik, Arinjoy De, Aravind Ravi, Abu Saleh Musa Patoary, Amitava Banerjee, Gautam Nambiar, Amit Anand, Aritra Das, Arghya Sadhukhan, Naren Manjunath, Subhayan Sahu, Anshuman Swain, Prakhar Gupta, Xiaozhen Fu, Jessica Bodosa, Saurabh Kadam, Jeet Shah, Navya Gupta, Kanika Kalra, Srilekha Gandhari, Aniruddha Bapat, Amit Nag, Swarnav Banik, Sabyasachi Barik, Subhojit Dutta and many other friends I will miss dearly.

One of my cherished memories from UMD will be intramural soccer tournaments. I would like to thank Majid Ekhterachian, Stefano Antonini, Masoud Mohammadi Arzanagh, Martin Ritter, Joseph Hart, Rahul Gaur, Tornike Ghutishvili, Landry Horimbere and many other teammates during the past six years for that.

I would like to thank my friends from college and school whose random chats have kept me sane. In this regard, I would like to thank Sohitri Ghosh, Aravind Ravi, Spandan Pathak, Kishalay Mahato, Rajat Roy, Arunav Bordoloi, Sanchita Pal, Shibajyoti Das, Rahul Kumar, Koushik Bar, Amit Bera, Abhinava Chatterjee, Antarikha Das, Riya Samanta, Payel Mukhopadhaya, Nabarun Gupta, Sohail Ahasan, Rounak Meyur.

Above all, I would like to thank my parents, my brother and all other extended family members, without them to share my happiness with, all this would be futile.

Table of Contents

List of Tables

List of Figures

Chapter 1: Introduction

1.1 Success of the Standard Model

The Standard Model (SM) has been extremely successful as a fundamental theory of nature. The predictions of SM has been verified to incredible accuracy over many orders of energy scale.

SM is a Gauge theory with $SU(3)_C \times SU(2)_L \times U(1)_Y$ gauge symmetry. The $SU(3)_C$ describes the symmetry of the strong interaction. On the other hand, $SU(2)_L \times U(1)_Y$ corresponds to the electroweak interaction. At low energies, the electroweak symmetry is broken spontaneously by the vacuum expectation value of the Higgs field. Higgs is a scalar SU(2) doublet. After spontaneous symmetry breaking (SSB), among the four degrees of freedom of the Higgs field, three provides mass to the Weak gauge fields, $W^{\pm}$ and Z boson and the remaining one becomes the physical Higgs field. Only the subgroup $U(1)_{EM}$ survives the SSB and manifests itself in the form of electromagnetic interaction mediated by the massless photon.

If we assume neutrinos to be massless, the Standard Model can be described by nineteen free parameters. The mass of the nine fermions (3 leptons and six quarks), four parameters in the CKM matrix (three mixing angles and CP violating phase), three coupling constants corresponding to the three gauge groups, Higgs vev, Higgs mass and QCD vacuum angle. Once we consider these parameters as input, we can predict all other physical quantities to great accuracy. The poster child of this success has been the gyromagnetic ratio of an isolated electron, which has been calculated up to twelve [16, 17, 18] significant figures.

In spite of this great success, there are both experimental observations and theoretical arguments that suggest that SM may not be a complete theory of nature. For example, the neutrino was assumed to be massless in the original formulation of SM. The observation of neutrino oscillations conclusively proves that neutrinos have small, albeit non-zero, mass. Moreover, from cosmological and astrophysical observations spanning over a multitude of lengthscales, we know that the dominant gravitating matter in the universe is the Dark Matter (DM), a cold and collisionless matter that interacts extremely weakly with SM. Since SM doesn't have any suitable candidate for DM (with the exception of primordial black holes), DM is guaranteed to be some species beyond Standard Model (BSM). There exist other reasons to believe that the standard model is not an absolute theory of nature and we need to search for its modifications both theoretically and experimentally. We will discuss a few of them next, including the 'Little Hierarchy Problem' and magnetic monopoles.

1.2 The little Hierarchy problem

Apart from the various observations like neutrino oscillations and the existence DM, there are other hints within the theoretical framework of SM that indicate it is perhaps incomplete. One of the strongest such indications comes from the Higgs mass. The Higgs boson is a scalar in the SM. The mass of a scalar field is not protected by any symmetry and receives quantum corrections from all other fields it interacts with. For example, the top loop provides a quantum correction to the Higgs mass squared [1] $\sim (-)\frac{3}{8\pi^2}\lambda_t^2\Lambda^2$, where λ_t is the Higgs and the top quark coupling and Λ is the scale parametrically at which new physics should appear. Since Higgs couples to all the quarks and leptons in the Standard Model, the Higgs mass is sensitive to all those couplings. If we assume that new physics appears at the Grand Unified Theory (GUT) scale, roughly around 10^{14} GeV, then the Higgs mass squared should naturally be expected around $|m_H^2| \sim 10^{28}\text{GeV}^2$. But the observed m_H^2 is smaller by a rough factor of 10^{24}. This extreme precise cancellation, roughly 1 part in 10^{24} is dubbed the 'Little Hierarchy Problem'. Sometimes the same problem is stated as the smallness of the Electroweak scale relative to Planck scale or GUT scale.

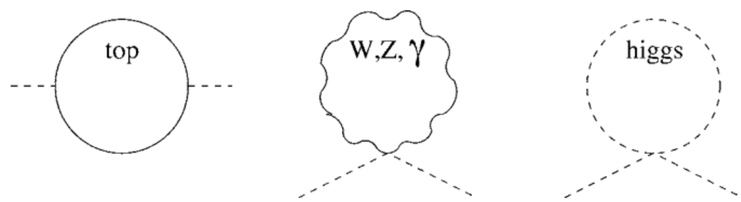

Figure 1.1: Most significant quadratic contributions to the Higgs potential in the standard model [1].

The various proposed resolutions of the 'Little Hierarchy Problem' can be divided into two main categories. One of them is the extra dimensional solution, in which either of the scales (the Weak scale or the Planck scale) is assumed to be the fundamental one and some additional dynamics in the extra dimension(s) produces the other one. Some of the most well known examples of this paradigm are the RS model [19, 20] and Large extra dimensions [21, 22, 23].

The other main category for the resolution of the 'Little Hierarchy Problem' is to invoke additional symmetry under which the Higgs is a pseudo-Goldstone. The Higgs is protected from the quadratic corrections due to enhanced symmetry. If the new symmetry was exact, the Higgs would be completely massless. The mass of the Higgs then arises from the small breaking of the enhanced symmetry and is thus naturally much smaller than expected from the naive quadratic quantum corrections. The examples of this principle is manifested in the Little Higgs [1, 24, 25] and twin Higgs [26] theories, among many.

1.3 Magnetic monopoles

Magnetic monopoles are generic predictions of modifications of the Standard Model (like GUT theories). Although we haven't experimentally observed their existence yet, they are nonetheless extremely interesting.

The source free Maxwell equations are symmetric in electric and magnetic field. However, that symmetry is broken by the fact that we haven't observed a magnetic monopole unlike electrically charged particles. That fact is reflected in the definition of vector potential $\vec{A}$. As the magnetic field is given by $\vec{B} = \nabla \times \vec{A}$, the magnetic field is source free, $\nabla \cdot \vec{B} = 0$. However, it is possible to define a vector potential that describes an effective magnetic monopole [27].

$$\vec{A}(\vec{r}) = \frac{g}{4\pi|\vec{r}|} \frac{\vec{r} \times \hat{n}}{|\vec{r}| - \vec{r} \cdot \hat{n}} \tag{1.1}$$

The magnetic field created by the above vector potential is well defined everywhere apart from along $\hat{n}$.

$$\vec{B}(\vec{r}) = \frac{g}{4\pi} \frac{\vec{r}}{|\vec{r}|^3} \qquad \hat{r} \neq \hat{n} \tag{1.2}$$

This can be thought of as an infinitely long thin solenoid along $\hat{n}$ which emanates a magnetic charge from its end as shown in Fig. 1.2.

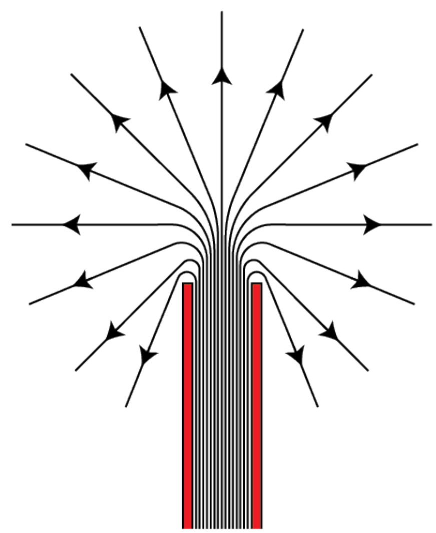

Figure 1.2: Schematic diagram of a Dirac magnetic monopole.

Although classically it will be impossible to observe such a string, quantum mechanics will not be insensitive to its existence. In an Aharonov-Bohm experiment, a charged particle will acquire a phase when moving around the string. However, the existence of the string will not affect the interference pattern if the phase accumulated by the charged particles' wavefunction is a multiple of 2π. That would mean that the electric charge can only take values e such that

$$\frac{ge}{2\pi} \in \mathbb{Z} \tag{1.3}$$

which will imply that electric charge is quantized. Thus, Dirac showed that quantum mechanics is compatible with magnetic monopoles and its existence will provide an explanation for electric charge quantization.

Later t'Hooft [28] and Polyakov [29] showed that under certain general assumption about symmetries of quantum electrodynamics, magnetic monopoles are essential (please refer to [27, 30] for excellent reviews). Consider a model with an $SU(2)$ gauge group and a Higgs field Φ in the triplet representation

$$\mathcal{L} = -\frac{1}{4}F^a_{\mu\nu}F^{\mu\nu a} + \frac{1}{2}D_\mu\Phi^a D^\mu\Phi^a - U(\Phi) \tag{1.4}$$

where the potential $U(\Phi) = \frac{1}{8}(\Phi^a\Phi^a - v^2)^2$ has a classical minimum at $|\Phi| = v$ and $D_\mu\Phi^a$ and $F^a_{\mu\nu}$ are the non abelian gauge covariant derivative and gauge field strength respectively. The classical vacuum of the theory is a zero energy solution in which the potential energy is zero and all the gradient energies also vanish. In the unitary gauge, such a solution can be written as

$$\Phi = (0, 0, v + H), \quad H = 0, \quad W^a_\mu = 0 \tag{1.5}$$

The perturbative spectrum of the theory consists of massive gauge bosons $W_\pm$ and Higgs field H with $M_W = ev$ and $M_H = \sqrt{\lambda}v$ respectively. The gauge field W^3_μ remains massless and acts as the mediator for electromagnetism. However, apart from the vacuum solution, there exists other time independent classical solutions. For example the 'hedgehog' solution

$$\phi^a(r) = vf(M_W r)\hat{r}^a \tag{1.6}$$

For continuity, the function f has to vanish at the origin $f(0) = 0$ and for the scalar Φ to approach the vacuum, $\Phi^a\Phi^a = v^2$ at a distance, we need $f(\infty) = 1$. It is clear that the field wraps around the origin, as shown in the Fig 1.3. Therefore it is impossible to deform it in a continuous way to match with the vacuum solution since continuous deformations preserve the 'winding number'.

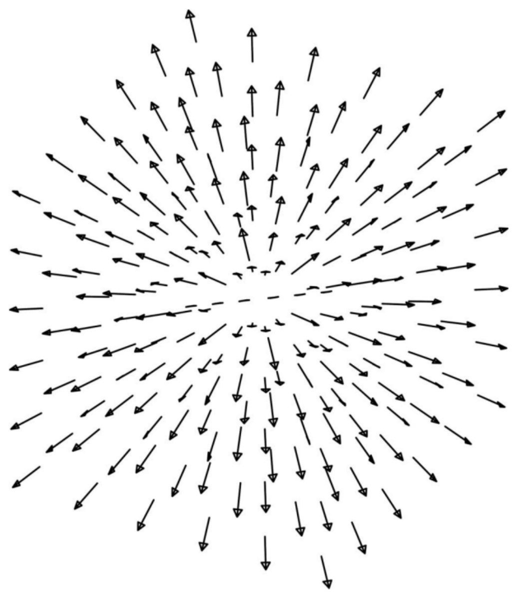

Figure 1.3: The Hedgehog configuration of the magnetic monopole. The scalar field always points away from the origin. It is impossible to continuously deform it to the vacuum solution. Image from [2].

The total energy of the configuration will be finite only if far away from the origin, the gauge fields cancel the gradient of the scalar. Hence for large r, $D_\mu \Phi^a \sim 0 \implies W^a_\mu \sim \frac{\epsilon_{\mu a k} \hat{r}^k}{er}$. Hence we can write

$$W^a_\mu = \frac{\epsilon_{\mu a k} \hat{r}^k}{er} (1 - g(M_W r)) \tag{1.7}$$

where the function g follows the asymptotic behavior $g(0) = 1$ and $g(\infty) = 0$. In general, the exact solution for the functions f and g need to be found numerically. However, we can simply observe that since g asymptotes to a fixed value, the gauge fields excitations are limited within some radius r_c. The radius r_c has to be selected so that the total energy of the configuration, the gradient of the scalar inside and magnetic field energy outside, is minimum. From that we get

$$r_c \sim \frac{1}{M_W} \tag{1.8}$$

which is understood to be classical radius of the magnetic monopole. On the other hand, the classical mass of the monopole is simply the energy stored within the configuration of radius r_c, which is

$$m = \frac{4\pi}{e^2} M_W \tag{1.9}$$

This means that the size of the monopole is $4\pi/e^2 = 1/\alpha$ times its Compton wavelength. So the GUT monopole can be thought of as a classical object or a coherent superposition of quantum states.

Since black holes radiate only thermal radiation, the production rate of magnetic monopoles from Hawking radiation will be extremely small, perhaps exponentially suppressed due to their coherent nature. We can quantify this suppression by means of calculating grey body factor of an extended object in Hawking radiation. The following discussion roughly follows [31]

$$P(\omega) = \sigma(\omega) \frac{\omega^3}{(2\pi)^3} \frac{1}{\exp\left(\omega/k_B T\right) - 1} \tag{1.10}$$

where P is the power radiated per unit solid angle per unit frequency, ω denotes the frequency and σ denotes grey body factor. The grey body factor for an extended object like a GUT monopole can be numerically estimated starting from the tunneling action responsible for Hawking radiation. Under semiclassical approximation, the effective action for a pure radial motion in Schwarzschild metric can be written as

$$S = -\int d\tau \left(m + c\frac{6M^2}{M_P^4 r^6} \left(\left(1 - \frac{2M}{M_P^2 r}\right) \dot{t}^2 - \dot{r}^2 - 2\dot{t}\dot{r}\sqrt{2M/M_P^2 r} \right)^2 \right) \tag{1.11}$$

where M is the effective mass of the Schwarzschild BH, m is the mass of the species under consideration and $\dot{x}$ denotes derivative of x w.r.t. proper time τ. The second term with coefficient c can be interpreted as tidal effects. For a point object, $c = 0$. For a non-gravitational extended object, like magnetic monopole, it is expected that $c \sim d^3$ where d is the physical size of the object. Thus the resulting grey body factor is numerically found to be exponentially suppressed for large ratios of size

$$\sigma \sim \exp\left(-\frac{d^3 M_p^6}{\alpha M^3}\right) \tag{1.12}$$

where $\alpha \approx 3.3$ is found numerically for low mass emission, $mM/M_p^2 \ll 1$.

This can also be seen as an exponential in the ratio of the size of the object to the size of the black hole (BH). It is then clear that for any extended object, for example a proton, emission via Hawking radiation is extremely small. When the mass (size) of the BH is large, its temperature is small and the emission is Boltzmann suppressed. On the other hand, when the mass(size) of the BH is small enough that the emission is not Boltzmann suppressed, $\frac{d^3 M_p^6}{\alpha M^3} \sim (2\pi)^3/\alpha$, the emission is size suppressed. For a GUT monopole where the size is larger than the Compton wavelength, this effect is even more pronounced.

In chapter 3, we will discuss a novel way in which a BH can produce extended objects like a magnetic monopole.

1.4 Neutrinos

Neutrinos only interact with the rest of the Standard Model via the Weak interaction (and gravity). Since neutrinos are so weakly interacting in the standard model, they are an extremely interesting source of exotic physics. Neutrinos were first proposed by Pauli to explain the missing energy and momentum from nuclear β-decay. The first neutrinos to be detected were electron neutrinos, in 1956. Since then we have detected muon and tau neutrinos, the other two weak flavor neutrino eigenstates.

Neutrinos are copiously produced in the extreme astrophysical environments, like in the core of the sun and supernovae. But since neutrinos rarely interact on their way out to us, they can reveal important information about interesting astrophysics. By the same token, since neutrinos rarely interact with matter from their source of creation to the point of detection, any change in their spectrum can reveal new BSM physics.

In the SM, the neutrino was assumed to be massless. But neutrino oscillation implies that neutrinos have different masses. So all the neutrino masses can't be zero. Neutrino oscillation can be described by the time evolution of the flavor eigenstates

$$|\nu_\alpha\rangle = \sum_i U_{\alpha i}|\nu_i\rangle \tag{1.13}$$

where ν_α and ν_i denote the neutrino flavor and mass eigenstates respectively and U denotes the Unitary transformation between two bases. The wavefunction evolves according to the Schrodinger equation. If the mass eigenstates have different masses, then the different mass eigenstates acquire different phases which interfere with each other.

$$|\nu_\alpha(t)\rangle = \sum_i U_{\alpha i}|\nu_i(t)\rangle \tag{1.14}$$

After the free evolution, the neutrino state can then undergo a charged current interaction with a lepton, and the corresponding probability is given by

$$P_{\alpha\beta} = |\langle\nu_\beta|\nu_\alpha(t)\rangle|^2 = |\sum_{i,j} U_{\alpha i}U^*_{\beta j}\langle\nu_j|\nu_i(t)\rangle|^2 \tag{1.15}$$

If we assume the neutrino wavefront can be approximated as a plane wave, then

$$|\nu_j(t)\rangle = e^{-iE_j t}|\nu_j(0)\rangle = e^{-i\sqrt{p_j^2+m_j^2}t}|\nu_j(0)\rangle \tag{1.16}$$

For a highly relativistic neutrino, to leading order, $\sqrt{p_j^2+m_j^2} \approx p + \frac{m_j^2}{2p} \approx E + \frac{m_j^2}{2E}$. A simple example is to consider the two neutrino case (which is a very good approximation in some cases due to the fact that two of the masses are very close and θ_{23} is extremely small), the transition probability reads

$$P_{12} = \sin^2 2\theta \sin^2\left(\frac{\Delta m^2 L}{4E}\right) \tag{1.17}$$

where θ is the rotation angle in the 2×2 unitary matrix, $\Delta m^2 = m_2^2 - m_1^2$ is the neutrino mass squared difference and L is the neutrino path length.

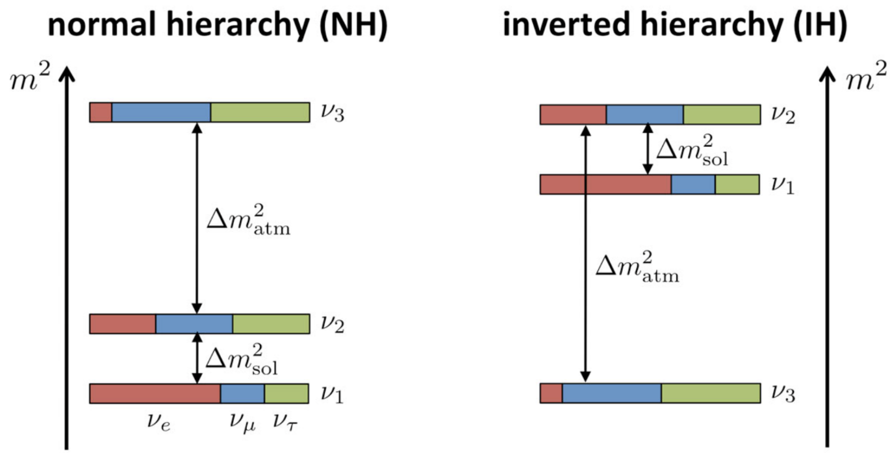

Figure 1.4: Normal and inverted neutrino mass Hierarchy, courtesy to JUNO collaboration

From the neutrino oscillation in vacuum, we can only infer the squared differences in the neutrino masses. From measurement of neutrino oscillations, we know that two of the neutrino masses are relatively close, $m_2^2 - m_1^2 = 7.39 \times 10^{-5}\text{eV}^2$, whereas the third neutrino mass is well separated from the other two $m_3^2 - m_2^2 = \pm 2.5 \times 10^{-3}\text{eV}^2$. That allows neutrino masses to be arranged in two different orders. One is termed the "Normal mass hierarchy" in which m_3 is the largest, whereas in the "Inverted mass Hierarchy" , m_3 is the smallest, as shown in Fig. 1.4. On the other hand, cosmological probes, which are sensitive to only the gravitational effects of neutrinos, can probe the sum of neutrino masses [32, 33]. However, in various Earth based experiments, it is possible to observe the effects of different mass hierarchies. Since neutrinos travel through the earth, which acts as a chemical potential for electron neutrinos [34, 35] (and oppositely for anti-neutrinos), and electron neutrinos overlap unequally with different mass eigenstates (Fig 1.4) , the chemical potential pushes the effective mass splitting into opposite directions. Existing [36, 37, 38] and upcoming [39] neutrino experiments can distinguish between the different hierarchies.

Since neutrino oscillations are so precisely measured, and the oscillation is predominantly set by the vacuum oscillation parameter, $\frac{\Delta m^2}{4E} \approx 10^{-13} eV \left(\frac{GeV}{E}\right)$, neutrino oscillations can be a probe of BSM physics. The new physics is very often discussed in terms of model independent probes like neutrino non standard interactions (NSI) [40, 41] or Lorentz Violation (LV) [42, 43]. However, it is also imperative to consider dark matter that can be imprinted on the neutrino oscillation [44, 45, 46, 47, 48]. A particularly simple example [49] is that of a scalar DM that interacts with neutrino via

$$\mathcal{L}_{\text{int}} = y_{\alpha\beta}\phi(\nu^{\alpha})^T \nu^{\beta} \tag{1.18}$$

where $y_{\alpha\beta}$ is the yukawa coupling, ϕ is the scalar DM and ν denotes SM neutrino flavor states. For a light DM particle, ϕ can be treated as a classical background, which alters the effective neutrino mass

$$\hat{m} = \hat{m}_0 + \hat{y}\phi \tag{1.19}$$

where $\hat{m}$ is the neutrino mass matrix and $\hat{y}$ denotes the yukawa matrix. The oscillating scalar background

$$\phi = \phi_0 \cos(m_\phi t) + \mathcal{O}(v_{DM}) \tag{1.20}$$

creates an oscillation in both neutrino mass squared difference and neutrino mixing angle. The resulting change in the neutrino oscillation can be probed using neutrino experiments. Although the mass induced by DM can potentially make neutrinos non relativistic early in the cosmic history for large couplings, since the galactic DM density in the solar neighbourhood is roughly 10^6 times larger than the homogeneous density, there is a large DM parameter space that can be probed in neutrino experiments without making neutrinos non relativistic during Big Bang Nucleosynthesis (BBN) or last scattering.

1.5 Outline of Thesis

In Chap. 2, we present a new way of producing a scalar that is lighter than expected from the dimensional analysis arguments. We will see that for Goldstone bosons of discrete symmetries, the quadratic divergence necessarily cancels and the contribution to the potential only originates at higher order. We show that this construction can be generalized from the abelian case [50] to the non abelian scenario.

In Chap. 3, we show that although Hawking radiation can not directly produce magnetic monopoles, evaporation of a BH in the early universe can. BH can heat up the surrounding plasma to an extremely high temperature so that a broken symmetry can be restored in that region. After the evaporation of the BH is complete, the plasma cools down and the restored symmetry gets broken again. If this symmetry breaking proceeds through a second order phase transition, the Kibble-Zurec mechanism can produce significant number of magnetic monopoles, or any other topological defects. We further show that if the reheating of the universe was dominated by primordial BHs, the number of magnetic monopoles produced in this way could be significant and can potentially overclose the universe.

In Chap. 4, we show that neutrino experiments can probe into yet unexplored part of vector dark matter parameter space. We show that vector DM that gauges either of the lepton number differences creates an effective chemical potential for the neutrinos that alter neutrino oscillation pattern compared to standard oscillations. Although this chemical potential is oscillating in time, the time averaged effect of the oscillation does not vanish. We use the non observation of such effects in existing neutrino experiments to put new bounds on viable DM parameter space. We also project sensitivity of future neutrino experiments to these effects.

Chapter 5 provides the conclusion to the thesis.

Chapter 2: Non-linearly realized discrete symmetries

This work was done in collaboration with Anson Hook and is published in J. High Energy. Phys. 2020, 71 (2020).

2.1 Overview

Non-linear realizations of continuous symmetries, Nambu Goldstone bosons (NGBs), often appear in particle physics models. Perhaps the most famous example of a pseudo-Nambu Goldstone boson (pNGB) appears in the Standard Model and is the pion. Exact Goldstone bosons are highly constrained by their continuous shift symmetry so that they are derivatively coupled and do not have a potential. Goldstone bosons are interesting objects and there exists a vast literature studying them [51, 52, 53, 54, 55, 56, 57, 58, 59, 60, 61, 62, 63].

While interesting in their own right, the symmetries of a Goldstone boson are often too restrictive to be useful and they are often made into pNGBs by explicitly breaking their exact shift symmetry. The breaking of the exact shift symmetry can reintroduce unwanted features such as a large mass term, typically referred to as the Hierarchy Problem. Unsurprisingly, many of the features discussed below will have analogues with various solutions to the Hierarchy problem that we will only briefly touch upon, as there exists a whole class of models where the Higgs is a pNGB [64, 65, 66, 67, 68].

In addition to solutions to Hierarchy problems, discrete symmetries are also ubiquitous in models of flavor, see e.g. Refs. [3, 69, 70] and references therein. These flavor models use group theoretic properties to explain various observed properties of the quark and lepton mass matrices. These models typically involve spontaneous breaking of the discrete symmetries, leading to their non-linear realizations. The results discussed in this paper will help explain features such as anomalously light scalars that appear in these models.

In this article, we initiate a study of the non-linear realizations of discrete symmetries, objects we dub "discrete" NGBs. We find that discrete NGBs combine the best features of both exact Goldstone bosons and ordinary NGBs. On one hand, discrete NGBs can have large $\mathcal{O}(1)$ Yukawa couplings. On the other hand, the potential radiatively generated from these Yukawa couplings is typically very highly suppressed. These features can all be understood in the simplest example of a non-linear realization of the abelian discrete symmetry $\mathbb{Z}_N$, which we now briefly review [50].

A non-linearly realized $\mathbb{Z}_N$ features a periodic scalar π_0 with a period $2\pi f$ so that $\pi_0 = \pi_0 + 2\pi f$. Under the $\mathbb{Z}_N$ symmetry, π_0 transforms as

$$\frac{\pi_0}{f} \to \frac{\pi_0}{f} + \frac{2\pi}{N}.$$

Like Goldstone bosons and pNGBs, it is useful to exponentiate the scalar to obtain a field that transforms linearly under the $\mathbb{Z}_N$ symmetry. In this case, we introduce the field $\phi = f e^{i\pi_0/f}$ that transforms as $\phi \to e^{2\pi i/N}\phi$ under the $\mathbb{Z}_N$ symmetry. To see that π_0 should have a suppressed potential, we simply need write down the leading order term in its potential. Most of the first terms one can write preserve an accidental $U(1)$ symmetry and do not give π_0 a mass. The leading order analytic piece that can give a mass to π_0 can easily be seen to be

$$V \sim \phi^N$$

To generate a potential, one must first generate the operator ϕ^N. If the Yukawa coupling appears as $y\phi$, then each ϕ is accompanied by a Yukawa coupling so that the mass term generated must scale as y^N. Thus, as long as $y < 1$, the potential is exponentially suppressed in large N limit.

To see this explicitly, we couple a set of N fermions to π_0 in a $\mathbb{Z}_N$ symmetric manner. We introduce N fermions $\psi_1 \cdots \psi_N$ that are exchanged cyclically under the $\mathbb{Z}_N$ symmetry, $\psi_1 \to \psi_2 \to \psi_3 \cdots \psi_N \to \psi_1$. The leading order yukawa coupling that can be written is

$$\sum_{j=1}^{N} \left(m_\psi + \frac{y}{2} e^{i\left(\frac{2\pi j}{N} - \frac{\pi}{2}\right)} \phi + \frac{y}{2} e^{-i\left(\frac{2\pi j}{N} - \frac{\pi}{2}\right)} \phi^\dagger \right) \psi_j \psi_j^c = \sum_{j=1}^{N} \left(m_\psi + yf \sin\left(\frac{\pi_0}{f} + \frac{2\pi j}{N} \right) \right) \psi_j \psi_j^c,$$

where we have taken the Yukawa coupling y to be real. From this, one can calculate the one-loop Coleman Weinberg potential of π_0 and find that the leading order contribution scales as

$$V(\pi_0) \sim m_\psi^4 \left(\frac{yf}{m_\psi} \right)^N \cos\left(\frac{N\pi_0}{f} \right).$$

As expected from the general arguments given before, we see that the potential is suppressed by y^N. The proper expansion parameter is (yf/m_ψ) as opposed to y as one is simply doing a Taylor series of the fermion mass

$$m_{\psi,j}(\pi_0) = m_\psi \left(1 + \frac{yf}{m_\psi} \sin\left(\frac{\pi_0}{f} + \frac{2\pi j}{N} \right) \right).$$

Thus we see that if the expansion parameter is small, then as N increases, $\mathbb{Z}_N$ becomes an exponentially good approximation to a $U(1)$ and the corresponding discrete NGB mass goes to zero exponentially quickly [1]. From this simple example, it can be seen that non-linear realizations of discrete symmetries can feature amazing cancellations that result in highly suppressed potentials.

In this article, we will study non-linear realizations of non-abelian discrete symmetries and to what extent their discrete NGBs have their potentials suppressed. Discrete NGBs of non-abelian discrete symmetries have many of the same features of as their abelian cousins. As with the abelian case, the crucial point in determining how suppressed the potential is, is to determine the dimension of the operator which gives the discrete NGBs a mass.

When considering continuous non-abelian Lie groups, one must specify the breaking pattern in order to determine the number of Goldstone bosons or equivalently one must specify the representation doing the symmetry breaking. Analogously, when dealing with non-abelian discrete NGBs, one must also specify the representation doing the breaking. A surprising feature of non-abelian discrete groups is that they can approximate many different groups and cosets to varying degrees of accuracy. To see this feature in action, assume that you have a scalar ϕ in an M dimensional real representation of a non-abelian discrete symmetry $\mathcal{G}$ and take the potential for ϕ to include a negative mass squared term. The largest accidental continuous symmetry that can act on this M dimensional representation is an $SO(M)$ symmetry and we take the leading order operator that breaks this accidental $SO(M)$ symmetry to be ϕ^{N_M}. Thus there are $M-1$ discrete NGBs which non-linearly realize $\mathcal{G}$ and approximate the continuous coset $SO(M)/SO(M-1)$. This situation is in complete analogy to Z_N where we took a 2 dimensional real representation that had a $SO(2)$ accidental symmetry. The leading order operator that breaks this accidental

[1] Depending on the details of the theory, the y^N can also be understood as collective symmetry breaking [64, 66].

$SO(2)$ symmetry was ϕ^N.

If the discrete NGBs obtain an $SO(M)$ breaking but $\mathcal{G}$ preserving Yukawa coupling via the interaction $y\phi\overline{\Psi}\Psi$, then by the same arguments used before in the $\mathbb{Z}_N$ example, the potential giving a mass term to the $M-1$ discrete NGBs scales as $y^{N_M}\phi^{N_M}$. The larger N_M is, the better the discrete NGBs approximates the real Goldstone bosons of $SO(M)/SO(M-1)$. If $N_M > 2$, it is a good enough approximation to remove the quadratic divergence. Because there are many different representations with many different dimensions that all approximate different continuous groups, we see that non-abelian discrete groups can approximate as many continuous cosets as they have representations [2]. This scenario is in complete analogy to Twin Higgs models [26] or Twin Higgs-like models [71] where a $\mathcal{Z}_2$ symmetry plus gauge invariance forces the Higgs mass term to be accidentally $SO(4)$ symmetric and a mass for the pNGB Higgs is only generated by a $SO(4)$ breaking quartic term.

In Sec. 2.2, we give a simple A_4 example and work out in detail how the cancellations occur. In Sec. 2.3, we describe how the results of invariant theory can be used to obtain how suppressed a potential is for a generic non-abelian discrete symmetry. In Sec. 2.4, we explore how exchange representations of discrete symmetry groups can be used. Finally, we conclude in Sec. 2.5

2.2 Explicit example

As a simple example, we will first consider the case of an A_4 non-abelian discrete symmetry. Consider a scalar ϕ which transforms as a triplet under A_4 [3]. A_4 is the group of all even

[2]Interestingly by exactly the same reasoning, large dimensional representations of continuous symmetries can also be used to approximate various cosets.

permutations of four objects and is isomorphic to proper rotations of a regular tetrahedron. From this, one can geometrically see that it is a finite subgroup of $SO(3)$. The scalar ϕ is coupled to a Dirac fermion Ψ via a Yukawa coupling. For simplicity, Ψ is also taken to be a triplet. As we are focusing on the quantum generated potential, we will take the tree level potential to be $SO(3)$ symmetric except for the Yukawa interaction [3].

$$\begin{aligned}\mathcal{L}_{\text{tree}} &= \mathcal{L}_{\text{kin}} + \mathcal{L}_{\text{V}(\phi)} + \mathcal{L}_{\text{int}} \\ \mathcal{L}_{\text{kin}} &= \frac{1}{2}\partial^\mu \phi^T \partial_\mu \phi + \overline{\Psi}(i\gamma^\mu \partial_\mu)\Psi \\ \mathcal{L}_{\text{V}(\phi)} &= \frac{m^2}{2}\phi^T\phi - \frac{\lambda}{4}(\phi^T\phi)^2\end{aligned} \tag{2.1}$$

The tachyonic mass generates a tree level set of degenerate vacua with $\langle \phi^T \phi \rangle = \frac{m^2}{\lambda} \equiv f^2$ that is spanned by the usual Goldstone bosons. After spontaneous symmetry breaking, the scalar triplet around the vacuum $(0, 0, f)$ is parameterized by

$$\phi = \exp\left[\frac{1}{f}\begin{pmatrix} 0 & 0 & \pi_1 \\ 0 & 0 & \pi_2 \\ -\pi_1 & -\pi_2 & 0 \end{pmatrix}\right]\begin{pmatrix} 0 \\ 0 \\ f \end{pmatrix}, \tag{2.2}$$

where π are the familiar Goldstone bosons of the breaking $SO(3)/SO(2)$ and will later become discrete NGBs of A_4. Under the tree level $SO(3)$ symmetry, the pions have a shift symmetry which forbids non-derivative couplings. The approximate $SO(3)$ symmetry is broken explicitly by the Yukawa coupling so that the radiative corrections only respect the global A_4 symmetry

[3] If this assumption bothers the reader, one can start with a more complicated example where the renormalizable potential automatically preserves an accidental global symmetry, e.g. the doublet representation of T'. Alternatively, one can simply assume that the UV theory gives an approximate $SO(3)$ symmetry at tree level in analogy with chiral perturbation theory.

instead of the larger $SO(3)$ symmetry and generate a mass for the pions.

The pions π_1 and π_2 provide a non-linear realization of the A_4 symmetry. A_4 has two generators, s and t, with $s^2 = t^3 = (st)^3 = e$. Explicitly, the s and t generators in the triplet representation are

$$\begin{aligned} s &= \begin{pmatrix} 1 & 0 & 0 \\ 0 & -1 & 0 \\ 0 & 0 & -1 \end{pmatrix} \\ t &= \begin{pmatrix} 0 & 0 & 1 \\ 1 & 0 & 0 \\ 0 & 1 & 0 \end{pmatrix} . \end{aligned} \tag{2.3}$$

To leading order in the pions, the s generator is realized by sending $\pi_2 \to \pi_2 \pm \pi f$. Again to leading order in the pions, the t generator is realized by sending $\pi_1 \to \pi_1 + \pi f/2$ followed by $\pi_2 \to \pi_2 - \pi f/2$.

The most general A_4 invariant Yukawa interaction can be written as

$$\mathcal{L}_{\text{int}} = \left[y_s \begin{pmatrix} \{\overline{\Psi}_2 \Psi_3\} \\ \{\overline{\Psi}_3 \Psi_1\} \\ \{\overline{\Psi}_1 \Psi_2\} \end{pmatrix} + y_a \begin{pmatrix} [\overline{\Psi}_2 \Psi_3] \\ [\overline{\Psi}_3 \Psi_1] \\ [\overline{\Psi}_1 \Psi_2] \end{pmatrix} \right] \cdot \phi \tag{2.4}$$

where

$$\begin{aligned}\{A_iB_j\} &= A_iB_j + B_jA_i \\ [A_iB_j] &= A_iB_j - B_jA_i\end{aligned} \tag{2.5}$$

The anti-symmetric coupling, y_a, is the usual $SO(3)$ invariant piece, does not give a mass to the pions and will thus be neglected for the rest of the section. The novel symmetric coupling, y_s, gives the pions a non-zero yukawa coupling to the fermions but at the same time protects it from the standard quadratic divergences. To see that explicitly, let us Taylor expand the scalar in terms of the pions.

$$\phi_1 = \pi_1 \;\; \phi_2 = \pi_2 \;\; \phi_3 = f\left(1 - \frac{1}{2}\frac{\pi_1^2 + \pi_2^2}{f^2}\right) \tag{2.6}$$

At this order, the interaction term becomes

$$\begin{aligned}\mathcal{L}_{\text{int}} = y\pi_1\big(\overline{\Psi}_2\Psi_3 + \overline{\Psi}_3\Psi_2\big) + y\pi_2\big(\overline{\Psi}_3\Psi_1 + \overline{\Psi}_1\Psi_3\big) \\ + yf\left(1 - \frac{1}{2}\frac{\pi_1^2 + \pi_2^2}{f^2}\right)\big(\overline{\Psi}_1\Psi_2 + \overline{\Psi}_2\Psi_1\big)\end{aligned} \tag{2.7}$$

where we have abbreviated the Yukawa coupling $y_s = y$. One can calculate the one loop quadratic divergence from the two diagrams shown in Fig. 2.1, which neatly cancel each other in a manner very reminisent of Little Higgs models [1, 66, 72, 73].

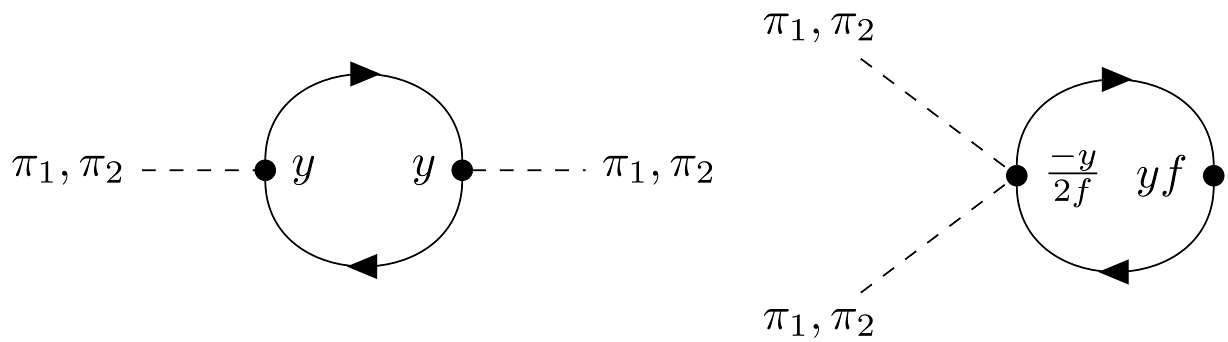

Figure 2.1: The two quadratically divergent one loop diagrams for pion mass that cancel each other exactly.

The surprising cancellation found in the previous example follows from symmetry. Let us write the interaction as

$$L_{\text{int}} = M^{IJ}\overline{\Psi}_I \Psi_J$$
$$M = y \begin{pmatrix} 0 & \phi_3 & \phi_2 \\ \phi_3 & 0 & \phi_1 \\ \phi_2 & \phi_1 & 0 \end{pmatrix} \tag{2.8}$$

where the position of the indices on the 'fermion mass matrix' has no special meaning, $M_{IJ} = M^{IJ}$. The quadraticly divergent part of the one loop Coleman-Weinberg potential for the scalar is

$$\begin{aligned} V_{1\text{ loop}} &\supset -\frac{1}{4\pi^2}\Lambda^2 \,\text{Tr}[M \cdot M^T] \\ &= -\frac{1}{4\pi^2} y^2 \Lambda^2 \, 2(\phi^T \phi) \end{aligned} \tag{2.9}$$

which protects the shift symmetry of the pions. This form is required as the only quadratic invariant of the A_4 group is also an $SO(3)$ invariant. As this conclusion is simply group theoretic, it is not surprising that adding a vector like mass for the fermions does not change anything. In presence of a vector like mass m_ψ, the quadratic part of the one loop potential is

$$
\begin{aligned}
V_{1\text{ loop}} &\supset -\frac{1}{4\pi^2}\Lambda^2 \mathrm{Tr}[M\cdot M^T] \\
&= -\frac{1}{4\pi^2}\Lambda^2\left[y^2\ 2(\phi^T\phi)+3m_\psi^2\right] \\
M &= y\begin{pmatrix} 0 & \phi_3 & \phi_2 \\ \phi_3 & 0 & \phi_1 \\ \phi_2 & \phi_1 & 0 \end{pmatrix} + m_\psi I_{3\times 3}
\end{aligned}
\tag{2.10}
$$

which also doesn't introduce a potential for the pions. Since the Dirac mass term trivially respects the $SO(3)$ symmetry, the reader may have anticipated this behavior.

However, the discrete A_4 symmetry does not entirely prevent the pions from acquiring a potential. The one loop Coleman Weinberg potential (in $\overline{\text{MS}}$) [74, 75] for the pions generated by the fermions is given by

$$
V_{1\text{ loop, fermions}} = -\frac{1}{16\pi^2}\mathrm{Tr}\left((M\cdot M^T)^2\left[\ln\left(\frac{M\cdot M^T}{\mu^2}\right)-\frac{3}{2}\right]\right)
\tag{2.11}
$$

where μ is the renormalization scale. The logarithmic piece breaks the $SO(3)$ symmetry and generates an effective potential for the pions. This potential is plotted in Fig. 2.2.

The one loop potential is flat along the lines $\pi_1 = 0$ or $\pi_2 = 0$ (this is a one-loop accident as the yukawa coupling is proportional to $\pi_1\pi_2$) and has 8 degenerate minima that obey $\pi_1 = \pm\pi_2$. The effective potential gives a vev to the pions so that the vev of the scalar ϕ is stabilized around any of the eight vacua $\frac{f}{\sqrt{3}}\begin{pmatrix}\pm 1 & \pm 1 & \pm 1\end{pmatrix}$ (only four of the eight solutions are shown in Fig. 2.2).

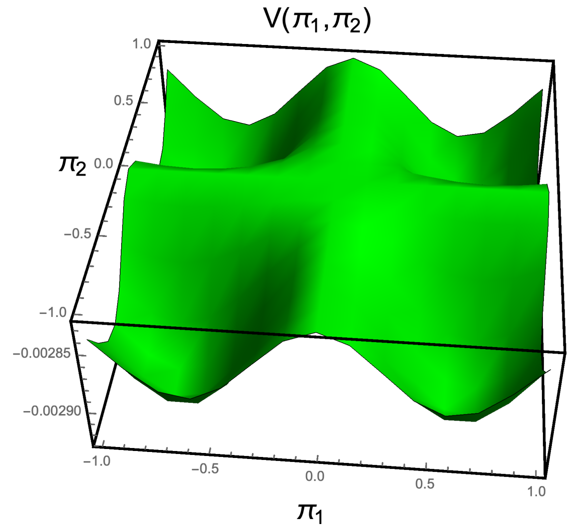

Figure 2.2: One loop potential for the pions in arbitrary units with $m_\psi = 0$, $y = 0.5$, $f = 1$ and $\lambda = 1, \mu = 1$.

The mass of the pions in these new vacua are parametrically smaller than the mass of the radial mode.

In Fig. 2.3, we plot the ratio of the numerical values of m_π^2 to the mass squared of the radial mode. The pions' mass is suppressed by different powers of Yukawa depending on the presence of or absence of a vector-like fermion mass. Depending on if there is a vector-like mass, m_π^2 scales as either y^3 or y^4.

In the presence of a large vector-like mass for the fermions, the effective potential becomes analytic and can be expanded in terms of the expansion parameter $\left(\frac{yf}{m_\psi}\right)$. Schematically, the potential is of the form

$$V_{A_4}(\phi) = m_\psi^4 \sum_n C_n \left(\frac{y\phi}{m_\psi}\right)^n \tag{2.12}$$

As the quadratic part of the scalar potential preserves $SO(3)$, the first non-constant contribution occurs at the third order in the power series expansion. Since the Yukawa generated potential is

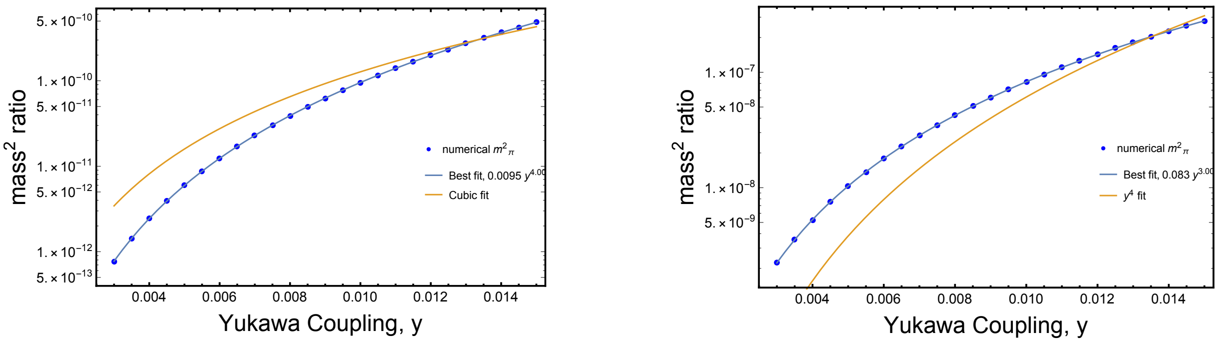

Figure 2.3: The ratio of the square of the heavier discrete NGBs' mass to the square of the radial mode's mass. For simplicity we take $f^2 = \frac{1}{2}$, $\lambda = 1, \mu = 1$. In the left panel, we have assumed $m_\psi = 0$. Under this condition, $\phi \to -\phi$ is a valid symmetry which prohibits odd functions of ϕ in the effective potential. The mass of the pions comes from a term that scales as ϕ^4, hence $m_\pi^2 \propto y^4$. In the right panel, the fermion has a non-zero vector-like mass, $m_\psi = 1$. The Z_2 symmetry is no longer present and pions get a mass from the ϕ^3 term, and hence $m_\pi^2 \propto y^3$.

of the form $f(y\phi)$, the leading order term in the potential is suppressed by y^3 and the the pion mass squared is suppressed by at least the same power of Yukawa coupling. In the case under consideration, Eq. 2.11 can be expanded into the form

$$\begin{aligned} V_{1\text{ loop, fermions}} &= \mathcal{C}_1 + \mathcal{C}_2\phi^T\phi - \frac{y^3 m_\psi \phi_1\phi_2\phi_3\left(3\ln\left(\frac{m_\psi}{\mu}\right)+1\right)}{\pi^2} + O((y\phi)^4) \\ &= \mathcal{C} + \frac{y^3 f m_\psi\left(3\ln\left(\frac{m_\psi}{\mu}\right)+1\right)}{\sqrt{3}\pi^2}(\pi_1+\pi_2)^2 + \frac{2y^3 f m_\psi\left(3\ln\left(\frac{m_\psi}{\mu}\right)+1\right)}{3\sqrt{3}\pi^2\cos^{-1}\left(\frac{1}{\sqrt{3}}\right)^2}(\pi_1-\pi_2)^2 + O(\pi^3) \end{aligned} \tag{2.13}$$

for some constants $\mathcal{C}$, $\mathcal{C}_1$ and $\mathcal{C}_2$. Additionally, in the second line we have expanded the potential around its minimum. In the next section we will see that in other discrete groups the effective potential is even more suppressed. On the other hand, in the absence of a fermion mass, ϕ has a $\phi \to -\phi$ symmetry and the leading order term which breaks A_4 is of the form ϕ^4 leading to the scaling $m_\pi^2 \sim y^4$. However, there is a more dangerous fact hiding in this limit, the effective potential is non-analytic. The non-analytic part of the potential is of the form

$$V(\phi) \sim \sum_k (y\phi)^4 \ln\left(\frac{y^k \phi^k}{\Lambda^k}\right) \sim \sum_k (y\phi)^4 \ln(\phi^k). \tag{2.14}$$

The mass generated by this logarithmic part of the potential will only ever be suppressed by y^4 regardless of how high in k one must go to obtain a non-zero potential for the pions. Thus the mass is only guaranteed to be quadratically suppressed in the Yukawa coupling. This is in complete analogy with collective symmetry breaking models where naive counting will lead one to expect mass terms proportional to $m_\pi^2 \sim \prod_i y_i$ but the 1-loop result can be instead proportional to $m_\pi^2 \sim (\prod_i y_i)^{(4/N)}$ [64].

2.3 Analysis using Invariant Theory

Our example of the tetrahedral group illustrates that discrete symmetries partially protect the Goldstones' mass from radiative corrections. In this section, we show how, given a representation of a non-abelian discrete symmetry, one can use the results of invariant theory to calculate how suppressed the mass term should be.

A simple example is useful in obtaining an intuitive picture of the general discussion. As before, our example will consist of an A_4 discrete symmetry with a scalar in the triplet representation. The starting point involves the invariant polynomials of the triplet representation

$$\mathcal{I}_2(\phi) = \phi^T \phi \quad \mathcal{I}_3(\phi) = \phi_1\phi_2\phi_3 \quad \mathcal{I}_4(\phi) = \sum_i \phi_i^4. \tag{2.15}$$

The invariant polynomials $\mathcal{I}$ are polynomial functions of ϕ that are invariant under A_4. Surprisingly, all A_4 invariant functions of ϕ can be expressed as a function of just these three invariant polynomials. For example

$$\phi^7 = \alpha_1(\mathcal{I}_2(\phi))^2\mathcal{I}_3(\phi) + \alpha_2\mathcal{I}_3(\phi)\mathcal{I}_4(\phi) \tag{2.16}$$

for some real numbers α_i that depend on how one contracts the unspecified A_4 indices. [4]

Since the potential of ϕ respects the underlying symmetry, the effective potential is necessarily of the form

$$V(\phi) = f(\mathcal{I}_2(\phi), \mathcal{I}_3(\phi), \mathcal{I}_4(\phi)). \tag{2.17}$$

Note that $\mathcal{I}_2(\phi)$ is $SO(3)$ invariant and that the first $SO(3)$ non-invariant operator appears at the ϕ^3 level. Thus, we can compute how suppressed the potential for the discrete NGBs of the triplet representation of A_4 must be by simply finding the first invariant polynomial that does not respect an accidental continuous symmetry. In this case, the mass term appears at order ϕ^3.

We now generalize the previous discussions to all representations of any discrete symmetry group. Again, the starting point of our analysis are the invariant polynomials of a symmetry group. As before, given a M dimensional representation $\phi_1, \cdots, \phi_M$, the invariant polynomials are sums of products of the ϕs which are invariant under the discrete symmetry. We will use the convention $\mathcal{I}_n$ to denote an invariant polynomial of degree n. The set of invariant polynomials is called the invariant ring. The elements of the invariant ring of any discrete group can be expressed as a polynomial of finite number of algebraically independent functions, therefore, the invariant ring of a discrete group is 'finitely generated' [76]. This situation is analogous to the fundamental representation of the Orthogonal group, for which all invariant functions can be

[4] A_4 also has a secondary invariant polynomial of degree 6 which is algebraically dependent on the basic invariants but can not be written as a polynomial of basic invariants.

expressed as polynomials of $\phi^T\phi$.

There is thus a simple recipe for determining when the potential for a discrete NGB is non-zero. Given an M dimensional representation, its maximal symmetry group is $SO(M)$ or $SU(M)$. Invariant polynomial of lowest degree typically respect these accidental symmetries. Simply look up the invariant polynomials of the representation and group of interest, and find the polynomial of lowest degree that breaks the accidental global symmetry. The degree of this polynomial gives the degree of suppression of the discrete NGB potential.

The "ideal" situation is if the invariant polynomial that breaks the accidental global symmetry is of very high degree. The easiest way to enforce this condition is if there are not many low dimensional invariant polynomials. There are several mathematical proofs that are useful when searching for such a representation. Combined, these theorems will tell us that when looking for highly suppressed potentials, it is best to look for small representations of groups that have a large number of elements. The most extreme example is $\mathbb{Z}_N$ which has N elements but only has a one-dimensional representation.

The first mathematical proof is a remarkable theorem [77, 78, 79, 80] that guarantees that the number of algebraically independent invariant functions equals the dimension of the representation. The second theorem is the following [81, 82]: If $\mathcal{H}$ is a finite subgroup generated by reflections [5] of a unitary group of n variables, then $\mathcal{H}$ posses n algebraically independent invariant forms $\mathcal{I}_{m_1}, \mathcal{I}_{m_2}, \ldots, \mathcal{I}_{m_n}$ with degrees $m_1, m_2, \ldots, m_n$ such that

$$\prod_{i=1}^{n} m_i = g \tag{2.18}$$

[5] A reflection is a diagonalizable non-identity linear isomorphism of finite order that keeps all the points on a hyperplane fixed. The matrix representation of a reflection has all of its eigenvalues equal to 1 except for a single eigenvalue whose value is the mth root of unity where m is the order of the reflection.

where g is the number of elements in the group. We can readily check the way the theorems apply to Z_N, since Z_N is a reflection generated subgroup of $U(1)$. Z_N has a dimension one representation that then only has one invariant polynomial. As the number of elements in Z_N is N, the degree of the polynomial is forced to be N, hence the only allowed function is ϕ^N. As an example of a non-Abelian group, we can check $A_5 \times Z_2$. A_5 is isomorphic to the proper rotations of an Icosahedron. Being a subgroup of rotation, A_5 doesn't include reflections, but $A_5 \times Z_2$ does. It has a total 120 elements. Its three dimensional representation has three basic invariants. Other than the familiar degree 2 invariant $\phi^T \phi$, two other invariants have degrees 6 and 10, making $\prod_{i=1}^{3} m_i = 2 \cdot 6 \cdot 10 = 120$.

The combination of the theorems forces the following conclusion. If one holds the dimension of the representation fixed, i.e. the number of m_i's, but have very large m_i's, the only way to achieve this is to increase g. Finally we conclude by listing the degrees of the basic polynomial invariants for a few familiar groups. T' illustrates an important subtlety. The two dimensional representation is complex, however the familiar second degree invariant $\phi^* \phi$ is not a polynomial in ϕ in strict mathematical sense and thus is not constrained by these considerations.

Group	n	Parent Lie Group	Number of Elements	Degree of Invariants
A_4	3	$SO(3)$	12	2,3,4
S_4	3	$O(3)$	24	2,3,4
T'	2	$SU(2)$	24	6,8
S_4	3	SO(3)	24	2,4,6
$S_4 \times Z_2$	3	O(3)	48	2,4,6
$A_5 \times Z_2$	3	O(3)	120	2,6,10

Table 2.1: Degree of Polynomial invariants for a few groups. n is the dimension of the representation under consideration. For subgroups of SO(3) or SU(2), the theorem doesn't apply. First three groups are isomorphic to tetrahedron, next two to Cube or Ocathedron. $A_5 \times Z_2$ is isomorphic to Icosahedron.

2.4 Exchange representation

Linear representations require all of the particles in the representation to have the same gauge quantum numbers. The reason for this is that gauge groups are usually uncharged under the transforming symmetries. A simple example of this in the Standard Model is that all three colors of the left handed up quark have the exact same gauge quantum numbers. Aside from linear representations, discrete symmetries are useful because they have exchange representations. This new representation allows for the new possibility that the gauge groups are in the exchange representation of the discrete symmetry, where copies of the gauge group transform into each other under the action of the discrete symmetry [6]. For the example of the Tetrahedral group, we can imagine four fields with their own different gauge groups representing the vertices. The fields along with their gauge sectors interchange among themselves under the group action. A pictorial representation of this scenario is shown in Fig. 2.4.

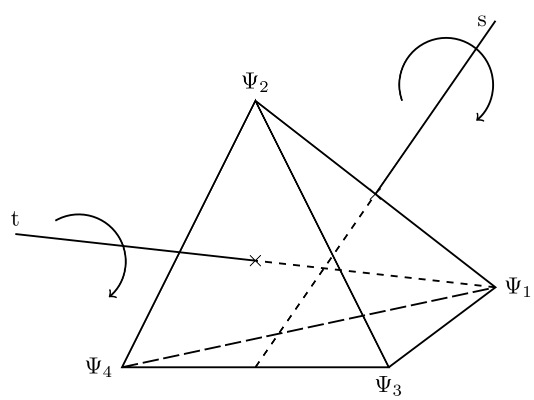

Figure 2.4: The group of proper rotations of a tetrahedron is isomorphic to the group of even permutations of four elements, A_4. A_4 can be succinctly parameterized by two rotations, s and t, which satisfy $s^2 = t^3 = (st)^3 = e$. The span of these two rotations covers A_4. The four fermions occupying the vertices exchange under A_4 as shown in Eq. 2.20.

[6]This situation can be useful in theories such as Twin Higgs, where making partners charged under different gauge symmetries drastically changes the phenomenology.

To elaborate on the example of the Tetrahedron, let us consider four fermions Ψ_j with $1 \leq j \leq 4$ representing the four vertices of a tetrahedron in Figure 2.4 charged under $SU(N)_{j,1\leq j\leq 4}$ gauge symmetries .

$$\begin{aligned}\mathcal{L}_{\text{kin}} &= \sum_j \mathcal{L}_{\text{kin},j} \\ \mathcal{L}_{\text{kin},j} &= \overline{\Psi}_j i\gamma^\mu \big(\partial_\mu - igA^a_{\mu,j}\tau_a\big)\Psi_j\end{aligned} \tag{2.19}$$

Under the action of A_4, the fermions and the gauge fields get exchanged.

$$\begin{aligned}s :&(\Psi_1, A^a_{\mu,1}) \leftrightarrow (\Psi_2, A^a_{\mu,2}), \quad (\Psi_3, A^a_{\mu,3}) \leftrightarrow (\Psi_4, A^a_{\mu,4}) \\ t :&(\Psi_2, A^a_{\mu,2}) \mapsto (\Psi_3, A^a_{\mu,3}) \mapsto (\Psi_4, A^a_{\mu,4}) \mapsto (\Psi_2, A^a_{\mu,2}), \quad (\Psi_1, A^a_{\mu,1}) \mapsto (\Psi_1, A^a_{\mu,1})\end{aligned} \tag{2.20}$$

Since the sectors are related by exchange symmetry, the fermions are all charged under different gauge groups despite being in the same representation of A_4.

There are several ways to couple a scalar to fermions in an exchange representation. If the scalar is also in the exchange representation, then it is trivial to add a new scalar per site. Instead, we will focus on the case where the scalar is in a linear representation and thus has the feature mentioned in the previous sections of having a suppressed potential. The key to coupling a linear and an exchange representation is to realize that the exchange representation can be decomposed into linear representations. The A_4 reducible exchange representation of four fermions can be decomposed into a singlet and a triplet [3].

$$\begin{pmatrix} \overline{\Psi_1}\Psi_1 \\ \overline{\Psi_2}\Psi_2 \\ \overline{\Psi_3}\Psi_3 \\ \overline{\Psi_4}\Psi_4 \end{pmatrix}^{\text{exchange}}_{\mathbf{4}} = \left(\overline{\Psi_1}\Psi_1 + \overline{\Psi_2}\Psi_2 + \overline{\Psi_3}\Psi_3 + \overline{\Psi_4}\Psi_4\right)_{\mathbf{1}} \oplus \begin{pmatrix} \overline{\Psi_1}\Psi_1 + \overline{\Psi_2}\Psi_2 - \overline{\Psi_3}\Psi_3 - \overline{\Psi_4}\Psi_4 \\ \overline{\Psi_1}\Psi_1 - \overline{\Psi_2}\Psi_2 + \overline{\Psi_3}\Psi_3 - \overline{\Psi_4}\Psi_4 \\ \overline{\Psi_1}\Psi_1 - \overline{\Psi_2}\Psi_2 - \overline{\Psi_3}\Psi_3 + \overline{\Psi_4}\Psi_4 \end{pmatrix}_{\mathbf{3}} \tag{2.21}$$

A triplet scalar couples to the irriducible triplet of the exchange representation by the yukawa interaction

$$\mathcal{L}_{\text{int}} = y \begin{pmatrix} \overline{\Psi_1}\Psi_1 + \overline{\Psi_2}\Psi_2 - \overline{\Psi_3}\Psi_3 - \overline{\Psi_4}\Psi_4 \\ \overline{\Psi_1}\Psi_1 - \overline{\Psi_2}\Psi_2 + \overline{\Psi_3}\Psi_3 - \overline{\Psi_4}\Psi_4 \\ \overline{\Psi_1}\Psi_1 - \overline{\Psi_2}\Psi_2 - \overline{\Psi_3}\Psi_3 + \overline{\Psi_4}\Psi_4 \end{pmatrix} \cdot \begin{pmatrix} \phi_1 \\ \phi_2 \\ \phi_3 \end{pmatrix} \tag{2.22}$$

The form of the interaction carries the signature of the underlying symmetry, in this case the A_4 asymmetry. Thus, despite the rather strange appearance of the interaction, the pion masses will again be highly suppressed, in this case by either $y^3(y^4)$ if there is (is not) a vector-like mass.

We can readily apply all the tools mentioned above once we identify all discrete groups which allow for an exchange representation. The amazing feature of discrete groups is that all of them do. The easiest way to construct one is to observe that the group elements exchange among themselves under the action of the group. So every discrete group has an exchange representation with dimensions equal to the number of elements in the group itself. This is a consequence of Cayley's Theorem [83, 84], which states that every group G is isomorphic to a subgroup of a symmetric group acting on G.

The case can be best illustrated with a cyclic group like Z_N. Z_N has a single generator

a and the N elements of the group are simply $(e, a^1, a^2, \ldots, a^{N-1})$. These N elements can be converted into an N dimensional exchange representation using N scalar fields $(\phi_1, \phi_2, \ldots, \phi_N)$ that are permuted under the action of the group as

$$a^k \begin{pmatrix} \phi_1 \\ \phi_2 \\ \vdots \\ \phi_{N-k} \\ \vdots \\ \phi_N \end{pmatrix} = \begin{pmatrix} \phi_{k+1} \\ \phi_{k+2} \\ \vdots \\ \phi_N \\ \vdots \\ \phi_k \end{pmatrix} \tag{2.23}$$

However, the N dimensional exchange representation is reducible since Z_N, being Abelian, only allows for one dimensional irreducible representations (irreps). The singlet can be identified as the linear combination $(\phi_1 + \phi_2 + \cdots + \phi_N)$ and a general irreducible representation is furnished by

$$e^{\frac{i2k\pi}{N}} : (\phi_1 + e^{\frac{i2k\pi}{N}} \phi_2 + \cdots + e^{\frac{i(N-1)2k\pi}{N}} \phi_N), \quad 0 \leq k \leq (N-1) \tag{2.24}$$

The procedure can be generalized to non-Abelian discrete groups which allows for higher dimensional irreps.

The exchange representations generated from Cayley's theorem can be too large to be convenient. For example, the now familiar A_4 group has a 12 dimensional exchange representation. However, in many cases, there exist smaller exchange representations which also have a simple geometrical interpretation. For example, A_4 has four and six dimensional exchange representations which exchange vertices [7] and edges respectively of a regular tetrahedron. For A_5, the group is isomorphic to proper rotations of an Icosahedron, representations with dimensions of twelve, twenty and thirty that exchange its vertices, faces and edges respectively.

2.5 Conclusions

In this paper we initiated a study of the pseudo-Nambu Goldstone bosons of discrete symmetries. NGBs of discrete symmetries feature many interesting properties. On one hand, discrete NGBs can have large shift symmetry breaking Yukawa interactions. On the other hand, discrete NGBs have suppressed potentials, e.g. the quadratically divergent contribution to their potential is not present.

In order to determine how suppressed the potential of a discrete NGB is, first rewrite the non-linear realization in terms of a linear realization. Then find the lowest dimensional operator that breaks the accidental continuous symmetry and gives mass to the discrete NGB. In many cases, there is not a renormalizable operator that can be written down that gives mass to the NGB. We illustrated this procedure in a toy model example where we gave an A_4 theory with a triplet where one could explicitly demonstrate that the potential for the discrete pNGB was suppressed.

Many of these considerations have already been expressed in some form or another mathematically. One example is the idea of invariant polynomials. All products of fields can be rewritten in terms of the invariant polynomials (in much the same way that in an SO theory all gauge invariant operators involving the vector ϕ are just functions of $\phi^T\phi$). By examining the invariant

[7] The representations exchanging four vertices and four faces are equivalent.

polynomials, one can find at what order the accidental continuous symmetries are broken.

Non-abelian discrete symmetries are exciting and it is somewhat surprising that their Nambu Goldstone bosons have not been considered in detail before. We have only scratched the surface of their properties. Perhaps one of the most exciting future directions would be if it were possible to gauge various sub-groups of the accidental symmetries so that one could actually charge discrete NGBs under a gauge symmetry. Many of the examples of pNGBs that are found experimentally and considered theoretically have gauge quantum numbers. It would be exciting if the NGBs of discrete symmetries could also have this property. The suppression of the discrete NGB potential is strongest in vector-like theories that generate analytic potentials. It would be exciting if the cancellations that occur in chiral theories could be made equally strong. pNGBs have guided our thinking for a long time and it would be interesting if discrete NGBs change how we approach model building.

2.6 More details on the A_4 invariant potential

In Sec. 2.2, we presented the A_4 invariant one loop potential with massless fermions in Fig. 2.2, which was flat at the origin. Here we emphasise that this behavior occurs only at the 1-loop level and is specific to the case of massless fermions only. At 2-loops, the flat directions disappear.

For massive fermions, the broken Z_2 symmetry allows odd functions in the effective potential. The total one loop potential now has minima located on the straight lines $\pi_1 = \pi_2$ whereas the maxima are on $\pi_1 = -\pi_2$.

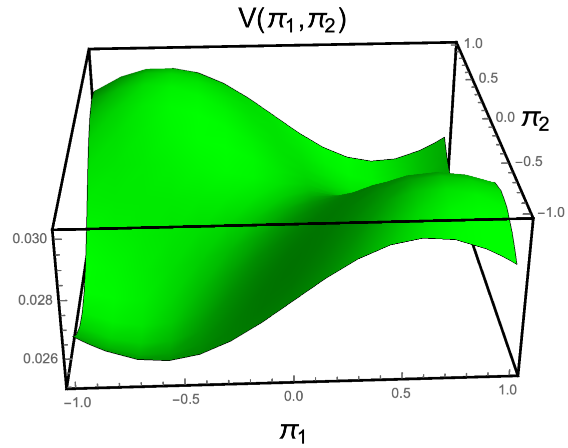

Figure 2.5: The A_4 symmetric one loop potential for $m_\psi = 1$, $y = 0.5$, $f^2 = 1$, $\lambda = 1$, $\mu = 1$. The potential is no longer flat at the origin. The mode $\frac{\pi_1 - \pi_2}{\sqrt{2}}$ has a regular mass where as $\frac{\pi_1 + \pi_2}{\sqrt{2}}$ has a tachyonic mass at $(0, 0)$.

2.7 Platonic Solids

The regular convex polyhedrons, which are also known as Platonic solids, are useful examples of discrete symmetries. In three dimensions, there are only five of such objects. In table 2.2, we present the invariant analysis of the Platonic solids.

Solid	$\mathcal{R}$	$\mathcal{S}$	$\lvert\mathcal{S}\rvert$	Degree of Invariants
Tetrahedron	A_4	S_4	24	2,3,4
Cube	S_4	$S_4 \times Z_2$	48	2,4,6
Octahedron	S_4	$S_4 \times Z_2$	48	2,4,6
Icosahedron	A_5	$A_5 \times Z_2$	120	2,6,10
Dodecahedron	A_5	$A_5 \times Z_2$	120	2,6,10

Table 2.2: The symmetries of five Platonic solids. $\mathcal{R}$ and $\mathcal{S}$ denote Rotation Group and Symmetry Group respectively. More colloquially, $\mathcal{R}$ is the discrete group representing the symmetries of the Platonic solid while $\mathcal{S}$ is the double cover. $|\mathcal{S}|$ denotes the number of elements in the symmetry group.

The rotation groups of Platonic solids are subgroups of rotation group in three dimensions, $SO(3)$. But they have irreducible representation with dimensions other than 3. Here we present the invariant analysis summary of those representations.

Group	n	Parent Lie Group	Order	Degree of Invariants
S_4	2	$SU(2)$	24	2,3
A_5	4	$SO(4)$	60	2,3,4,5
A_5	5	$SO(5)$	60	2,3,3,4,5

Table 2.3: Degree of Polynomial invariants for a few other irreps of the familiar groups.

Finally, all of the Platonic Solids furnish exchange representations of various discrete groups. We conclude by demonstrating how these different exchange representations can be decomposed into the standard linear representations.

2.7.1 Tetrahedron

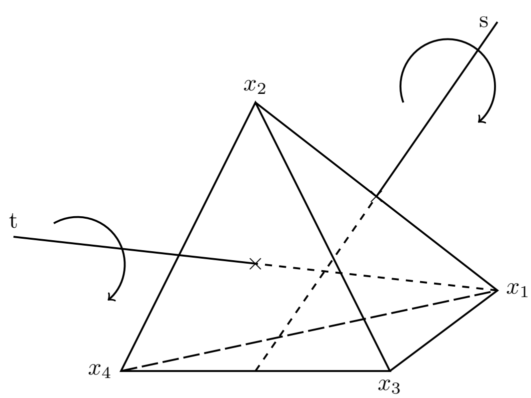

Figure 2.6: Proper rotations of a regular tetrahedon are isomorphic to A_4. A_4 can be parameterized be $s^2 = t^3 = (st)^3 = e$. The four vertices exchange under A_4 as $s : x_1 \leftrightarrow x_2, x_3 \leftrightarrow x_4, t : x_2 \mapsto x_3 \mapsto x_4 \mapsto x_2, x_1 \mapsto x_1$.

The 4 dimensional exchange representation can be decomposed as

$$\begin{pmatrix} x_1 \\ x_2 \\ x_3 \\ x_4 \end{pmatrix}_{\mathbf{4}}^{\text{exchange}} = \Big(x_1 + x_2 + x_3 + x_4\Big)_{\mathbf{1}} \oplus \begin{pmatrix} x_1 + x_2 - x_3 - x_4 \\ x_1 - x_2 + x_3 - x_4 \\ x_1 - x_2 - x_3 + x_4 \end{pmatrix}_{\mathbf{3}} . \tag{2.25}$$

2.7.2 Cube

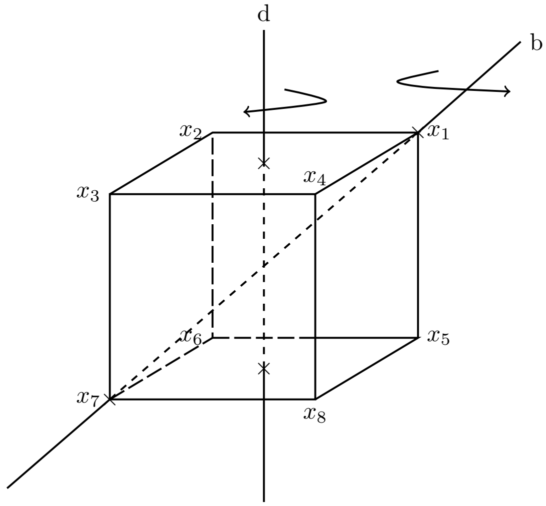

Figure 2.7: The group of proper rotations of a cube are isomorphic to S_4, the group of all possible permutations of four objects. S_4 can be parameterized by [3] $b^3 = d^4 = e$, $db^2d = b$ and $dbd = bd^2b$. The eight vertices exchange under S_4 as $b : x_1 \mapsto x_1, x_7 \mapsto x_7, x_2 \mapsto x_4 \mapsto x_5 \mapsto x_2, x_3 \mapsto x_8 \mapsto x_6 \mapsto x_3$, $d : x_1 \mapsto x_4 \mapsto x_3 \mapsto x_2 \mapsto x_1, x_5 \mapsto x_8 \mapsto x_7 \mapsto x_6 \mapsto x_5$.

The 8 dimensional exchange representation can be decomposed as

$$\mathbf{8} = \mathbf{1} \oplus \mathbf{1}' \oplus \mathbf{3} \oplus \mathbf{3}'$$

$$\begin{pmatrix} x_1 \\ x_2 \\ x_3 \\ x_4 \\ x_5 \\ x_6 \\ x_7 \\ x_8 \end{pmatrix}_{\mathbf{8}}^{\text{exchange}} = \begin{pmatrix} x_1 + x_2 + x_3 + x_4 + x_5 + x_6 + x_7 + x_8 \end{pmatrix}_{\mathbf{1}} \oplus \begin{pmatrix} x_1 - x_2 + x_3 - x_4 - x_5 + x_6 - x_7 + x_8 \end{pmatrix}_{\mathbf{1}'} \oplus \begin{pmatrix} x_1 - x_2 + x_3 - x_4 + x_5 - x_6 + x_7 - x_8 \\ x_1 + x_2 - x_3 - x_4 - x_5 - x_6 + x_7 + x_8 \\ x_1 - x_2 - x_3 + x_4 - x_5 + x_6 + x_7 - x_8 \end{pmatrix}_{\mathbf{3}} \oplus \begin{pmatrix} x_1 + x_2 + x_3 + x_4 - x_5 - x_6 - x_7 - x_8 \\ x_1 - x_2 - x_3 + x_4 + x_5 - x_6 - x_7 + x_8 \\ x_1 + x_2 - x_3 - x_4 + x_5 + x_6 - x_7 - x_8 \end{pmatrix}_{\mathbf{3}'} . \tag{2.26}$$

2.7.3 Octahedron

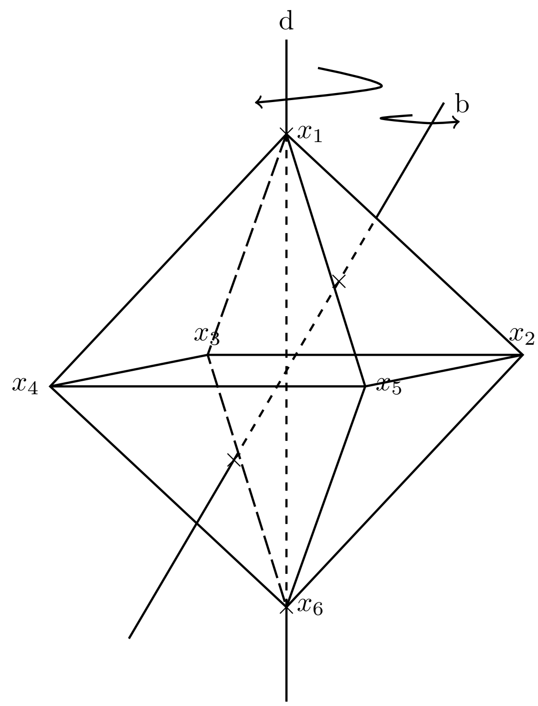

Figure 2.8: Octahedron and Cube are dual to each other. We parameterize Octahedron similar to the cube, $b^3 = d^4 = e$, $db^2d = b$ and $dbd = bd^2b$. The six vertices exchange under S_4 as $b : x_1 \mapsto x_2 \mapsto x_3 \mapsto x_1, x_4 \mapsto x_5 \mapsto x_6 \mapsto x_4$, $d : x_1 \mapsto x_1, x_6 \mapsto x_6, x_3 \mapsto x_2 \mapsto x_5 \mapsto x_4 \mapsto x_3$.

The six dimensional exchange representation can be decomposed as

$$\mathbf{6} = \mathbf{1} \oplus \mathbf{2} \oplus \mathbf{3'}$$

$$\begin{pmatrix} x_1 \\ x_2 \\ x_3 \\ x_4 \\ x_5 \\ x_6 \end{pmatrix}^{\text{exchange}}_{\mathbf{6}} = \begin{pmatrix} x_1 + x_2 + x_3 + x_4 + x_5 + x_6 \end{pmatrix}_{\mathbf{1}} \oplus \begin{pmatrix} (x_1+x_6) + \omega(x_2+x_4) + \omega^2(x_3+x_5) \\ (x_1+x_6) + \omega^2(x_2+x_4) + \omega(x_3+x_5) \end{pmatrix}_{\mathbf{2}} \oplus \begin{pmatrix} \sqrt{3}(x_1 - x_6) \\ \sqrt{3}(x_2 - x_4) \\ \sqrt{3}(x_3 - x_5) \end{pmatrix}_{\mathbf{3'}} \tag{2.27}$$

where $\omega = \exp(\frac{2i\pi}{3})$.

2.7.4 Icosahedron

Icosehedron [3] and Dodecahedron are dual to each other. Icosehedron has 12 vertices where as Dodecahedron has 20. For simplicity, we will only consider the Icosehedron.

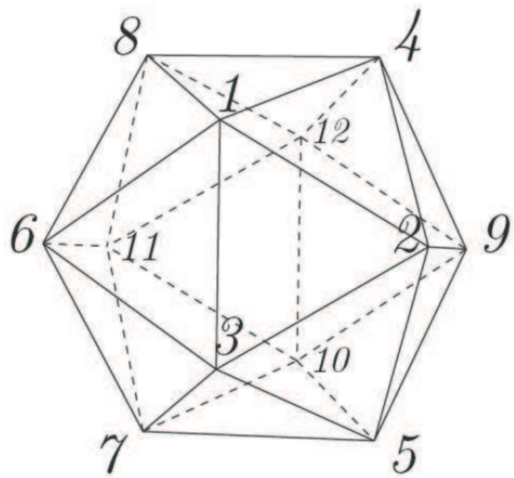

Figure 2.9: Proper rotations of an Icosehedron is isomorphic to A_5. A_5 can be parameterized by [3] $a^2 = b^5 = (ab)^5 = e$, where a corresponds to rotation by π about the edge joining vertices 1 and 2 and b corresponds to clockwise rotation by axis passing through the centre of the face 10-11-12. The 12 vertices exchange under A_5 as a : $(x_1, x_2, x_3, x_4, x_5, x_6, x_7, x_8, x_9, x_{10}, x_{11}, x_{12}) \mapsto (x_2, x_1, x_4, x_3, x_8, x_9, x_{12}, x_5, x_6, x_{11}, x_{10}, x_7)$, $b : (x_1, x_2, x_3, x_4, x_5, x_6, x_7, x_8, x_9, x_{10}, x_{11}, x_{12}) \mapsto (x_2, x_3, x_1, x_5, x_6, x_4, x_8, x_9, x_7, x_{11}, x_{12}, x_{10})$.

This 12 dimensional exchange representation can be decomposed as

$$\mathbf{12} = \mathbf{1} \oplus \mathbf{3} \oplus \mathbf{3'} \oplus \mathbf{5}$$

$$\begin{pmatrix} x_1 \\ x_2 \\ x_3 \\ x_4 \\ x_5 \\ x_6 \\ x_7 \\ x_8 \\ x_9 \\ x_{10} \\ x_{11} \\ x_{12} \end{pmatrix}^{\text{exchange}}_{\mathbf{12}} = \begin{pmatrix} x_1 + x_2 + x_3 + x_4 + x_5 + x_6 + x_7 + x_8 + x_9 + x_{10} + x_{11} + x_{12} \end{pmatrix}_{\mathbf{1}}$$

$$\oplus \begin{pmatrix} x_2 + x_5 - x_8 - x_{11} + \frac{1}{\phi}(x_3 + x_9 - x_6 - x_{12}) \\ x_1 + x_4 - x_7 - x_{10} + \frac{1}{\phi}(x_2 + x_8 - x_5 - x_{11}) \\ x_3 + x_6 - x_9 - x_{12} + \frac{1}{\phi}(x_1 + x_7 - x_4 - x_{10}) \end{pmatrix}_{\mathbf{3}}$$

$$\oplus \begin{pmatrix} x_1 + x_4 - x_7 - x_{10} + \phi(x_5 + x_{11} - x_2 - x_8) \\ x_8 + x_{11} - x_2 - x_5 + \phi(x_3 + x_9 - x_6 - x_{12}) \\ x_3 + x_6 - x_9 - x_{12} + \phi(x_4 + x_{10} - x_1 - x_7) \end{pmatrix}_{\mathbf{3'}}$$

$$\oplus \begin{pmatrix} x_1 + x_4 + x_7 + x_{10} - \frac{1}{\phi}(x_2 + x_5 + x_8 + x_{11}) + (\frac{1}{\phi} - 1)(x_3 + x_6 + x_9 + x_{12}) \\ \frac{1}{\phi}(x_2 + x_{11} - x_5 - x_8) \\ \frac{1}{\phi}(x_1 + x_{10} - x_4 - x_7) \\ \frac{1}{\phi}(x_3 + x_{12} - x_6 - x_9) \end{pmatrix}$$

where $\phi = \frac{\sqrt{5}+1}{2}$, $a_1 = \frac{3-2\phi}{\sqrt{3}}$, $a_2 = \sqrt{\frac{3}{5}}\frac{1+2\phi}{\phi^4}$ and $a_3 = \frac{1+5\phi^3}{2\sqrt{3}(\phi+2\phi^2)}$.

Chapter 3: Black Hole Production of Monopoles in the Early Universe

This work was done in collaboration with Anson Hook and is published in J. High Energ. Phys. 2021, 145 (2021).

3.1 Overview

One of the most fascinating objects in physics are black holes. Black holes have been observed at the center of many galaxies and play a central role in astrophysics [85, 86]. Aside from astrophysical black holes, black holes are often also a consequence of early universe dynamics such as hybrid inflation [87, 88, 89, 90, 91, 92, 93, 94], phase transitions [95, 96, 97, 98, 99, 100, 101, 102, 103, 104] or topological defects [105, 106]. In fact, in many of these scenarios there are so many black holes produced that they become the dominant energy density of the entire universe [107, 108, 109, 110, 111, 112, 113].

While a black hole dominated era may seem like a phenomenological disaster, it turns out that due to Hawking radiation [114, 115, 116], black holes evaporate and the universe eventually transitions into the standard early universe radiation dominated regime [117, 118, 119, 120, 121, 122, 123]. As compared to more standard reheating mechanisms, reheating the universe through black hole evaporation is a rather unique process. The reason for this is two-fold.

Firstly, as a black hole evaporates, its temperature rises until the black hole becomes a

Planck mass and Planck temperature object. As such, black hole evaporation depends in part on ultraviolet physics. Secondly, a black hole is extremely massive and thus serves as a heat source. It heats up the surrounding plasma to large temperatures creating a temperature profile around the black hole that can also reach temperatures close to the Planck scale [1]. Due to the large radius of this profile, the effects of the surrounding plasma may be more significant than the black hole itself.

In this article, we present one example, monopole production, where the the hot plasma surrounding a black hole is more important than the black hole itself. Monopoles are another object of great interest to particle physicists [30, 124, 125]. They are especially relevant given that they are a generic prediction of quantum field theories and feature in many well motivated models such as Grand Unified Theories [28, 29, 126, 127]. Aside from their magnetic charge, the other property of monopoles is that as composite objects [30], their physical radius is larger than their Compton wavelength. This mismatch means that monopole production coming from Hawking radiation is always exponentially suppressed [31]. By the time that black holes are hot enough to produce monopoles without a Boltzmann suppression, the black hole is smaller than the monopole meaning that the emission of monopoles is still exponentially suppressed.

However, monopole production by the plasma surrounding the black hole is not exponentially suppressed. Because the plasma surrounding the black hole has a radius much larger than the black hole, it can easily produce many monopoles via the Kibble-Zurek mechanism [128, 129, 130]. Close to the black hole, the plasma is hot enough that symmetry is restored. After the black hole evaporates, this hot region slowly cools down. At some point, it undergoes a symmetry

[1] Even if there was originally no radiation around the black hole, once $\mathcal{O}(1)$ of the black holes have started to evaporate, the universe is effectively reheated and there is a large bath of particles for the rest of the black holes to heat up.

breaking phase transition. Regions of space separated by more than a correlation length all choose their vacua independently and monopoles are created depending on those random values.

Monopole production from evaporating black holes can be extremely efficient. As an example, we show that if the universe was reheated by black holes and monopoles were produced by a second order phase transition, the monopole over-production limits the reheat temperature to be

$$T_{RH} \lesssim 500\,\mathrm{GeV}\left(\frac{10^{15}\,\mathrm{GeV}}{T_{PT}}\right)^{9/35}. \tag{3.1}$$

Despite the very low reheat temperature of the universe and the very large scale associated with the phase transition, T_{PT}, producing the monopole, monopoles can still very easily over-close the universe. The re-introduction of the monopole problem in this context occurs because even if the average temperature is low, the temperature around the black holes themselves is still very large.

There are reasons to believe [131] that as the black holes reach Planck scale masses that Hawking radiation is modified and possibly even stops completely. As long as the temperature of the phase transition producing the monopoles is lower than the temperature at which Hawking radiation ceases, then monopole production by the plasma would be completely unaffected. There may however be other constraints that one needs to take into account such as over-closing the universe with remnants.

Depending on the model dependent properties of the monopoles, bounds even stronger than Eq. 3.1 can also be obtained. The Parker bound [132] on monopoles destroying galactic magnetic fields gives the constraint $T_{RH} \lesssim 500\,\mathrm{GeV}\left(\frac{T_{PT}}{10^{15}\,\mathrm{GeV}}\right)^{12/35}$. The stronger and slightly more uncertain improvements on the Parker bound [133, 134] imply even stronger bounds on

T_{RH}. If the monopoles catalyze baryon number decay with geometric cross sections, there are extremely strong bounds on their abundance [135, 136, 137]. In this case, the bounds on the reheating temperature are so strong as to be excluded by BBN. Thus baryon number violating monopoles and reheating via black hole decay are mutually exclusive.

A reheat temperature this low is very impactful as it strongly favors reheat temperatures lower than the scale at which electroweak sphalerons are active. This limits the available baryogenesis mechanisms and pushes one to consider black hole assisted baryogenesis mechanisms [114, 121, 138, 139, 140, 141, 142, 143, 144, 145, 146, 147]. Additionally, many models of black hole production in the early universe produce only a sub-population of black holes, e.g. a popular scenario is when primordial black holes are dark matter [111, 148, 149]. Evaporation of a sub-population of primordial black holes provides a mechanism for producing a sub-dominant populations of monopoles.

In Sec. 3.2, we derive the temperature profile of the plasma surrounding a black hole in the early universe. In Sec. 3.3, we calculate how many monopoles are produced per black hole. In Sec. 3.4, we place a bound on the reheat temperature coming from monopole over production if the universe was reheated by black holes. In Sec. 3.5, we discuss the approximations under which our calculations are valid. Finally, we conclude in Sec. 3.6.

3.2 Temperature Profile Around a Black Hole

In this section, we derive the temperature profile around a black hole evaporating in the early universe. We will describe how a black hole heats up the plasma surrounding it and how this hot region of space cools after the black hole evaporates.

3.2.1 Radiation Transfer

To set the stage, we first present the derivation of the equations governing the transfer of energy in a relativistic thermal system. The discussion in this section will be a terse summary of the material presented in Ref. [150].

The starting point is a quantity called the specific intensity, $I_\nu(\vec{r}, \hat{s}, t)$, which is the energy emitted per area per solid angle per time per frequency. For simplicity, we will work in the plane approximation where quantities vary in z but not in x and y. The specific intensity is related to the more familiar quantities such as a systems total energy density (ρ), radiation pressure (P), and energy flux (J_z) by

$$\rho = \int d\Omega d\nu\, I_\nu \qquad J_z = \int d\Omega d\nu \cos\theta\, I_\nu \qquad P = \int d\Omega d\nu \cos^2\theta\, I_\nu.$$

The energy emitted in a direction $\hat{s}$ has its power modulated by

$$\frac{dI_\nu}{ds} = -\frac{1}{\lambda} I_\nu + j_\nu \tag{3.2}$$

where j_ν is the power being emitted in the $\hat{s}$ direction and $\lambda = 1/n\sigma$ is the scattering length. The first term gives the absorption of radiation passing through the thermal bath while the second gives the power emitted by the bath itself. Often, Eq. 3.2 is written in terms of the optical depth parameter by $d\tau = -dz/\lambda = -\cos\theta\, ds/\lambda$. Written in terms of the optical depth, Eq. 3.2 becomes

$$\cos\theta \frac{dI_\nu}{d\tau} = I_\nu - \lambda j_\nu. \tag{3.3}$$

This equation can be further simplified by multiplying by $\cos\theta$ and integrating over solid angle and frequency. A thermal system emits radiation isotropically so that $\int d\Omega \cos\theta \, j_\nu = 0$, leaving

$$J_z = \frac{dP}{d\tau} = -\frac{\lambda}{3}\frac{d\rho}{dz}, \tag{3.4}$$

where in the second equality we used the fact that in thermal equilibrium $P = \rho/3$. Eq. 3.4 shows how the energy flux is related to temperature gradients. The final equation we will consider is simply the conservation of energy

$$\frac{d\rho}{dt} = -\frac{dJ_z}{dz} = \vec{\nabla}\left(\frac{\lambda}{3}\vec{\nabla}\rho\right), \tag{3.5}$$

where we use Eq. 3.4 in the second equality.

This conservation equation governs how a system heats and cools. In what follows we will be solving this conservation equation with various initial conditions and boundary conditions corresponding to a black hole evaporating and the subsequent cooling phase. In a relativistic thermal system $\lambda \propto 1/T$ and $\rho \propto T^4$, so Eq. 3.5 is a differential equation that one can solve for the temperature profile, $T(\vec{r}, t)$.

3.2.2 Heating

In this subsection, we will solve Eq. 3.5 subject to the condition that there is a black hole providing a heat source at $r = 0$. In the cases we will be interested in, we are dealing with regions close enough to the black hole that we can safely assume that the asymptotic temperature is negligible.

Intuition for the problem can be built up by first starting with the case of a boundary condition $T = T_0$ at a radius r_0. In this case, the equilibrium solution of Eq. 3.5 can be easily seen to be

$$T(r) = \left(\frac{r_0}{r}\right)^{1/3} T_0. \tag{3.6}$$

Thus we see that when in equilibrium, the temperature falls off rather slowly when far from the heat source. The above scaling can also be obtained by using the fact that in equilibrium, the total energy leaving any radius must be the same. Using Eq. 3.4 we have $4\pi r^2 J_r \sim rT^3$, which should be radius independent, giving another way of finding Eq. 3.6.

We now discuss the situation of interest. A black hole of mass M_{BH} initially starts off emitting Hawking radiation at a temperature T_{BH} from a radius r_{BH},

$$T_{BH} = \frac{M_{pl}^2}{8\pi M_{BH}} \qquad r_{BH} = \frac{1}{4\pi T_{BH}}, \tag{3.7}$$

where M_{pl} is Planck's constant. The Hawking radiation receives grey body correction factors so that the total energy emitted by the black hole is

$$\frac{dM_{BH}}{dt} = -\frac{\mathcal{G}_f g_\star M_{pl}^4}{30720\pi M_{BH}^2} \equiv -c_1 \frac{M_{pl}^4}{M_{BH}^2}, \tag{3.8}$$

where $\mathcal{G}_f$ is the temperature and spin dependent grey body factor and $g_*(T)$ is the total number of entropic degrees of freedom. For the Standard Model, we average over all particles and find that $\mathcal{G}_f \sim 4$. As a result of this emission, the black hole slowly evaporates and its temperature as a function of time is

$$T_{BH}(t) = \frac{M_{pl}^2}{8\pi} \frac{1}{\left(M_{BH}^3 - 3c_1 M_{pl}^4 t\right)^{1/3}}. \tag{3.9}$$

In the rest of this sub-section, we will derive the temperature profile that results from a time and space dependent boundary condition of this sort.

Analytical Estimate We first describe how to obtain an $\mathcal{O}(1)$ analytical estimate of the profile before moving on to numerical solutions. There are two critical observations that render black hole heating easy to estimate. The first fact is that in any thermal system, energy diffuses out as a random walk. If there is a change at $r = 0$ at a time $t = 0$, then at a later time t only radii smaller than $r^2 \lesssim \lambda t$ have noticed the change while all physics outside of this radius have not noticed the change. The second observation is the simple fact that when the black hole evaporates, it spends more time at lower temperatures than it does at higher temperatures. Combined, these two observations allow one to treat the heating process like an onion. At any given time, the black hole is in diffusion limited thermal contact with a region of space around it. As the black hole evaporates, this region of space shrinks. The final temperature profile at any given radius is set by when that radius "freezes-out" and leaves equilibrium with the black hole.

To turn this intuition into a set of equations, we start with a black hole of temperature T_{BH}. This black hole evaporates in a finite time $t_{BH} \sim M_{pl}^2/T_{BH}^3$. In this time, the energy can only diffuse out to a distance

$$r_d^2 \sim \lambda t_{BH} \sim \frac{M_{pl}^2}{T(r_d) T_{BH}^3}. \tag{3.10}$$

We will make the approximation that everything inside of r_d is in equilibrium with the black hole while everything outside of r_d is not in equilibrium and has been frozen in place and is no longer changing. When we later consider cooling, it will become clear that the cooling time is much longer than the heating time and that treating the temperature profile outside of the radius r_d as constant is a reasonable approximation.

A consequence of this freezing-out assumption is that for radii $r < r_d$, the temperature profile should scale as $T \sim 1/r^{1/3}$ as found in Eq. 3.6. While for radii $r > r_d$, the temperature profile is a fossilized memory of when the black hole was just leaving equilibrium with that radius. Eventually the black hole has evaporated completely and the temperature profile consists entirely of the frozen out part of the profile.

To determine the final temperature profile after the evaporation of the black hole, at every radius, we find what its temperature was when it was just leaving equilibrium with the black hole and set the final temperature to be that value. In equilibrium, the flux of energy leaving the black hole is equal to the flux leaving the thermal bath. Applying this to the radius r_d, we have

$$\frac{dM_{BH}}{dt} \sim T_{BH}^2 \sim 4\pi r_d^2 J_r \sim r_d T(r_d)^3. \tag{3.11}$$

Combining Eq. 3.10 and Eq. 3.11 we arrive at the scaling

$$T(r) \sim \frac{M_{pl}^{4/11}}{r^{7/11}} \tag{3.12}$$

for all radii which have decoupled from the black hole.

There is a second derivation of this scaling where instead of requiring Eq. 3.11, we instead impose that the black hole's mass is larger than the total energy stored in the region r_d. If the black hole mass is smaller, then that temperature is necessarily frozen out by conservation of energy. This different argument also gives the scaling found in Eq. 3.12.

Numerical calculation To put $\mathcal{O}(1)$ numbers to Eq. 3.12, we will solve Eq. 3.5 numerically. Unfortunately, the exact problem of interest has two aspects which makes it difficult to solve numerically. The first is that the black hole shrinks as it evolves and a boundary condition whose location r_H is changing as a function of time is difficult to solve. The second one is that the region right near the black hole is not in thermal equilibrium with the radiation emitted by the black hole and thus would require other methods to deal with.

To eliminate these problems, we consider a fixed radius, r_0 which is in thermal contact with the black hole and use it as our boundary. Any surface which is in thermal contact with the black hole has the same energy passing through it as what was emitted by the black hole. This means

$$\tfrac{dM_{BH}}{dt} \sim T_{BH}^2 \sim 4\pi r_0^2 J_{r_0} \sim r_0 T(r_0)^3 \tag{3.13}$$

$$\implies T(r_0) \sim \tfrac{T_{BH}^{2/3}}{r_0^{1/3}}. \tag{3.14}$$

We can then solve Eq. 3.5 with the boundary condition

$$T(r_0,t) \equiv T_0(t) = T_{0H}\left(\frac{\tau}{\tau - t}\right)^{\frac{2}{9}}, \tag{3.15}$$

which was obtained from Eq. 3.13 using Eq. 3.9. τ is the characteristic lifetime of the black hole and T_{0H} is the initial temperature of the surface at r_0. To match our numerical solution to the analytical approach, we repeat the analysis done in the analytic section including a proportionality coefficient that will be determined numerically.

Energy passing through the surface at r_0 can only reach a finite distance during the lifetime of the black hole. The lifetime of the black hole as a function of the temperature at r_0 is

$$t_c = \tau \left(\frac{T_{0H}}{T_0}\right)^{9/2}. \tag{3.16}$$

Within its lifetime, the energy can only diffuse up to a distance r_d

$$r_d^2 = c_0 \lambda\, t_c = c_0 \frac{c_\lambda}{T(r_d)} \tau \left(\frac{T_{0H}}{T_0}\right)^{9/2}, \tag{3.17}$$

where we have introduced a proportionality constant c_0 that will be determined numerically. We have also defined c_λ as $\lambda(T) = 1/(n\sigma) = c_\lambda/T$, which is a parameter that depends on the microscopics of the theory and can be scaled out of the problem.

As before, we require that the flux emitted at r_0 is the same as the flux passing through r_d,

$$r_0 T_0^3 = r_d T(r_d)^3. \tag{3.18}$$

Combining Eq. 3.17 and Eq. 3.18, we find the scaling

$$T(r) = (c_0 c_\lambda)^{2/11} \frac{\left(r_0 T_{0H}^3\right)^{3/11} \tau^{2/11}}{r^{7/11}}. \tag{3.19}$$

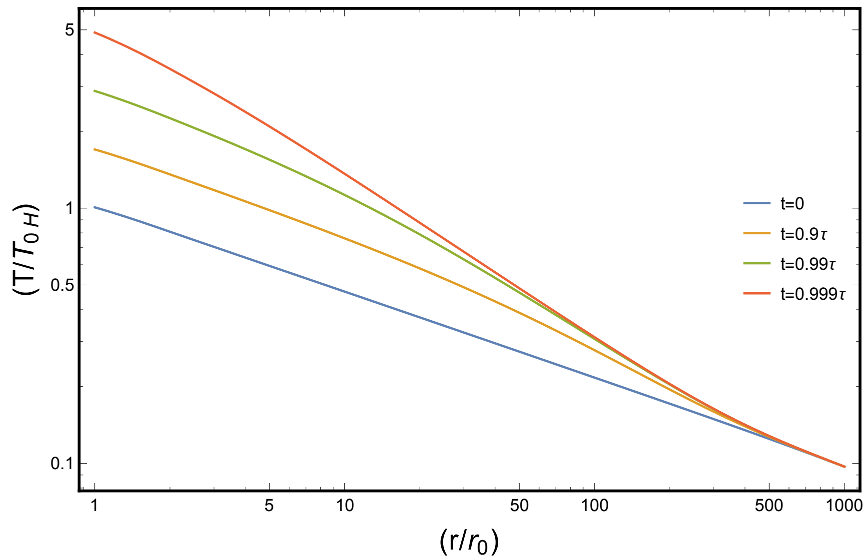

Figure 3.1: The temperature profile during the heating phase of a black hole like object. We start from an equilibrium profile at $t = 0$ of $T(r) \sim r^{-1/3}$. The temperature profile below the diffusion radius remains in equilibrium with the black hole. As the diffusion radius gradually shrinks, temperatures outside of it freezes out giving a profile of $T(r) \sim r^{-7/11}$ as expected from analytical arguments of this example.

We have solved Eq. 3.5 numerically subject to the boundary condition shown in Eq. 3.15. Perhaps unsurprisingly, the numerical solution exhibits the scaling found in Eq. 3.19 with

$$c_0 = 0.59. \tag{3.20}$$

The numerical solution is shown in Fig. 3.1 for various times. For simplicity, an initial condition of $T \sim 1/r^{1/3}$ is assumed. Many of the features anticipated by the analytical analysis are found here. First, all radii beyond $r \sim 700r_0$ are frozen to their initial values. The black hole evaporates too quickly for the heat it deposits to diffuse past that radius. The second feature that is present at all times and most visible for $t = 0.9\tau$, (τ is the characteristic lifetime of the BH, as defined before) is that near the black hole there is a region of space which is still in equilibrium with the black hole and scaling as $T \sim 1/r^{1/3}$. The last visible feature, most easily seen for $t \gtrsim 0.99\tau$, is the freeze-out regime. The regions beyond $r \gtrsim 50\, r_0$ have frozen out and subsequent evolution is not changing its temperature profile.

The constant c_0 allows us to calculate Eq. 3.12 for the problem of interest with $\mathcal{O}(1)$ numbers, namely the heating profile of an evaporating black hole. To facilitate our description of the calculation, we define new constants c_2 and c_5 as

$$t_{BH} \equiv c_2 \frac{M_{pl}^2}{T_H^3} \qquad\qquad \rho \equiv c_5 T^4. \tag{3.21}$$

We can now re-derive Eq. 3.12 in all of its full numerical glory

$$T(r) = \left(\frac{6^6 \pi^3 c_0^2 c_1^2 c_2^2}{c_5^3 c_4} \right)^{1/11} \frac{M_{pl}^{4/11}}{r^{7/11}} = 0.183 \left(\frac{c_\alpha^2 G_f}{g_*(T)} \right)^{1/11} \frac{M_{pl}^{4/11}}{r^{7/11}} \tag{3.22}$$

Where as before G_f is the Grey body factor of a black hole, $g_*(T)$ is the total number of entropic degrees of freedom and c_α characterizes the scattering cross section, $\sigma(T) = c_\alpha^2(T)/T^2$. The expectation is that c_α will be of order $\alpha = g^2/4\pi$, but due to the large number of possible final states, c_α can be a bit larger than α. The main assumption we have made so far is that is thermal equilibrium is maintained. Eventually the black hole's Hawking radiation will not be instantly absorbed by the thermal bath so that Eq. 3.22 is only valid for distances larger than some critical radius.

3.2.3 Cooling

Right after the black hole has evaporated, the temperature profile around it is of the form $T(r) \equiv c\, M_{pl}^{4/11}/r^{7/11}$. In this subsection, we describe how this temperature profile cools.

Analytical Estimate The temperature profile left after a black hole evaporates is IR dominated so that it cools through an inverse of how it heated. Namely, the inner regions cool faster than the outer regions. To see this explicitly, we can use Eq. 3.5 to see that

$$t_{char} \sim \frac{E}{dE/dt} \sim \frac{r^3 T^4}{\frac{r^2}{T}\nabla T^4} \sim r^{15/11}. \tag{3.23}$$

From this characteristic cooling time we see that the smaller r cool faster and the larger r cool slower. As a result, the center of the profile cools first and reaches a constant temperature. As the outer regions start to cool, this region of constant temperature slowly expands in space while cooling off. As such, we will make the following approximation for the form of the cooling profile.

$$T = T_{in} \qquad\qquad r < r_c \tag{3.24}$$

$$T = c\frac{M_{pl}^{4/11}}{r^{7/11}} = T_{in}\left(\frac{r_c}{r}\right)^{7/11} \qquad\qquad r > r_c \tag{3.25}$$

We take there to be a cooling radius $r_c(t)$ inside of which there is a uniform sphere of constant temperature $T_{in}(t)$. Outside of the cooling radius, the temperature is the same as it was pre-cooling. Matching at the boundary relates

$$T_{in} \sim M_{pl}^{4/11}/r_c^{7/11}. \tag{3.26}$$

We can find the functions $r_c(t)$ and $T_{in}(t)$ using conservation of energy. The region of space inside of $r_c(t)$ is cooling at a rate

$$\frac{dE}{dt} \sim 4\pi r_c^2 \frac{\lambda}{3} \nabla\rho \sim r_c T_{in}^3 \qquad \text{with} \qquad \frac{dE}{dt} \sim \frac{E}{t} \sim \frac{r_c^3 T_{in}^4}{t}. \tag{3.27}$$

Combining Eq. 3.26 with Eq. 3.27, we find the time dependencies

$$r_c(t) \sim \frac{t^{11/15}}{M_{pl}^{4/15}} \qquad T_{in}(t) \sim \frac{M_{pl}^{8/15}}{t^{7/15}}. \tag{3.28}$$

Numerical Calculation How the profile cools is easy to solve numerically. We numerically solve the conservation of energy equation, Eq. 3.5, with the initial condition

$$T(r,t_0) = T_0 \qquad r \le r_0 \tag{3.29}$$

$$T(r,t_0) = T_0 \left(\frac{r_0}{r}\right)^{7/11} \qquad r > r_0. \tag{3.30}$$

We add a small region of constant T_0 in the center of the initial profile to help deal with $r = 0$. Our numerical results are insensitive to how one treats the $r \sim 0$ region.

The results of the numerical simulation are shown in Fig. 3.2. As is evident, the numerical solution satisfies our intuition about how cooling occurs. Namely, there is a region of constant temperature that slowly expands as it cools off. Meanwhile the temperature outside this expanding sphere maintains its pre-cooling temperature. The result of a numerical simulation is that the temperature of the plautau region falls as

$$T_{in} = T(r_0,t) = 0.87 \left(g_*(T) c_\alpha^2\right)^{7/15} \frac{T_0^{22/15} r_0^{14/15}}{t^{7/15}}. \tag{3.31}$$

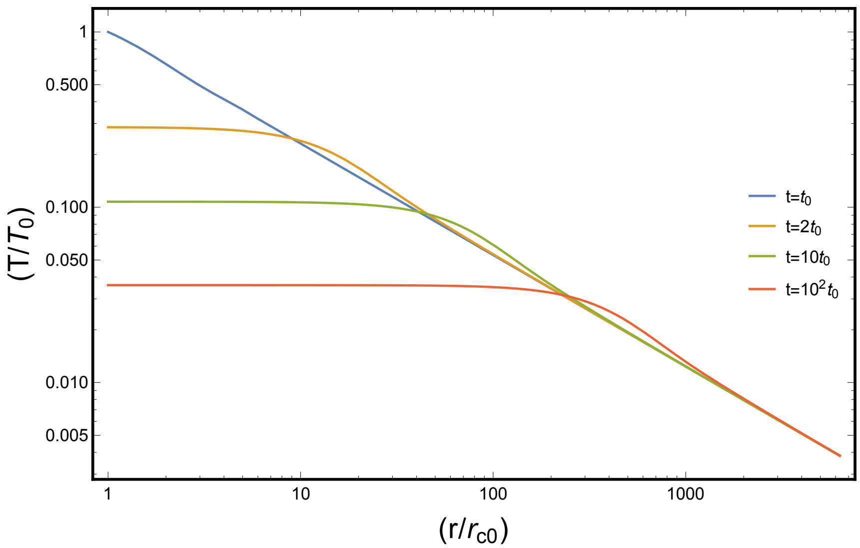

Figure 3.2: Temperature profile at different times where we have defined $r_{c0} = r_c(t_0)$. The initial profile follows Eq. 3.29. As time progresses, the constant temperature region slowly expands without affecting the outside temperature significantly.

Using the results of Eq. 3.31 and Eq. 3.22, we find that the late-time cooling profile is

$$T_{in}(t) = 0.072 \left(c_\alpha^{6/5} g_*(T)^{1/3} G_f^{2/15} \right) \frac{M_{pl}^{8/15}}{t^{7/15}}. \tag{3.32}$$

This equation tells us how fast the plasma surrounding the black hole cools through the phase transition, which in turns determines the number of monopoles produced per black hole. The longer the system remains in the symmetry restored phase, the fewer topological defects produced.

3.3 Monopoles From Black Holes

In this section, we apply our knowledge of the temperature profile around a black hole to calculate the number of monopoles produced per black hole.

3.3.1 The Kibble-Zurek Mechanism

The basic mechanism by which monopoles are produced is the Kibble-Zurek mechanism. In this sub-section, we provide a brief review of the Kibble-Zurek mechanism as applied to thermal systems that are slowly cooling down [130].

In many thermal systems, the high temperature limit involves a symmetry unbroken phase while the low temperature limit involves a symmetry broken phase. Consider a hot plasma in the symmetry unbroken phase. As a hot plasma cools, spontaneous symmetry breaking occurs through the condensation of a scalar order parameter Φ. When this happens, Φ randomly chooses an expectation value somewhere along its vacuum manifold. Regions of space separated by distances longer than the correlation length ξ will obtain different values of Φ. By random chance, these regions of space can accidentally form topologically non-trivial objects such as monopoles. As a result, in a region of size R

$$N_M \sim \frac{R^3}{\xi^3} \tag{3.33}$$

monopoles are created. It is not obvious what the value of the proportionality constant in front of Eq. 3.33 is, so for simplicity we will take it to be 1.

If the phase transition is first order, then over most of the parameter space a single bubble will nucleate and devour the entire space R before a second bubble has a chance to form. Depending on how this bubble interacts with the outside low temperature region, there will be at best $\mathcal{O}(1)$ number of monopoles created. It is plausible that no monopoles will be created. In some corners of parameter space, either because the bubble nucleation rate is highly sensitive to temperature or because the bubbles expand extremely slowly, it is possible that $\xi \lesssim R$, however this is not generically the case and thus we will instead consider second order phase transitions.

If the phase transition is second order, then we can have the situation where $\xi \ll R$ and a much larger number of monopoles can be created. We can characterize how close a second order phase transition is to the critical temperature T_{PT} with a parameter ϵ

$$\epsilon = \frac{T - T_{PT}}{T_{PT}}. \tag{3.34}$$

It is sometimes also convenient to express this parameter in terms of the time to the phase transition t and the characteristic cooling time of the phase transition τ_{char}

$$\epsilon \sim \frac{t}{\tau_{\text{char}}}. \tag{3.35}$$

The correlation length and time are

$$\xi \sim l_0 \epsilon^{-\nu} \qquad \tau \sim \tau_0 \epsilon^{-\mu} \tag{3.36}$$

where l_0 and τ_0 are typical time and length scales in the problem. The system freezes in place when the time to the phase transition t is of order the relaxation time

$$t \sim \tau \qquad \tau_{\text{char}} \epsilon \lesssim \tau_0 \epsilon^{-\mu}, \tag{3.37}$$

where we have used Eq. 3.35 and Eq. 3.36. Solving for ϵ and plugging it back into Eq. 3.36, we find

$$\xi \sim l_0 \left(\frac{\tau_{\text{char}}}{\tau_0} \right)^{\frac{\nu}{1+\mu}} . \tag{3.38}$$

In the case of a plasma slowly cooling in time, the correlation length and time are governed by the mass of the radial mode. Expanding the mass squared in a Taylor series around T_{PT}, we find

$$\xi, \tau \sim \frac{1}{m(T)} \sim \frac{1}{\sqrt{\frac{dm^2(T)}{dT} (T - T_{PT})}} \sim \frac{1}{T_{PT}\sqrt{\epsilon}}. \tag{3.39}$$

Thus we are interested in the scenario where $l_0, \tau_0 \sim 1/T$ and $\nu = \mu = 1/2$ so that Eq. 3.38 gives

$$\xi = \frac{\beta}{T} \left(T \tau_{\text{char}}\right)^{1/3} , \tag{3.40}$$

where β is a proportionality constant and without considering a specific model, it is impossible to specify the value of β. In the case of a weakly coupled scalar whose thermal mass comes from a quartic coupling (λ), we have $\beta \sim 1/\lambda^{1/3}$ and so β can potentially be parametrically larger than $\mathcal{O}(1)$ in the small λ limit. When estimating monopole production later on, we will take $\beta = 1$ with the understanding that there is some model dependence in the estimate.

3.3.2 Kibble-Zurek Around Black Holes

We are now in a position to estimate how many monopoles are produced per black hole. The mechanism of monopole production is that each black hole heats up the surrounding plasma to a temperature profile shown in Eq. 3.12. After the black hole has evaporated, it cools down with a characteristic time scale shown in Eq. 3.28. As the plasma cools past the phase transition temperature, the Kibble-Zurek mechanism generates some number of monopoles. As mentioned before, if the phase transition was first order, then there are generically at most $\mathcal{O}(1)$ and possibly no monopoles produced per black hole.

The more interesting case is if the phase transition was second order. Let us take the phase transition to occur at a scale T_{PT}. Using Eq. 3.12, the radius of the region with $T > T_{PT}$ is

$$R_{PT} \sim \frac{M_{pl}^{4/7}}{T_{PT}^{11/7}}. \tag{3.41}$$

Meanwhile, the characteristic timescale associated with cooling can be read off of Eq. 3.28

$$\tau_{\text{char}} \sim \frac{M_{pl}^{8/7}}{T_{PT}^{15/7}}. \tag{3.42}$$

Using Eq. 3.40, we find that the number of monopoles produced per black hole is

$$N_m \sim \frac{R_{PT}^3}{\xi^3} \sim \left(\frac{M_{pl}}{T_{PT}}\right)^{4/7}. \tag{3.43}$$

Thus a significant number of monopoles can be potentially produced per black hole.

3.4 Bounds on Reheating from Black Holes

In this section, we place reheating bounds on the scenario where the decay of a population of black holes with the same mass reheats the universe. Because each black hole can produce many monopoles, monopoles have the possibility of overclosing the universe.

We estimate the bounds on the reheating temperature in two steps. We first omit all $\mathcal{O}(1)$ numbers in order to emphasize the scaling behavior. Afterwards, we redo the estimate using all of the $\mathcal{O}(1)$ numbers.

If black holes are responsible for reheating the universe, the black holes decay when

$$H^2 \sim \frac{T_{RH}^4}{M_{pl}^2} \sim \frac{1}{t_{BH}^2} \sim \frac{M_{pl}^8}{M_{BH}^6}. \tag{3.44}$$

Using this, the number density of black holes over the number density of photons is given by

$$Y_{BH} = \frac{n_{BH}}{s} \sim \left(\frac{T_{RH}}{M_{pl}}\right)^{5/3}. \tag{3.45}$$

Bounds on overclosing the universe can be obtained by requiring that the energy density in monopoles, MN_mY_{BH} is smaller than roughly five times the energy density in baryons [151], m_BY_B. Taking the mass of the monopole M to be 100 T_{PT} and using Eq. 3.43 for N_m, we find the bound on the reheat temperature to be

$$T_{RH} \lesssim 500\,\text{GeV}\left(\frac{10^{15}\,\text{GeV}}{T_{PT}}\right)^{9/35} \qquad \mathcal{O}(1)\text{ Estimate}. \tag{3.46}$$

This shows that we can expect a very strong bound on the reheat temperature in these scenarios.

Now we produce a more refined estimate by keeping all $\mathcal{O}(1)$ numbers. Using the results of Sec. 3.2, Eq. 3.41 and Eq. 3.42 with $\mathcal{O}(1)$ numbers become

$$\begin{aligned} R_{PT} &= 0.07\left(\frac{c_\alpha^2 G_f}{g_*}\right)^{1/7}\left(\frac{M_{pl}^{4/7}}{T_{PT}^{11/7}}\right) \\ \tau_{\text{char}} &= 0.008\left(c_\alpha^{18} g_*^5 G_f^2\right)^{1/7}\left(\frac{M_{pl}^{8/7}}{T_{PT}^{15/7}}\right). \end{aligned} \tag{3.47}$$

Using these equations, we can calculate the numerical coefficient in Eq. 3.43 and find

$$N_m = 0.044\left(\frac{G_f}{c_\alpha^{12} g_*^8}\right)^{1/7}\left(\frac{M_{pl}}{T_{PT}}\right)^{4/7}. \tag{3.48}$$

For the last step, we assume that black holes decay instantaneously when $H = 1/t_{BH}$. Using the fiducial values $G_f = 3.8$, $g_*(T_{PT}) = 108$, $c_\alpha = 1/10$ and $M = 25\,T_{PT}$ at the unification scale, we arrive at

$$T_{RH} \lesssim 672\,\text{GeV}\left(\frac{10^{15}\,\text{GeV}}{T_{PT}}\right)^{9/35}. \tag{3.49}$$

Thus we see that having a large reheat temperature runs the risk of over-producing monopoles.

3.5 Realm of validity

In this section, we discuss the various approximations that go into our result and the limitations placed on our result by these approximations.

3.5.1 Model dependent factors

Many of our results depend to some degree on the model dependent factors c_α, β, $g_\star(T)$ and G_f. Of these, it is expected that $g_\star$ and G_f change by at most $\mathcal{O}(1)$ and thus do not change the final results by much. On the other hand, it is possible for c_α and β to change by more than an order of magnitude and can thus change the final result more significantly.

As mentioned before, a major source of uncertainty comes from the the correlation length at criticality, ξ. β appears as a proportionality constant in Eq. 3.40 and its value depends on the Grand Unified Theory under consideration. The expectation is that $\beta \gtrsim \mathcal{O}(1)$. While the exact value of β is unknown, the parametric dependence of our final reheat temperature on β is easily calculated. A larger correlation length decreases the abundance of magnetic monopoles which makes the bound on T_{RH} weaker. It is easy to verify that the monopole abundance decreases by an amount $1/\beta^3$ which weakens the bound on the reheat temperature by $\beta^{9/5}$ in Eq. 3.49.

$$T_{RH} \lesssim 672\,\mathrm{GeV}\,\beta^{\frac{9}{5}} \left(\frac{10^{15}\,\mathrm{GeV}}{T_{PT}}\right)^{9/35} . \tag{3.50}$$

The other important model dependent quantity is c_α, which characterizes the typical size of the scattering cross sections. c_α is important because scattering is responsible for the diffusion of energy, which affects the profile. We have defined the typical interaction cross section σ as

$$\sigma \equiv \frac{c_\alpha^2}{T^2} \tag{3.51}$$

in the high energy limit. Larger c_α give shorter diffusion lengths and so that energy diffuses out more slowly. As a result, in equilibrium the temperature distribution changes more gradually and there is a larger volume at higher temperature. But larger c_α (slower diffusion) also hinders cooling which makes the correlation length at freeze out at larger values. Between these two effects, the effect on the correlation length is stronger as can be seen in Eq. 3.48. As a result of this, the final bound on the reheat temperature scales as

$$T_{RH} \lesssim 672\,\mathrm{GeV}\,\beta^{9/5}\left(\frac{g_*(T_{PT})}{108}\right)^{11/14}\left(\frac{G_f}{3.8}\right)^{4/35}(10c_\alpha)^{36/35}\left(\frac{10^{15}\,\mathrm{GeV}}{T_{PT}}\right)^{9/35}. \tag{3.52}$$

As will be shown later, a critical assumption of our derivation is that the thermal bath is in equilibrium with the evaporating black hole. The validity of this assumption is c_α dependent and may be where the uncertainty in c_α is most important.

3.5.2 Hierarchy of length scales

In our previous derivation, it was tacitly assumed that $R_{PT} > \xi$ and $\xi > r_m$, where r_m is the size of the monopole. In this subsection, we discuss the validity of these assumptions. Our work is based on the premise that an evaporating BH will heat up a large volume of the surrounding plasma, where the phase transition can take place and produce topological defects. This assumes that the size of the region that attains temperatures above T_{PT} is larger than the correlation length, namely $R_{PT} > \xi$. In the limit that $R_{PT} < \xi$, then like first order phase transitions, either $\mathcal{O}(1)$ or zero monopoles will be produced and our estimate would need to be modified.

The second inequality comes from the fact that the monopole is an extended object with a characteristic length scale r_m. We assumed that one monopole was produced per volume ξ^3, an assumption only valid if $\xi > r_m$. In the limit $\xi < r_m$ there is one monopole produced per r_m^3 instead of ξ^3, and the estimate must be modified.

The temperature dependence of R_{PT} and ξ can be seen in Eq. 3.40 and Eq. 3.41, namely $R_{PT} \sim T_{PT}^{-11/7}$ and $\xi \sim T_{PT}^{-29/21}$. Meanwhile, the radius of the monopole scales with its mass as $r_m \sim T_{PT}^{-1}$. Putting in the relevant pre-factors, we find

$$R_{PT} = 0.07 \left(\frac{c_\alpha^2 G_f}{g_*}\right)^{1/7} \left(\frac{M_{pl}^{4/7}}{T_{PT}^{11/7}}\right) \qquad \xi = 0.20 \left(c_\alpha^{18} g_*^5 G_f^2\right)^{1/21} \left(\frac{M_{pl}^{8/21}}{T_{PT}^{29/21}}\right). \tag{3.53}$$

From this, we see that R_{PT} falls off fastest with increasing phase transition temperature while ξ and r_m decrease more slowly. Depending on the value of $g_*(T)$ and c_α, one of either $R_{PT} > \xi$ or $\xi > r_m$ is more important. Combining the two, we find that as long as

$$T_{PT} < \begin{cases} 1.37 \times 10^{16}\,\text{GeV} \left(\frac{108}{g_*(T_{PT})}\right)^2 \left(\frac{G_f}{3.8}\right)^{1/4} \left(\frac{0.076}{c_\alpha}\right)^3, & \text{if } g_*(T) c_\alpha^2(T) \geq 0.63 \\ 1.37 \times 10^{16}\,\text{GeV} \left(\frac{g_*(T_{PT})}{108}\right)^{5/8} \left(\frac{G_f}{3.8}\right)^{1/4} \left(\frac{c_\alpha}{0.076}\right)^{9/4}, & \text{otherwise} \end{cases} \tag{3.54}$$

our assumptions ($R_{PT} > \xi > r_m$) are valid. For our fiducial parameters, $g_*(T)c_\alpha^2 = 1.08$, the conditions are safely satisfied for $T_{PT} < 6.1 \times 10^{15}$ GeV.

3.5.3 Thermal equilibrium

Throughout our work, we have assumed thermal equilibrium. There are several areas where the approximation of thermal equilibrium break down. For example if the temperature is changing on length scales shorter than the scattering length, then it is clear that thermal equilibrium is breaking down. In the context of monopole production, the most important and constraining assumption that was made was the assumption that that the energy emitted by the black hole is in thermal equilibrium with the surrounding plasma.

The Hawking radiation emitted by the black hole only reaches thermal equilibrium when it has lost all of its energy. All of the Hawking radiation eventually scatters and loses its energy, so for a large enough radius, we expect the thermal equilibrium condition to hold. We will thus assume the equilibrium configuration to hold until some critical radius r_{th} inside of which the system is not in thermal equilibrium. The equilibrium temperature distribution can be found by requiring that the power passing through the temperature distribution match the power emitted by the black hole, $rT(r)^3 \sim T_{BH}^2$.

As the radiation emitted by the black hole with energy E passes through the plasma, it loses energy through its interaction as described in Eq. 3.2

$$\partial_r E = -n\,\sigma\,E \sim T^2. \tag{3.55}$$

While the number density of the thermal bath scales as $n \sim T^3$, the cross section of a high energy particle scales as $\sigma \sim 1/s \sim 1/TE$ resulting in a constant energy loss of order T^2 when moving through the plasma. Hawking radiation loses all of its energy after traveling a distance

$$r_{th} \sim \frac{T_{BH}}{T(r_{th})^2} \qquad\qquad r_{th} \sim \frac{1}{T_{BH}}. \tag{3.56}$$

Since $\partial_r E \sim -T^2$, high energy particles travel longer before they they thermalize. Averaging over the energies in the relativistic limit, we get the following $\mathcal{O}(1)$ factors

$$r_{th} \approx \frac{1.3 \times 10^6}{T_{BH}} \left(g_*(T)c_\alpha^2\right)^{-3} \qquad T(r_{th}) \approx 0.004\, T_{BH}\, g_*(T)c_\alpha^2. \tag{3.57}$$

From this, we can see that unless one is interested in temperatures close to T_{BH}, the assumption of thermal equilibrium is good.

We can finally use Eq. 3.57 to find a maximum for T_{PT}. Given that we assumed that the system was in equilibrium when T_{PT} froze out, we can require that $R_{PT} > r_{th}$ when the T_{PT} froze out. Imposing this requirement gives

$$T_{PT} \lesssim 1.94 \times 10^{15} \left(\frac{g_*(T)c_\alpha^2}{1.08}\right) \text{GeV}. \tag{3.58}$$

which is satisfied for our choice of T_{PT}.

3.5.4 Evaporation of Black Holes

If thermal equilibrium was maintained all the way to the surface of the black hole, then the evaporation of the black hole would be greatly affected. In thermal equilibrium, radiation into and out of the black hole would roughly balance and only temperature gradients give rise to an outflow of energy. As was demonstrated in the previous subsection, the area right outside of the black hole is not in thermal equilibrium with the black hole itself. As a result, its temperature is lower than the black hole temperature, see e.g. Eq. 3.57. Thus the energy falling into the black hole, $r_{BH}^2 T(r_{th})^4$, is subdominant to the energy being emitted by the black hole, $r_{BH}^2 T_{BH}^4$. As such, we can treat the black hole as evaporating the same as it would in vacuum.

3.5.5 Reaching thermal equilibrium

When the black holes first start evaporating, they are not in equilibrium with the external radiation. In this subsection, we estimate the time it takes for the plasma surrounding the black hole to reach an equilibrium state.

When the thermal profile is close to the equilibrium profile, the black hole's ability to heat the surrounding plasma is limited by diffusion. Following the argument in Sec. 3.2.2, we find

$$r_d^2 \sim \lambda t \qquad r_d \sim \frac{t^{11/15}}{M_P^{4/15}}. \tag{3.59}$$

As long as the black hole is depositing energy in a radius smaller than r_d, then in a time t, the region of space with $r < r_d$ will be in equilibrium with the black hole.

Initially, the plasma surrounding the black hole has an initial temperature T_{RH}. The Hawking radiation emitted by the black hole loses all of its energy after a distance, see Eq. 3.2,

$$r_i \sim \frac{T_{BH}}{T_{RH}^2}. \tag{3.60}$$

This is the radius at which the black hole first starts to deposit its energy. As the temperature rises, it deposits energy closer and closer to the black hole. As long as $r_i < r_d(t)$, the black hole will have reached equilibrium with the plasma immediately around it. Equilbrium is first reached when $r_i \sim r_d(t_i)$ giving

$$t_i \sim \frac{T_{BH}^{15/11} M_P^{4/11}}{T_{RH}^{30/11}}. \tag{3.61}$$

When black holes are reheating the universe, t_i and T_{RH} are set by the lifetime of the black holes and Hubble. Comparing the two timescales, we find

$$t_i \sim t_{BH} \left(\frac{T_{BH}}{M_P}\right)^{3/11} < t_{BH} \tag{3.62}$$

showing that the plasma around the black hole does indeed have time to reach equilibrium with the black hole. For our choice of parameters, the $O(1)$ number in Eq. 3.62 is 0.9, which validates our assumption that the black hole reaches thermal equilibrium with its surrounding.

3.6 Conclusion

In this article, we explored the evaporation of black holes in the early universe and showed how they heat up the surrounding plasma. This plasma can reach temperatures much larger than the ambient temperature and can have effects more significant than that of the black hole itself. As an example, while monopole production by black hole evaporation is negligible, monopole production by the surrounding plasma can be very significant. This efficient mechanism of monopole production can be significant enough that it can easily overclose the universe if the reheat temperature is larger than $T_{RH} \gtrsim 500$ GeV. Such a low reheat temperature motivates black hole centric mechanisms of baryogenesis.

The evaporation of black holes in the early universe is an intriguing possibility. We have only listed a single scenario where the plasma surrounding the black hole has a significant effect. It would be interesting if there are other situations where this plasma is important.

Chapter 4: Constraining Vector Dark Matter with Neutrino experiments

This work was done in collaboration with Dawid Brzeminski, Anson Hook, Clayton Ristow and has been submitted for publication.

4.1 Overview

Determining the microscopic properties of dark matter is among the greatest puzzles in modern physics. There is overwhelming evidence [152, 153, 154] for the existence of dark matter (DM) but many of its basic properties, such as its mass, spin and interactions remain completely unknown.

In this article, we will focus on Ultralight Dark Matter (ULDM). ULDM are well-motivated DM candidates [155, 156] with rich experimental signatures. Due to their very low mass, the number of particles per Compton volume is large, $n_{DM}\lambda^3_{\text{Compton}} \gg 1$, which allows us to treat them as a classical field rather than as a set of particles. As the local DM field has an average velocity of $v \sim 10^{-3}$, the field's energy dispersion is very small, $\Delta E \sim mv^2 = 10^{-6}m$ and the field changes over very long length scales $l \sim 1/p \sim 10^{-3}/m$. As a result, we can approximate the field as coherently oscillating with the frequency $\omega = m$ until timescales of order $t_{\text{coh}} \sim (mv^2)^{-1} = 10^{-6}m^{-1}$ before the frequency spread becomes important. The long coherence length and time of dark matter lead to unique signatures. When the dark matter mass is so small that the long coherence length wipes out structure on observably small length scales, "fuzzy dark matter" phenomenology kicks in [157, 158, 159, 160]. Additionally, the oscillation in time of the dark matter field can lead to observable time-dependent effects if DM couples to the Standard Model (SM) [161, 162, 163, 164, 165, 166, 167]. For instance, ULDM QCD axions [50, 168, 169] result in the electric dipole moment of the neutron varying with the frequency of the axion mass [170, 171].

In this work, we focus on a spin one ULDM ($\vec{A}_d$), for related work see Refs. [172, 173, 174, 175, 176]. The main difference between scalars and vectors is polarization. Much like the amplitude of the field, the polarization changes direction on timescales of order t_{coh}. For sufficiently long DM coherence times, earth-based experiments sensitive to the direction of the polarization would see the polarization of dark matter rotating as the Earth spins around its axis. This would introduce a daily modulated feature on top of the standard oscillation with the frequency of the dark matter mass, which is a signature that can be used to distinguish scalar from vector DM. Additionally, experiments with angular resolution would see strong directional dependence.

Neutrino oscillations are uniquely suited for exploring dark matter interactions. As long as the interactions are flavor non-universal, neutrino oscillations are sensitive to energy differences of the order $\Delta m_\nu^2/E \sim 10^{-12}$ eV, over 15 orders of magnitude more sensitive than traditional dark matter detectors. The requirement that the interaction is flavor non-universal combined with our focus on VDM immediately leads us to consider $U(1)_{L_\mu - L_\tau}$ and $U(1)_{L_e - L_\mu}$.

New vectors interacting with the SM are extremely common. Kinetic mixing with the SM photon, gauging $U(1)_{B-L}$ or $U(1)_{L_\mu - L_\tau}$ are among the most commonly considered scenarios [15, 177, 178, 179]. The $U(1)_{L_\mu - L_\tau}$ and $U(1)_{L_e - L_\mu}$ gauge bosons that we consider have a plethora of interesting implications for neutrino physics [44, 45, 46, 47, 48, 49, 180, 181, 182, 183, 184, 185, 186, 187, 188, 189].

A background of $U(1)_{L_\mu-L_\tau}$ ($U(1)_{L_e-L_\mu}$) gauge bosons acts as a time-dependent potential that is flavor non-universal. As neutrinos and antineutrinos have opposite charges under a vector background, the potential is opposite for matter and antimatter. Additionally, the effect is proportional to the dot product of the neutrino velocity with the polarization of dark matter resulting in a directionally dependent chemical potential. If the dark matter oscillations are slow compared to the neutrino propagation timescale, the effect on neutrino oscillations is similar to the MSW matter effect [34, 35, 190]. Therefore, the main signature of these models are time-dependent neutrino oscillation parameters, e.g. $\Delta m^2_{31}(t)$ and $\sin\theta_{13}(t)$. Measurement of these signatures might be challenging due to a low neutrino event rate. However, we show that even after averaging over the duration of the experiment, the effect is strong enough to place bounds several orders of magnitude better than the leading bounds on $U(1)_{L_e-L_\mu}$ and $U(1)_{L_\mu-L_\tau}$ dark matter. A similar bound on $U(1)_{L_\mu-L_\tau}$ from neutrino oscillation experiments was estimated in [191] for the scenario where the vector field is a relic field used to facilitate the production of sterile neutrino dark matter in the early universe.

If the dark matter oscillations are fast compared to the neutrino propagation timescale, the neutrinos experience a rapidly oscillating effective chemical potential. Because this potential oscillates rapidly, to the lowest order the effective potential averages to zero over the neutrino propagation time. Thus, the leading effects are suppressed by an additional factor of m^{-1}, where m is the oscillation rate of the background dark matter field. The fact that our bounds on $U(1)_{L_e-L_\mu}$ and $U(1)_{L_\mu-L_\tau}$ scale by an additional factor of m^{-1} in the high mass regime reflects this chemical potential washout effect.

The goal of this paper is to explore the sensitivity of various neutrino oscillation experiments to $U(1)_{L_\mu - L_\tau}$ ($U(1)_{L_e - L_\mu}$) DM. In section 4.2, we review the phenomenology of neutrino oscillations and introduce the effect of vector DM on neutrino oscillations. In section 4.3, we constrain the model using existing and planned neutrino experiments. We conclude with section 4.4 and propose further avenues of research.

4.2 Model

We start with a brief description of gauging lepton flavor and its effect on neutrinos. The three individual lepton flavor numbers $L_\alpha,\ \alpha = e, \mu, \tau$, can be equivalently described in a different basis comprising of the total lepton number $\sum_\alpha L_\alpha = L$ and two lepton number differences, which we choose to be $L_e - L_\mu$ and $L_\mu - L_\tau$ without any loss of generality. The total lepton number charge L is the identity in the flavor space and gives an equal phase to neutrinos of all flavors and hence is unobservable in neutrino oscillations. Therefore we restrict our discussion to $L_e - L_\mu$ and $L_\mu - L_\tau$.

To the Standard Model, we add a single gauge boson $A_{d\,\mu}$ which gauges either of the two flavor lepton number differences.

$$\begin{aligned}
\mathcal{L} &\subset -\frac{1}{4} F_{d\,\mu\nu} F_d^{\mu\nu} - \frac{1}{2} m_A^2 A_{d\,\mu} A_d^\mu + \mathcal{L}_{int,e-\mu} + \mathcal{L}_{int,\mu-\tau} \\
\mathcal{L}_{int,e-\mu} &= -g A_{d\,\sigma} \left(\overline{l_e} \gamma^\sigma l_e - \overline{l_\mu} \gamma^\sigma l_\mu \right) \\
\mathcal{L}_{int,\mu-\tau} &= -g' A_{d\,\sigma} \left(\overline{l_\mu} \gamma^\sigma l_\mu - \overline{l_\tau} \gamma^\sigma l_\tau \right)
\end{aligned} \tag{4.1}$$

where m_A is the mass of the gauge field, g and g' denote coupling to the $L_e - L_\mu$ and

$L_\mu - L_\tau$ charges respectively and $l_{e,\mu,\tau}$ denotes leptons with e, μ, τ charges. For example, l_e denotes electrons, electron neutrinos and their anti-particles.

We now consider the consequences of the vector boson $A_{d\,\mu}$ being dark matter. The three polarizations of a massive gauge field satisfy $p_\mu \epsilon^\mu = 0$. If the gauge bosons were at rest, the three polarizations would simply be unit vectors in the x, y, and z directions. Including a non-zero velocity along the z-axis and considering the longitudinal polarization $\epsilon_L = \frac{1}{m_A}(p, 0, 0, E)$ we see that the temporal component of the vector field $A_{d\,0}$ is subdominant to the spatial components $A_{d\,i}$ by a factor of DM velocity $v_{DM} \sim 10^{-3}$. To leading order the galactic DM field can be written as an oscillating three vector with frequency $\omega \sim m_A + \mathcal{O}(v_{DM}^2)$

$$\vec{A}_d = \vec{A}_0 \cos\left(m_A(t + \vec{v}_{DM} \cdot \vec{x}) + \phi\right) + \mathcal{O}(v_{DM}^2), \tag{4.2}$$

where $|\vec{A}_0| = \sqrt{2\rho_{DM}/m_A^2}$ and m_A is the mass of the DM. Since the neutrinos are relativistic, the interactions in Eq. 4.1 can be written for neutrinos as

$$H_{\text{int}} = \vec{A}_d \cdot \vec{v}_\nu \begin{pmatrix} g & 0 & 0 \\ 0 & g' - g & 0 \\ 0 & 0 & -g' \end{pmatrix} + \mathcal{O}(v_{DM}) \tag{4.3}$$

where $\vec{v}_\nu$ is the neutrino velocity. The dark matter shifts the relative energies of different neutrino flavor eigenstates. For example, in the case where the dark matter is the gauge boson of $L_e - L_\mu$, the dark matter creates an energy difference between the electron neutrino ν_e and muon neutrino ν_μ. The vector nature of the interaction means it has opposite signs for neutrinos and anti-neutrinos. The dark matter thus acts as a chemical potential for the neutrinos. This can be contrasted with the effect of a scalar field which does not distinguish between particles and antiparticles.

It is important to note the directional dependence of the interaction. The interaction picks the polarization of the DM along the neutrino velocity. In neutrino beam experiments, where the neutrino velocity has a fixed orientation with respect to the Earth's frame, the direction of the neutrino velocity rotates with the Earth over the course of a day. This produces a daily modulation of the DM effect. This is in contrast with the effect produced by a scalar field where no such directional dependence exists and can be used to distinguish between the two. We explore this effect in more detail in Sec. 4.2.3

4.2.1 Neutrino Oscillations

Within the Standard Model, neutrino oscillations are controlled by two contributions, the vacuum Hamiltonian H_{vac} and the MSW effect [34, 35]. In absence of any matter, the neutrino oscillation is set by the neutrino energy, the mass squared difference and the rotation matrix between the mass and the flavor eigenstates, U_{PMNS}. In the relativistic limit, we can expand the Hamiltonian in powers of m_ν/E_ν where m_ν denotes the mass of a generic mass eigenstate and E_ν is the neutrino energy. The non-identity piece of the vacuum Hamiltonian can be written as

$$H_{\text{vac}} = U_{PMNS} \left[\frac{1}{2E_\nu} \begin{pmatrix} 0 & 0 & 0 \\ 0 & \Delta m_{21}^2 & 0 \\ 0 & 0 & \Delta m_{31}^2 \end{pmatrix} \right] U_{PMNS}^\dagger \tag{4.4}$$

where $\Delta m^2_{ij} = m^2_i - m^2_j$ are the neutrino mass differences and we have removed the pieces proportional to the identity that do not contribute to oscillations.

On the other hand, in the presence of matter, for example while propagating through the Earth, the interaction of the neutrinos with matter creates a chemical potential for the neutrinos. In the presence of protons, neutrons and electrons, the only non-identity interaction in flavor space is a chemical potential for the electron neutrinos.

$$H_{\text{MSW}} = \pm\sqrt{2}G_F n_e(x) \begin{pmatrix} 1 & 0 & 0 \\ 0 & 0 & 0 \\ 0 & 0 & 0 \end{pmatrix} \tag{4.5}$$

where G_F is the Fermi constant, $n_e(x)$ is the number density of electrons and the $+$ $(-)$ sign is for neutrinos (anti-neutrinos). The neutrino oscillations we observe in neutrino experiments are an interplay between the vacuum oscillation and the effect of matter. Experiments that are sensitive to this effect work in the regime $L\Delta m^2_{21}/E_\nu \ll 1$, despite the long distance traveled by neutrinos $L \sim 10^3 - 10^4$ km. As a result, the relevant mixing parameters are reduced to Δm^2_{31}, θ_{13} and θ_{23}. When there is a non-zero number density of electrons, Δm^2_{31} and θ_{13} are replaced by their effective counterparts [190]

$$\Delta m^2_{31,M} = \Delta m^2_{31}\sqrt{(\cos 2\theta_{13} - \Gamma)^2 + \sin^2 2\theta_{13}} \tag{4.6}$$

$$\sin^2 2\theta_{13,M} = \frac{\sin^2 2\theta_{13}}{(\cos 2\theta_{13} - \Gamma)^2 + \sin^2 2\theta_{13}} \tag{4.7}$$

where $\Gamma = \sqrt{2}G_F n_e E_\nu/\Delta m^2_{31}$. When $\Gamma = \cos 2\theta_{13}$, magnitudes of H_{vac} and H_{MSW} are comparable, which significantly changes mass eigenstates. This leads to enhanced oscillations into electron neutrinos at distances of order $\frac{E\nu}{\Delta m^2_{31,M}}$, which we call resonance.

The effect has important phenomenological consequences. The sign of Γ changes between neutrinos and antineutrinos, and also depends on mass ordering. In the normal ordering, the resonance can only happen for neutrinos, while in the inverted ordering it can only occur for antineutrinos. Therefore, the resonance can be used to solve the mass ordering problem [190].

In the presence of vector dark matter, neutrino oscillations are modified in a similar way. The dark matter contribution (Eq. 4.1) to the neutrino oscillation can be written as[1]

$$H_{\text{int}} = \pm\frac{\sqrt{2\rho}}{m_A}\cos(m_A t+\phi)\cos\alpha(t)\begin{pmatrix} g & 0 & 0 \\ 0 & g'-g & 0 \\ 0 & 0 & -g' \end{pmatrix} \tag{4.8}$$

where g and g' denote coupling to the $L_e - L_\mu$ and $L_\mu - L_\tau$ charges respectively, ρ is the DM energy density, m_A is the mass of the vector DM and $\alpha(t)$ is the angle between DM polarization and the neutrino velocity. The total Hamiltonian governing neutrino oscillations is the sum of the parts

$$H = H_{\text{vac}} + H_{\text{MSW}} + H_{\text{int}}. \tag{4.9}$$

In order to see the effect of the VDM is similar to the matter effect, let us set $g = 2g'$. Then, the non-identity piece of H_{int} has the same matrix structure as Eq. (4.5). In the $L\Delta m^2_{21}/E_\nu \ll 1$

[1]Although the DM phase changes both in space and time, as in Eq. 4.2, the neutrino baseline is much smaller than the coherence length so that the change in phase is suppressed by the small DM velocity. Hence we only keep the leading time-dependent piece.

limit this leads to a time-dependence of the effective Δm^2_{31} and θ_{13}

$$\Delta m^2_{31,DM} = \Delta m^2_{31}\sqrt{(\cos 2\theta_{13} - \Gamma - \Gamma_{DM}(t))^2 + \sin^2 2\theta_{13}} \tag{4.10}$$

$$\sin^2 2\theta_{13,DM} = \frac{\sin^2 2\theta_{13}}{(\cos 2\theta_{13} - \Gamma - \Gamma_{DM}(t))^2 + \sin^2 2\theta_{13}} \tag{4.11}$$

where $\Gamma_{DM}(t) = \frac{3g\sqrt{\rho}E_\nu}{\sqrt{2}m\Delta m^2_{31}}\cos(mt+\phi)\cos\alpha(t)$. Therefore, we can see that experiments which are sensitive to the matter effect should also be able to measure the effect caused by DM. The only qualitative difference is that in this scenario the time-averaged effect is the same for neutrinos and anti-neutrinos, which is a feature that could be used to differentiate the DM-induced effect from the matter effect.

4.2.2 Simplified model with two flavors

To gain some insight into the effect of vector dark matter on neutrino oscillation, we consider a toy model of two neutrino flavors. For clarity, we ignore the matter effect as it does not affect our conclusions. The model is characterized by a single neutrino mass squared difference, which we denote by Δm^2, the neutrino energy E_ν and the dark matter mass and coupling, m_A and g.

$$\begin{aligned} H &= U\frac{\Delta m^2}{4E_\nu}\sigma_z U^\dagger + \frac{g\sqrt{2\rho}}{m_A}\sigma_z\cos(m_A(t-t_0)+\phi(t_0)) + \mathcal{O}(v_{\text{DM}}) \\ &= U\Delta_\nu\sigma_z U^\dagger + gA_0\sigma_z\cos(m_A(t-t_0)+\phi(t_0))\,, \end{aligned} \tag{4.12}$$

where σ_z is the third Pauli Matrix, U is the PMNS matrix for two flavors, $\Delta_\nu \equiv \frac{\Delta m^2}{4E_\nu}$ controls the neutrino vacuum Hamiltonian, $A_0 = \frac{\sqrt{2\rho}}{m_A}$ is the vector amplitude, $\phi(t_0) = m_A t_0 + \phi_0$ is the

DM phase at the point of neutrino production and t_0 denotes the time of neutrino production. We have also neglected the dot product of the polarization and the neutrino velocity which changes due to Earth's rotation. We discuss this effect in detail in Sec. 4.2.3.

Let us first consider the time dependence of the DM effect. Due to stringent constraints, the DM effect is subdominant to the vacuum oscillation and can be treated using perturbation theory. The transition probability between the flavor states can be written as

$$P_{\nu_e \to \nu_\mu} = P^{(0)} + P^{(1)} + P^{(2)} + \cdots , \tag{4.13}$$

where we have labeled the two flavor states as ν_e and ν_μ, $P^{(1)}$ and $P^{(2)}$ are the first and second order correction to the oscillation probability due to dark matter, $P^{(n)} \propto g^n$. The first order correction, $P^{(1)}$, only contains contributions as $\sin(m_A L + \phi(t_0))$, where L denotes the baseline of the experiment. This term oscillates as the initial phase $\phi(t_0)$ changes as a function of neutrino production time t_0. If an experiment has sufficient statistics, they can look for the oscillating first-order correction. On the other hand, if the experiment only observes time-averaged quantities, we will instead be sensitive to the second order correction, $P^{(2)}$, which includes terms like $\sin^2(m_A L + \phi(t_0))$. These do not average to zero in contrast with the first-order correction. Then,

$$\langle P_{\nu_e \to \nu_\mu} \rangle = P^{(0)} + \langle P^{(2)} \rangle + \cdots , \tag{4.14}$$

where $\langle \rangle$ denotes averaging over the lifetime of the experiment. We compute $\langle P^{(2)} \rangle$ using time-dependent perturbation theory.

$$\langle P^{(2)}\rangle = -\frac{g^2 A_0^2 \sin^2(2\theta)}{\left(m_A^3 - 4m_A\Delta_\nu^2\right)^2} f(m_A, \Delta_\nu, L)$$

$$f(m_A, \Delta_\nu, L) = 8\Delta_\nu^4 \cos^2(2\theta)\left(\cos\left(L\left(m_A + 2\Delta_\nu\right)\right) + \cos\left(L\left(m_A - 2\Delta_\nu\right)\right) - 2\cos\left(2L\Delta_\nu\right)\right)$$

$$+m_A^4\left(L\Delta_\nu \sin^2(2\theta)\sin\left(2L\Delta_\nu\right) + 2\cos^2(2\theta)\sin^2\left(L\Delta_\nu\right)\right) + 16m_A\Delta_\nu^3\cos^2(2\theta)\sin\left(Lm_A\right)\sin\left(2L\Delta_\nu\right)$$

$$+m_A^2\Delta_\nu^2\left(\cos(4\theta)\left(\cos\left(L\left(m_A + 2\Delta_\nu\right)\right) + \cos\left(L\left(m_A - 2\Delta_\nu\right)\right) - 2\cos\left(Lm_A\right) + 6\cos\left(2L\Delta_\nu\right) - 6\right)\right)$$

$$+m_A^2\Delta_\nu^2\left(\cos\left(L\left(m_A + 2\Delta_\nu\right)\right) + \cos\left(L\left(m_A - 2\Delta_\nu\right)\right) + 2\cos\left(Lm_A\right)\right)$$

$$+m_A^2\Delta_\nu^2\left(-4L\Delta_\nu\sin^2(2\theta)\sin\left(2L\Delta_\nu\right) + 2\cos\left(2L\Delta_\nu\right) - 6\right), \tag{4.15}$$

where θ characterizes the two flavor PNMS matrix U.

This very complicated expression can be greatly simplified in the large or small m_A limits. In the small mass limit, where $m_A \ll 1/L \sim \Delta_\nu$, the effect of dark matter is roughly constant as the neutrinos fly from the point of production to the point of detection. In this limit, the leading correction to the vacuum oscillation is given by

$$\langle P^{(2)}\rangle = g^2\frac{A_0^2\sin^2 2\theta}{8\Delta_\nu^2} \tag{4.16}$$

$$\left(4\cos 4\theta + 2\cos(2\Delta_\nu L)\left(\cos 4\theta(\Delta_\nu^2 L^2 - 2) + \Delta_\nu^2 L^2 - 1\right) - \Delta_\nu L(5\cos(4\theta) + 3)\sin(2\Delta_\nu L) + 2\right).$$

On the other hand in the large mass limit, where $m_A \gg 1/L \sim \Delta_\nu$, the dark matter is oscillating rapidly over the flight of the neutrinos and much of its effect is averaged away. In this limit, the same second-order correction reads

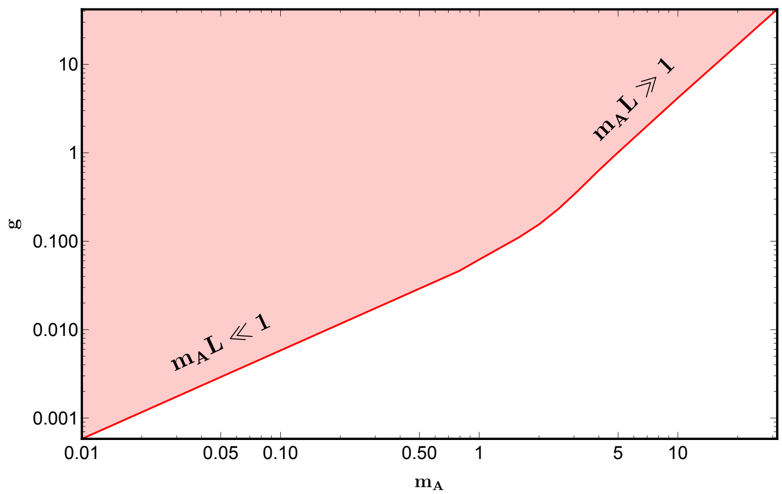

Figure 4.1: We show how the bound on the dark matter gauge coupling as a function of mass (units arbitrary) is expected to behave for hypothetical neutrino oscillation experiments. The two different scaling of the bound for the regimes $m_A L \ll 1$ and $m_A L \gg 1$ is clearly visible. For $m_A L \ll 1$, for a fixed experimental uncertainty, the coupling scales linearly with m_A whereas for $m_A L \gg 1$, the same scaling is quadratic.

$$\langle P^{(2)} \rangle = -g^2 \frac{A_0^2 \sin^2 2\theta}{m_A^2} \left(\Delta_\nu L \sin^2(2\theta) \sin(2\Delta_\nu L) + 2\cos^2(2\theta) \sin^2(\Delta_\nu L) \right) \tag{4.17}$$

From Eq. 4.16 and 4.17, it is easy to see how the bound on the dark matter coupling constant g scales with the mass of dark matter. In the low mass regime, $\sqrt{P^{(2)}} \sim gA_0 \sim \frac{g}{m_A}$, so we expect the constraint to scale as $g \propto m_A$. On the other hand, in the high mass regime, $\sqrt{P^{(2)}} \sim \frac{gA_0}{m_A} \sim \frac{g}{m_A^2}$. Hence the constraint is expected to scale as $g \propto m_A^2$. This scaling behavior can be seen in Fig. 4.1 where we have plotted the bound obtained from a hypothetical neutrino experiment using two neutrino flavors in the perturbative regime. In making this plot, we have assumed $\Delta_\nu \in [1., 2.]$, a fixed experimental uncertainty and considered 10 bins with equal energy spacing (motivated by the DUNE experiment [6, 192, 193]). The difference in the scaling of the bound on the coupling constant is clearly different in the small and large mass ranges. In the low mass regime, $m_A L \ll 1$, the bound increases slowly $g \propto m_A$. On the other hand, in the high mass regime $m_A L \gg 1$ it weakens faster, $g \propto m_A^2$ and smoothly transitions between the two at $m_A L \sim 1$.

In Section 4.3.3, we will use these perturbative results to scale numerically obtained bounds at one mass to other masses. To do this, we will need to be sure that we are in the perturbative regime. We will look at experiments with neutrino energies $E_\nu \sim \mathcal{O}(1 - 10\,\mathrm{GeV})$ at which scale Δm_{13}^2 dominates the oscillation dynamics. By demanding $P^{(2)} \ll 1$, Eq. 4.16 gives a bound on the coupling below which we are working in the perturbative regime:

$$g < 2.5 \cdot 10^{-30} \left(\frac{m_A}{10^{-20}\mathrm{eV}}\right) \left(\frac{\mathrm{GeV}}{E_\nu}\right) \tag{4.18}$$

4.2.3 Daily Modulation

In this section, we discuss the effects of the Earth's rotation on our DM signal. As the DM-induced potential is the dot product between the DM polarization and neutrino velocity, the DM-induced potential undergoes an oscillation due to the Earth's rotation. The equatorial component oscillates whereas the polar components remain unchanged due to the Earth's rotation. This directional dependence is a crucial difference between vector and scalar DM.

For a neutrino beam type experiment, the neutrino beam has a fixed direction in the lab frame. Figure 4.2 shows this in the lab frame. In general, the neutrino beam has a direction

$$\hat{v}_\nu = (v_{||},\ \ v_\perp) \tag{4.19}$$

where $v_{||}$ and $v_\perp$ are the equatorial and polar components of the neutrino velocity respectively.

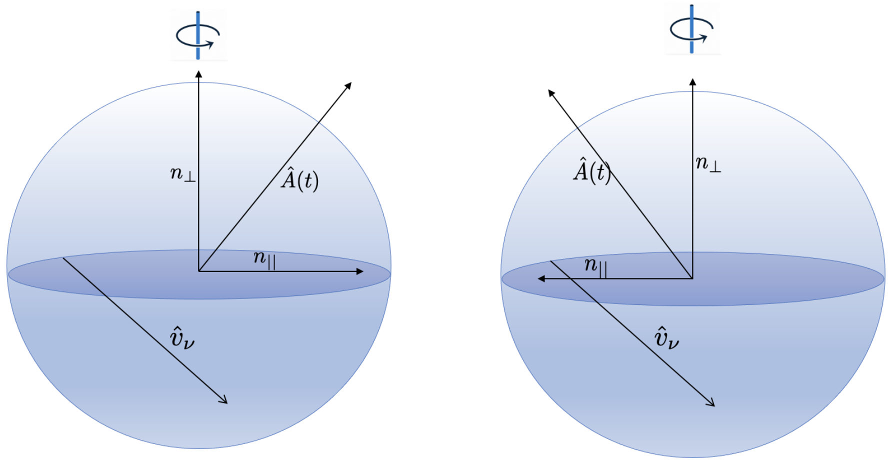

Figure 4.2: The equatorial component of the vector polarization $n_{||}$ rotates in the lab frame due to the Earth's rotation whereas the polar component $n_\perp$ remains unchanged. For experiments like DUNE, the neutrino velocity has a fixed direction. Hence the angle between the vector polarization and the neutrino velocity oscillates with the frequency of a day.

We can similarly write the dark matter polarization unit vector in the lab frame as

$$\hat{A}(t) = (n_{||}\cos(\omega_d t), \;\; n_\perp), \tag{4.20}$$

where $n_{||}$ and $n_\perp$ are the equatorial and polar components of the vector polarization and ω_d is the daily frequency. We can write the vector DM potential, Eq. 4.8,

$$H_{\text{int}} = \frac{\sqrt{2\rho}}{m_A}\cos(m_A t + \phi)\cos\alpha(t)\begin{pmatrix} g & 0 & 0 \\ 0 & g' - g & 0 \\ 0 & 0 & -g' \end{pmatrix} \tag{4.21}$$

$$\cos\alpha(t) = \hat{A}(t)\cdot\hat{v}_\nu. \tag{4.22}$$

In an experiment with high statistics, we can make out the daily modulation of the signal. On the other hand, without any temporal information about the data or in case of small statistics , we can observe the time averaged effect of the daily modulation.

The daily average removes the first order correction $\langle P^{(1)} \rangle = 0$ and only the higher order effects remain observable. In the case of sufficiently light DM, $m_A \ll \omega_d$, averaging over a day does not average over a full oscillation of DM. In that case, the oscillation of the DM effect is observable even after taking the daily average. On the other hand, if one averages over the lifetime of the experiment, as is typically done, the dark matter oscillations are also averaged over.

After averaging over the lifetime of the experiment, the oscillation probability is given by

$$\langle P_{\nu_e \to \nu_\mu} \rangle = P^{(0)} + \left(\frac{1}{2} n_{||}^2 v_{||}^2 + n_\perp^2 v_\perp^2 \right) \langle P^{(2)} \rangle + \cdots \tag{4.23}$$

where $P^{(0)}, P^{(2)}$ is same as in Eq. 4.13. Here we have assumed that the DM is light enough so that the coherence time of the DM is longer than the experiment lifetime, hence the vector polarization $(n_{||}, n_\perp)$ can be treated as constant. We see that the effect of the daily average is a correction of the DM effect which is dependent on the DM polarization and the beam direction. Given a global network of neutrino beam experiments, we can not only observe but also map out the DM polarization in the solar neighborhood.

If the DM coherence time is longer than a day but much smaller than the lifetime of the experiment, we have to average over all possible DM polarizations.

$$\langle P_{\nu_e \to \nu_\mu} \rangle = P^{(0)} + \frac{1}{2} \left(\frac{1}{2} v_{||}^2 + v_\perp^2 \right) \langle P^{(2)} \rangle + \cdots \tag{4.24}$$

For a neutrino beam experiment like DUNE, we can compare Eq. 4.14 to Eq. 4.24 to

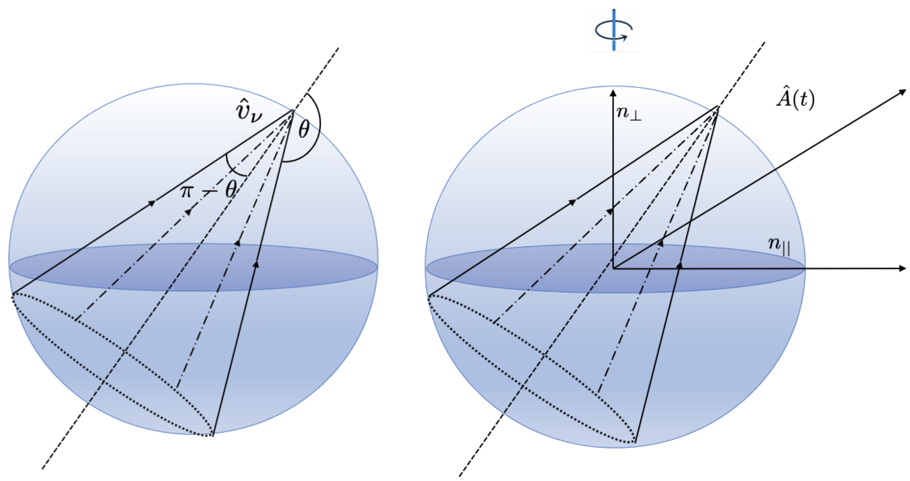

Figure 4.3: Schematic diagram showing the two different averages over atmospheric neutrino velocity. For atmospheric neutrinos, the neutrino velocity doesn't have a fixed direction. On the left, we have shown the averaging of the neutrino velocity over the same zenith angle θ (it is conventional to assign $\theta = 0$ to down-going neutrinos). Paths with the same zenith angle have equal lengths which form a cone. This is standard for atmospheric neutrino experiments, as discussed in 4.3.1. We also have to average over the daily modulation, which we have shown on the right.

perceive the effect of the Earth's rotation. The difference depends upon the latitude and longitude of both the points of neutrino production and detection. On the other hand, for atmospheric neutrino experiments, shown in Fig. 4.3, there are a whole host of neutrino velocities distributed on a two sphere. It is customary to bin events by zenith angle θ, as shown in Fig. 4.3. Then each bin corresponds to atmospheric neutrinos with the same path length from production to detection. For an experiment located near the Earth's rotation axis, like IceCube [194, 195], this corresponds to averaging over $v_{||}$. However, for an experiment located elsewhere, like Super-Kamiokande [4, 5, 190], the constant zenith angle averaging will correspond to different averages over the neutrino velocity depending on the particular location. To get an estimate of the impact of the velocity average on the vector DM effect, we can look at average over both neutrino velocity and

DM polarization,

$$\langle P_{\nu_e \to \nu_\mu} \rangle \;=\; P^{(0)} + \frac{3}{8}\langle P^{(2)} \rangle + \cdots \tag{4.25}$$

The effect of daily average and the angular average is clear once we compare Eq. 4.14 to Eq. 4.25.

On the other hand, since the revolution of the Earth around the sun only modulates the velocity of the vector field, neutrino experiments are not sensitive to such effects.

4.3 Experiments

In order to get a qualitative understanding of which experiments are the most efficient at detecting Vector DM, we can compare the relative strengths of various terms in the Hamiltonian

$$H_{\text{vac}} \sim \frac{\Delta m^2}{E_\nu}, \qquad H_{\text{int}} \sim g\frac{\sqrt{2\rho}}{m_A}. \tag{4.26}$$

Here, we can make a simplifying assumption that a given experiment is sensitive to DM when both terms in the Hamiltonian are comparable

$$H_{int} \lesssim H_{vac} \qquad \to \qquad g \lesssim \frac{m_A}{E_\nu}\frac{\Delta m^2}{\sqrt{2\rho}} \sim 10^{-30}\left(\frac{m_A}{10^{-20}\ \text{eV}}\right)\left(\frac{10\ \text{GeV}}{E_\nu}\right). \tag{4.27}$$

As the vacuum term gets smaller with higher neutrino energies, we can see that experiments that operate at higher energies have greater discovery potential.

Naively, one could use the most energetic neutrinos to set the most stringent constraints. However, as the energy of neutrinos increases so does the oscillation length. Since the longest baseline we can probe is of the size of the Earth, this limits the most efficient energies to $E \sim 10$ GeV. Experiments that operate or will operate at these energies are Super-Kamiokande [4, 5, 190], IceCube [194, 195], DUNE [6, 192, 193] and Hyper-Kamiokande [196]. We can divide these experiments into two categories: atmospheric neutrino experiments (Super-Kamiokande, IceCube, DUNE and Hyper-Kamiokande) and beam experiments (DUNE). Below, we consider one experiment of each type, with Super-Kamiokande as an example of an atmospheric neutrino experiment and DUNE as an example of a neutrino beam experiment.

4.3.1 Super-Kamiokande

Super-Kamiokande is a water-Cherenkov detector that is designed to measure neutrinos of astrophysical, atmospheric and accelerator origins. In this work, we focus on atmospheric neutrinos detected by Super-Kamiokande. In this type of experiment we can reconstruct neutrino direction and their energy. As neutrinos are produced in the atmosphere, the distance they travel before reaching the detector is related to the zenith angle θ shown in Fig. 4.3. When $\cos\theta = 1$, the distance covered by neutrinos is of order $O(10\text{ km})$, while $\cos\theta = -1$ corresponds to distances of order $O(10^4\text{ km})$. In our analysis, we focus on neutrinos coming from underground ($\cos\theta < 0$) as the longer effective baseline allows the effect of DM to accumulate, leading to stronger sensitivity.

Super-Kamiokande divides neutrino events into three main categories, fully contained (FC), partially contained (PC) and up-going muons (Up-μ). Both FC and PC categories include neutrinos that convert into electrons/muons inside the detector. However, leptons produced during FC neutrino events deposit all energy inside the inner detector whereas leptons produced during PC events stop at the outer detector or deposit only a fraction of their energy before leaving the detector. The final type of event, Up-μ, includes muons that were produced outside the detector but stopped inside it or passed through it leaving a trace.

As we are interested in the neutrinos that have energies of order 10 GeV and whose angular direction can be resolved, there are two event sub-categories that meet this criterion, PC through-going and Up-μ stopping. Both samples have similar energy distributions that peak around 10 GeV [4]. The first sub-category includes mostly muons and antimuons that were produced inside the detector but managed to escape it. These events are binned over zenith angle $\cos\theta \in [-1, 1]$ with a bin size of $\Delta\cos\theta = 0.2$. The second sub-category contains the muons and antimuons that were produced outside the detector but stopped inside. Here, events are binned over a shorter range of zenith angle $\cos\theta \in [-1, 0]$, with a smaller bin size of $\Delta\cos\theta = 0.1$.

In the analysis, we use two data sets for each sub-category. The first one contains the number of observed events [5] as a function of the zenith angle $\cos\theta$, as shown in the Fig. 4.3. The second data set has the ratio of observed neutrino events to the expectation in the case of standard neutrino oscillations as a function of zenith angle $\cos\theta$ [4]. For the Up-μ stopping sub-category, both data sets are binned over $\cos\theta \in [-1, 0]$ into 10 bins of size $\Delta\cos\theta = 0.1$. For PC through-going sub-category we use the first 5 bins which correspond to $\cos\theta \in [-1, 0]$ as they are the most sensitive to the effect of VDM. We use these data sets as an experimental input to the χ^2 test

$$\chi^2(N_i, O_i) = 2\sum_{i=1}^{bins}\left(N_i - O_i + O_i \ln\frac{O_i}{N_i}\right) = 2\sum_{i=1}^{bins} O_i\left(\left(\frac{N_i}{N_i^0}x_i^{-1}\right) - 1 + \ln x_i \frac{N_i^0}{N_i}\right) \quad (4.28)$$

where O_i is the number of observed events, N_i is the number of expected events, N_i^0 is the number of expected events assuming standard neutrino oscillations [4] and $x_i = O_i/N_i^0$. The subscript i refers to the bin.

The input from our model is contained in the ratio $\frac{N_i}{N_i^0}$. In our work, we make a simplifying assumption that the energy of neutrinos is 10 GeV. We also assume that the detector response is identical for all neutrinos collected in a single bin. As a result, we can write the ratio $\frac{N_i}{N_i^0}$ as

$$\frac{N_i}{N_i^0} = \frac{\sum\limits_{a=e,\mu}\langle P_{a\to\mu}\rangle_i \Phi_{a,i} + \sum\limits_{a=\bar{e},\bar{\mu}}\langle P_{a\to\bar{\mu}}\rangle_i \Phi_{a,i}}{\sum\limits_{a=e,\mu}\langle P^0_{a\to\mu}\rangle_i \Phi_{a,i} + \sum\limits_{a=\bar{e},\bar{\mu}}\langle P^0_{a\to\bar{\mu}}\rangle_i \Phi_{a,i}} \quad (4.29)$$

where $\Phi_{a,i}$ is the atmospheric neutrino flux from [197]. $\langle P_{a\to\mu}\rangle_i$ is the probability averaged over bin i, where we average over azimuthal and zenith angles as well as DM oscillation and rotation of the Earth. The probability is calculated in the low mass limit where we assume that the DM phase is approximately constant as the neutrino passes through the Earth. Following [4, 5] we include the effect of changing electron density by employing the PREM model [198]. Taking the same 3-flavor neutrino oscillation parameters as in [4] we get the following bounds at the 2σ level

$$g < 2\cdot 10^{-31}\left(\frac{m_A}{10^{-20}\text{ eV}}\right) \qquad g' < 1\cdot 10^{-31}\left(\frac{m_A}{10^{-20}\text{ eV}}\right). \quad (4.30)$$

These bounds are only valid in the low mass limit. The treatment of the high mass limit is explained in Sec. 4.3.3. The projected bounds are shown in Fig. 4.4 and 4.5.

In order to validate the above result we performed cross-checks by reproducing the results of Ref. [4]. Ref. [4] examined the bounds coming from Lorentz symmetry violation in the form of chemical potentials and thus resembles our signal up to the time and direction dependence. The reproduced results differed by up to a factor of two, which we can use as an estimate of the accuracy of our method.

4.3.2 DUNE

As mentioned before, sensitivity is best for an experiment with a long baseline and high energy. As an example of a neutrino beam experiment with these properties, we consider the Deep Underground Neutrino Experiment (DUNE). DUNE produces a beam of primarily muon neutrinos at Fermilab at energies between 0.5 and 10 GeV. These neutrinos are then sent along a 1285 km path to a detector in Lead, SD. There, they measure the number of muon neutrinos that have disappeared (N^{dis}) and the number of electron neutrinos that have appeared (N^{app}). Figures 10 and 11 in Ref. [193] present a prediction for $N^{dis,app}$ using standard neutrino oscillations with the number of disappearance/appearance events. This data is presented in energy bins of width 0.25 GeV from $0.5 - 8$ GeV.

We can use these measurements to place bounds on our vector dark matter interaction. An exact treatment would involve a full simulation of the detector using the GLoBES framework [199, 200] as was done in Ref. [193] for standard oscillations and for a variety of BSM extensions to standard oscillations in Ref. [6]. However, we take a simplified approach by assuming that the detector response is the same for all neutrinos in a single energy bin. In this approximation, we can write $N_i^{app}(N_i^{dis})$, the number of electron-neutrino appearance events (muon-neutrino disappearance events) in the i^{th} energy bin, as

$$N_i^{dis} = N_i^{dis,0}\frac{1-\langle P_{\mu\to\mu}\rangle_i}{1-\left\langle P^0_{\mu\to\mu}\right\rangle_i} \qquad N_i^{app} = N_i^{app,0}\frac{\langle P_{\mu\to e}\rangle_i}{\left\langle P^0_{\mu\to e}\right\rangle_i} \tag{4.31}$$

Here the superscript 0 represents quantities taken without dark matter interactions and $\langle\rangle_i$ represents averaging over the i^{th} energy bin. We numerically compute the oscillation probabilities using three flavor oscillations in the low mass limit. We vary the dark matter coupling, g or g', while three-flavor oscillation parameters are kept fixed at the central values of the global fit [201] used by the DUNE collaboration in their simulated data for appearance/disappearance events [6]. Placing projected bounds from DUNE is complicated by the fact that we only have predicted data for N_i^{app} and N_i^{dis} and not any actual data. If we did have an observed number of events in each bin O_i we could simply compute the χ^2 for our theory using Eq 4.28. If we wanted to compare our vector dark matter theory to standard oscillations, we would look at the difference in χ^2 between the two theories

$$\Delta\chi^2(N_i, N_i^0, O_i) = \chi^2(N_i, O_i) - \chi^2(N_i^0, O_i) = 2\sum_i N_i - N_i^0 + O_i \ln\left(\frac{N_i^0}{N_i}\right) \tag{4.32}$$

Here the sum over bins sums over the bins for both muon-neutrino disappearance and electron-neutrino appearance to give the total χ^2. However, since we do not have any real data to compare to, we imagine drawing O_i from the distribution for appearance/disappearance events for standard oscillations given by N_i^0. Since $\Delta\chi^2$ is linear in O_i this amounts to replacing O_i with N_i^0 in Eq

4.32.

$$\left\langle \Delta\chi^2(N_i, N_i^0, O_i) \right\rangle_{O_i} = \chi^2(N_i, N_i^0) \tag{4.33}$$

If $\Delta\chi^2 > 4$ we would then be able to distinguish standard oscillations from standard oscillations with our vector dark matter interaction at the 2σ level. We can then place a predicted bound on our coupling, assuming that DUNE will not find disagreement with standard oscillations, by demanding

$$\Delta\chi^2(g) < 4 \tag{4.34}$$

where g is the coupling of interest. As a cross-check, we were able to use this method to reproduce the bounds on the flavor-diagonal piece of the non-standard neutrino interactions from Ref. [6] to within 20%. These flavor-diagonal non-standard neutrino interactions are very similar to our dark matter interaction. In fact, they are equivalent if we send $\cos(m_A t + \phi)\cos(\alpha) \to 1$ in Eq. 4.8. It is likely that our bounds have similar error bars.

As seen from Eq. 4.8, the strength of our interaction depends not only on the strength of the coupling g and g' but also on the relative direction of the neutrino velocity to the dark matter polarization and the phase of the dark matter. All of these quantities vary on different timescales. The phase of the dark matter, $m_A t + \phi$ in Eq. 4.8, changes on the time scale m_A^{-1}. The direction of the neutrinos' velocity changes on a daily time scale due to the Earth's rotation. Finally, the direction and amplitude of the dark matter background and changes on the scale of the coherence time of the dark matter background which scales with $t_{coh} \sim 10^6\, m_A^{-1}$. For time scales that are shorter than the total data collection time of DUNE, around 3-7 years, we should average the probabilities $P_{\mu\to\mu}$ and $P_{\mu\to e}$ over these time scales before placing the bound from Eq. 4.34. This is true for all three of our relevant time scales except for the coherence time for masses $m_A < 3 \cdot 10^{-18}$ eV. For masses below this limit, the dark photon field is coherent during the 3-7 year duration of the experiment so we must first compute bounds for each direction of the dark photon polarization. Then, in order to capture the fact we do not know in which direction the dark matter points, we should average these bounds over all dark photon polarizations. However, we find that whether or not we average over dark matter polarizations before or after computing the bounds leads to an $\mathcal{O}(10\%)$ change in the resulting average bound in the end. We, therefore, ignore this subtlety and average over all time scales before computing the bound. We find the bounds on $g(g')$ to be

$$g < 10^{-30} \left(\frac{m_A}{10^{-20}\text{ eV}}\right) \qquad g' < 7 \cdot 10^{-31} \left(\frac{m_A}{10^{-20}\text{ eV}}\right). \tag{4.35}$$

These bounds are shown plotted below in Fig. 4.4 and 4.5.

As mentioned before, we are using DUNE as an example of the sensitivity of a neutrino beam experiment. DUNE expects to detect oscillations from the background atmospheric neutrinos as described in Ref. [192] where they argue DUNE will have a sensitivity similar to Hyper-Kamiokande. If one were to use this aspect of DUNE, then the bounds in Eq. 4.35 and Eq. 4.30 would be improved upon significantly.

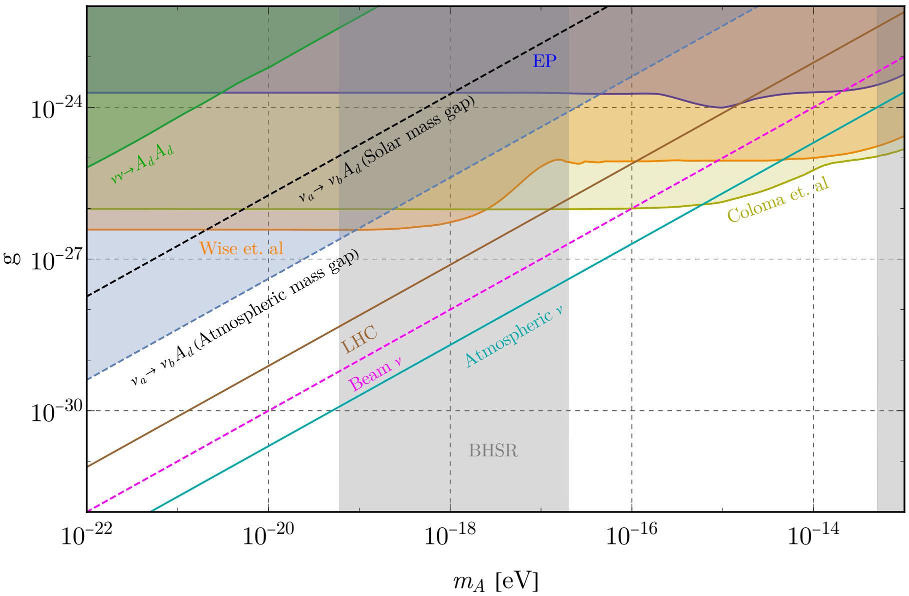

Figure 4.4: Constraints on the $L_e - L_\mu$ coupling from atmospheric and beam neutrino experiments. The curves show upper limits on the coupling g. The atmospheric neutrino bound is represented by the cyan line, which is derived using Super-Kamiokande data [4, 5]. The dashed magenta line gives the projected sensitivity of neutrino beam experiments, which is obtained assuming DUNE operating in the beam mode [6]. Our constraints are several orders of magnitude stronger than the cosmological ν-decay bound (light blue and black dashed lines) [7] and five orders of magnitude stronger than other terrestrial bounds at the lower end of the allowed mass range. It is expected that time dependent analysis will improve these bounds. Other constraints are from BH superradiance (gray band) [8], neutrino oscillations modified by a fifth force (orange and yellow lines) [9, 10], ΔN_{eff} through $\nu\nu \to A_d A_d$ (green line) [11, 12], EP violating forces (dark blue line) [9, 13] and a model dependent bound coming from a mono-lepton plus missing energy search at LHC (brown line) [14].

4.3.3 Results

We numerically find the DUNE and Super-Kamiokande bound for a DM mass in the small mass limit using the methods described before. To obtain a bound for an arbitrary mass, we rescale the bound using the full second-order correction to the oscillation probability, $\langle P^{(2)} \rangle$, given in Eq. 4.15. In Eq. 4.15, L is the neutrino baseline, $\Delta_\nu = \frac{\Delta m_{13}^2}{4E_\nu}$, A_0 is the field strength $A_0 = \frac{\sqrt{2\rho_{DM}}}{m_A}$, and g is the coupling we are interested in (either g or g'). For each of the experiments, we insert different values of L and E_ν. For DUNE [193], we use the baseline

$L \approx 1300$ km and $E_\nu = 2$ GeV, roughly the energy at which detection events peak. For Super-Kamiokande we use $E_\nu = 10$ GeV. The length for Super-Kamiokande is complicated since, for atmospheric neutrinos, L varies depending on the zenith angle θ. In principle, we should use an effective length, weighted over the bins. For simplicity, we use $L \approx 12000$ km, roughly the diameter of the Earth. A different choice of L does not alter our constraint in the low mass regime or its qualitative feature over the whole of the parameter space.

In order to use Eq. 4.15 to rescale our bounds, perturbation theory in g (g') must be valid. Using Eq. 4.18 with $E_\nu = 10$ GeV for Super-Kamiokande and $E_\nu = 2$ GeV for DUNE to obtain the perturbative limit for both experiments and comparing these limits to the bounds placed in Eq. 4.30 and 4.35, we find that our bounds are soundly in the perturbative limit.

As an additional cross-check of this extrapolation, we solved for the transition probabilities numerically for a few values of m_A in the high mass regime for both DUNE and Super-Kamiokande. While doing this for all points in our parameters space is too computationally expensive, we find good agreement between our perturbation extrapolation to high masses and the exact numerical results.

4.4 Conclusions

In this work, we studied the effects of ultra-light vector dark matter consisting of a dark photon. We consider our dark photon to be the gauge boson of gauged lepton flavor number with different couplings for each flavor. We showed the effect of such a coupling in the context of neutrino oscillations is to give each neutrino flavor an effective chemical potential proportional to the background dark matter field and the coupling. Because the couplings are flavor asymmetric,

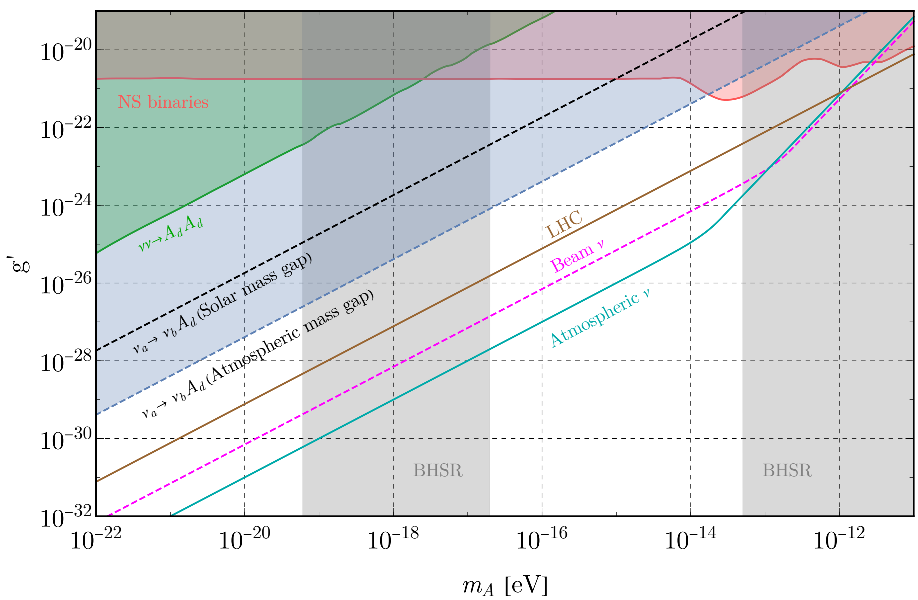

Figure 4.5: Constraints on the $L_\mu - L_\tau$ coupling from atmospheric and beam neutrino experiments. The curves show upper limits on the coupling g'. The atmospheric neutrino bound is derived using Super-Kamiokande data [4, 5]. The projected sensitivity of beam neutrino experiments is obtained assuming DUNE operating in the beam mode [6]. Our constraints are several orders of magnitude stronger than the cosmological ν-decay bound (light blue and black dashed lines) [7] and eight orders of magnitude stronger than other existing constraints at the lower end of the allowed mass range. It is expected that time-dependent analysis will improve these bounds. Previous constraints are from BH superradiance (gray band) [8], $\Delta N_{\rm eff}$ through $\nu\nu \to A_d A_d$ (green line) [11, 12], NS binaries (red line) [15] and a model-dependent bound coming from a mono-lepton plus missing energy search at LHC (brown line) [14].

these chemical potentials are different for each neutrino flavor and thus will have some effect on neutrino oscillations. Because this interaction is diagonal in flavor space, we saw that the net effect of these couplings is to dampen the mixing, and thus dampen oscillations between neutrino flavor eigenstates.

Using this effect, we are able to place bounds on the flavor asymmetric couplings $g\,(U(1)_{L_e-L_\mu})$ and $g'\,(U(1)_{L_\mu-L_\tau})$ by comparing to neutrino oscillation experiments. Using Super-Kamiokande (DUNE) as an example, we found the (projected) bounds coming from an atmospheric (beam) neutrino experiment. These bounds are shown in Fig. 4.4 and Fig. 4.5. For both, we found our bounds beat previously leading bounds for low dark matter masses and give bounds comparable to leading bounds at high masses.

We also considered time-dependent effects unique to our vector dark matter background. In particular, due to the Earth's rotation, neutrinos in the earth's frame see a vector background that rotates on a daily basis. Since the coupling between neutrinos and the dark matter background is proportional to $\vec{A}_d \cdot \vec{v}_\nu$, this rotation effect would manifest as daily modulations in neutrino oscillations. In our bounds, we averaged over these daily modulations. However, one could look for these daily modulations directly. These daily modulation would be seen as a daily time dependence in the appearance/disappearance events. One would need to have the time-stamped data to see this effect. This would involve working directly with the data from neutrino oscillation experiments and so we leave it for future works. In addition to this time-dependent analysis, bounds could be made more precise with future atmospheric neutrino experiments such as Hyper-Kamiokande, DUNE and by working more directly with experiments like IceCube.

Chapter 5: Conclusion

The search for new physics must be pursued in all possible directions. In this thesis I have divided my efforts in search of UV completion as well as search for DM.

In chapter 2, we showed that Non-abelian discrete symmetries are interesting and started the study of their Nambu Goldstone bosons. Perhaps the most exciting future directions would be if it were possible to gauge various sub-groups of the accidental symmetries so that one could actually charge discrete NGBs under a gauge symmetry.

In chapter 3, we explored the evaporation of black holes in the early universe and showed how they heat up the surrounding plasma. This plasma can reach temperatures much larger than the ambient temperature and can have effects more significant than that of the black hole itself. As an example, while monopole production by black hole evaporation is negligible, monopole production by the surrounding plasma can be very significant. However, we have only listed a single scenario where the plasma surrounding the black hole has a significant effect. It would be interesting if there are other situations where this plasma is important.

In chapter 4, we studied the effects of ultra-light vector dark matter consisting of a dark photon. We consider our dark photon to be the gauge boson of gauged lepton flavor number with different couplings for each flavor. We showed the effect of such a coupling in the context of neutrino oscillations is to give each neutrino flavor an effective chemical potential proportional to the background dark matter field and the coupling. Because the couplings are flavor asymmetric, these chemical potentials are different for each neutrino flavor and thus will have some effect on neutrino oscillations.

Bibliography

[1] Martin Schmaltz and David Tucker-Smith. Little Higgs review. *Ann. Rev. Nucl. Part. Sci.*, 55:229–270, 2005.

[2] Arttu Rajantie. Introduction to Magnetic Monopoles. *Contemp. Phys.*, 53:195–211, 2012.

[3] Hajime Ishimori, Tatsuo Kobayashi, Hiroshi Ohki, Yusuke Shimizu, Hiroshi Okada, and Morimitsu Tanimoto. Non-Abelian Discrete Symmetries in Particle Physics. *Prog. Theor. Phys. Suppl.*, 183:1–163, 2010.

[4] K. Abe et al. Test of Lorentz invariance with atmospheric neutrinos. *Phys. Rev. D*, 91(5):052003, 2015.

[5] K. Abe et al. Limits on sterile neutrino mixing using atmospheric neutrinos in Super-Kamiokande. *Phys. Rev. D*, 91:052019, 2015.

[6] B. Abi et al. Prospects for beyond the Standard Model physics searches at the Deep Underground Neutrino Experiment. *Eur. Phys. J. C*, 81(4):322, 2021.

[7] Joe Zhiyu Chen, Isabel M. Oldengott, Giovanni Pierobon, and Yvonne Y. Y. Wong. Weaker yet again: mass spectrum-consistent cosmological constraints on the neutrino lifetime. *Eur. Phys. J. C*, 82(7):640, 2022.

[8] Masha Baryakhtar, Robert Lasenby, and Mae Teo. Black Hole Superradiance Signatures of Ultralight Vectors. *Phys. Rev. D*, 96(3):035019, 2017.

[9] Mark B. Wise and Yue Zhang. Lepton Flavorful Fifth Force and Depth-dependent Neutrino Matter Interactions. *JHEP*, 06:053, 2018.

[10] Pilar Coloma, M. C. Gonzalez-Garcia, and Michele Maltoni. Neutrino oscillation constraints on U(1)' models: from non-standard interactions to long-range forces. *JHEP*, 01:114, 2021. [Erratum: JHEP 11, 115 (2022)].

[11] Jeff A. Dror. Discovering leptonic forces using nonconserved currents. *Phys. Rev. D*, 101(9):095013, 2020.

[12] Guo-yuan Huang, Tommy Ohlsson, and Shun Zhou. Observational Constraints on Secret Neutrino Interactions from Big Bang Nucleosynthesis. *Phys. Rev. D*, 97(7):075009, 2018.

[13] Stephan Schlamminger, K. Y. Choi, T. A. Wagner, J. H. Gundlach, and E. G. Adelberger. Test of the equivalence principle using a rotating torsion balance. *Phys. Rev. Lett.*, 100:041101, 2008.

[14] Majid Ekhterachian, Anson Hook, Soubhik Kumar, and Yuhsin Tsai. Bounds on gauge bosons coupled to nonconserved currents. *Phys. Rev. D*, 104(3):035034, 2021.

[15] Jeff A. Dror, Ranjan Laha, and Toby Opferkuch. Probing muonic forces with neutron star binaries. *Phys. Rev. D*, 102(2):023005, 2020.

[16] Tatsumi Aoyama, Masashi Hayakawa, Toichiro Kinoshita, and Makiko Nio. Tenth-Order QED Contribution to the Electron g-2 and an Improved Value of the Fine Structure Constant. *Phys. Rev. Lett.*, 109:111807, 2012.

[17] T. Aoyama, M. Hayakawa, T. Kinoshita, and M. Nio. Automated calculation scheme for alpha**n contributions of QED to lepton g-2: Generating renormalized amplitudes for diagrams without lepton loops. *Nucl. Phys. B*, 740:138–180, 2006.

[18] T. Kinoshita and M. Nio. The Tenth-order QED contribution to the lepton g-2: Evaluation of dominant alpha**5 terms of muon g-2. *Phys. Rev. D*, 73:053007, 2006.

[19] Lisa Randall and Raman Sundrum. A Large mass hierarchy from a small extra dimension. *Phys. Rev. Lett.*, 83:3370–3373, 1999.

[20] Lisa Randall and Raman Sundrum. An Alternative to compactification. *Phys. Rev. Lett.*, 83:4690–4693, 1999.

[21] Nima Arkani-Hamed, Savas Dimopoulos, and G. R. Dvali. The Hierarchy problem and new dimensions at a millimeter. *Phys. Lett. B*, 429:263–272, 1998.

[22] Ignatios Antoniadis, Nima Arkani-Hamed, Savas Dimopoulos, and G. R. Dvali. New dimensions at a millimeter to a Fermi and superstrings at a TeV. *Phys. Lett. B*, 436:257–263, 1998.

[23] Nima Arkani-Hamed, Savas Dimopoulos, and G. R. Dvali. Phenomenology, astrophysics and cosmology of theories with submillimeter dimensions and TeV scale quantum gravity. *Phys. Rev. D*, 59:086004, 1999.

[24] N. Arkani-Hamed, A. G. Cohen, E. Katz, A. E. Nelson, T. Gregoire, and Jay G. Wacker. The Minimal moose for a little Higgs. *JHEP*, 08:021, 2002.

[25] Nima Arkani-Hamed, Andrew G Cohen, Emanuel Katz, and Ann E Nelson. The littlest higgs. *Journal of High Energy Physics*, 2002(07):034–034, jul 2002.

[26] Z. Chacko, Hock-Seng Goh, and Roni Harnik. The Twin Higgs: Natural electroweak breaking from mirror symmetry. *Phys. Rev. Lett.*, 96:231802, 2006.

[27] Arttu Rajantie. Magnetic Monopoles in Field Theory and Cosmology. *Phil. Trans. Roy. Soc. Lond. A*, 370:5705–5717, 2012.

[28] Gerard 't Hooft. Magnetic Monopoles in Unified Gauge Theories. *Nucl. Phys. B*, 79:276–284, 1974.

[29] Alexander M. Polyakov. Particle Spectrum in Quantum Field Theory. *JETP Lett.*, 20:194–195, 1974.

[30] John Preskill. MAGNETIC MONOPOLES. *Ann. Rev. Nucl. Part. Sci.*, 34:461–530, 1984.

[31] George Johnson and John March-Russell. Hawking Radiation of Extended Objects. *JHEP*, 04:205, 2020.

[32] Simeon Bird, Matteo Viel, and Martin G. Haehnelt. Massive neutrinos and the non-linear matter power spectrum. *Monthly Notices of the Royal Astronomical Society*, 420(3):2551–2561, jan 2012.

[33] Shankar Agarwal and Hume A. Feldman. The effect of massive neutrinos on the matter power spectrum. *Monthly Notices of the Royal Astronomical Society*, pages no–no, oct 2010.

[34] L. Wolfenstein. Neutrino Oscillations in Matter. *Phys. Rev. D*, 17:2369–2374, 1978.

[35] S. P. Mikheyev and A. Yu. Smirnov. Resonance Amplification of Oscillations in Matter and Spectroscopy of Solar Neutrinos. *Sov. J. Nucl. Phys.*, 42:913–917, 1985.

[36] Sanjib Kumar Agarwalla and Pilar Hernandez. Probing the Neutrino Mass Hierarchy with Super-Kamiokande. *JHEP*, 10:086, 2012.

[37] Anushree Ghosh, Tarak Thakore, and Sandhya Choubey. Determining the Neutrino Mass Hierarchy with INO, T2K, NOvA and Reactor Experiments. *JHEP*, 04:009, 2013.

[38] Olga Mena, Hiroshi Nunokawa, and Stephen J. Parke. NOvA and T2K: The Race for the neutrino mass hierarchy. *Phys. Rev. D*, 75:033002, 2007.

[39] M. Bass et al. Baseline Optimization for the Measurement of CP Violation, Mass Hierarchy, and θ_{23} Octant in a Long-Baseline Neutrino Oscillation Experiment. *Phys. Rev. D*, 91(5):052015, 2015.

[40] *Neutrino Non-Standard Interactions: A Status Report*, volume 2, 2019.

[41] Y. Farzan and M. Tortola. Neutrino oscillations and Non-Standard Interactions. *Front. in Phys.*, 6:10, 2018.

[42] V. Alan Kostelecky and Matthew Mewes. Lorentz violation and short-baseline neutrino experiments. *Phys. Rev. D*, 70:076002, 2004.

[43] Teppei Katori. Tests of Lorentz and CPT violation with MiniBooNE neutrino oscillation excesses. *Mod. Phys. Lett. A*, 27:1230024, 2012.

[44] Abhish Dev, Pedro A. N. Machado, and Pablo Martínez-Miravé. Signatures of ultralight dark matter in neutrino oscillation experiments. *JHEP*, 01:094, 2021.

[45] Matías M. Reynoso and Oscar A. Sampayo. Propagation of high-energy neutrinos in a background of ultralight scalar dark matter. *Astropart. Phys.*, 82:10–20, 2016.

[46] Asher Berlin. Neutrino Oscillations as a Probe of Light Scalar Dark Matter. *Phys. Rev. Lett.*, 117(23):231801, 2016.

[47] Gordan Krnjaic, Pedro A. N. Machado, and Lina Necib. Distorted neutrino oscillations from time varying cosmic fields. *Phys. Rev. D*, 97(7):075017, 2018.

[48] Vedran Brdar, Joachim Kopp, Jia Liu, Pascal Prass, and Xiao-Ping Wang. Fuzzy dark matter and nonstandard neutrino interactions. *Phys. Rev. D*, 97(4):043001, 2018.

[49] Marta Losada, Yosef Nir, Gilad Perez, and Yogev Shpilman. Probing scalar dark matter oscillations with neutrino oscillations. *JHEP*, 04:030, 2022.

[50] Anson Hook. Solving the Hierarchy Problem Discretely. *Phys. Rev. Lett.*, 120(26):261802, 2018.

[51] Yoichiro Nambu and G. Jona-Lasinio. Dynamical Model of Elementary Particles Based on an Analogy with Superconductivity. 1. *Phys. Rev.*, 122:345–358, 1961.

[52] J. Goldstone. Field Theories with Superconductor Solutions. *Nuovo Cim.*, 19:154–164, 1961.

[53] Jeffrey Goldstone, Abdus Salam, and Steven Weinberg. Broken Symmetries. *Phys. Rev.*, 127:965–970, 1962.

[54] Stephen L. Adler. Consistency conditions on the strong interactions implied by a partially conserved axial vector current. *Phys. Rev.*, 137:B1022–B1033, 1965.

[55] Holger Bech Nielsen and S. Chadha. On How to Count Goldstone Bosons. *Nucl. Phys. B*, 105:445–453, 1976.

[56] Tomas Brauner. Spontaneous Symmetry Breaking and Nambu-Goldstone Bosons in Quantum Many-Body Systems. *Symmetry*, 2:609–657, 2010.

[57] Haruki Watanabe and Hitoshi Murayama. Unified Description of Nambu-Goldstone Bosons without Lorentz Invariance. *Phys. Rev. Lett.*, 108:251602, 2012.

[58] Clifford Cheung, Karol Kampf, Jiri Novotny, and Jaroslav Trnka. Effective Field Theories from Soft Limits of Scattering Amplitudes. *Phys. Rev. Lett.*, 114(22):221602, 2015.

[59] Ian Low. Adler's zero and effective Lagrangians for nonlinearly realized symmetry. *Phys. Rev. D*, 91(10):105017, 2015.

[60] Clifford Cheung, Karol Kampf, Jiri Novotny, Chia-Hsien Shen, and Jaroslav Trnka. A Periodic Table of Effective Field Theories. *JHEP*, 02:020, 2017.

[61] Ian Low and Zhewei Yin. Ward Identity and Scattering Amplitudes for Nonlinear Sigma Models. *Phys. Rev. Lett.*, 120(6):061601, 2018.

[62] Ian Low and Zhewei Yin. The Infrared Structure of Nambu-Goldstone Bosons. *JHEP*, 10:078, 2018.

[63] Laurentiu Rodina. Scattering Amplitudes from Soft Theorems and Infrared Behavior. *Phys. Rev. Lett.*, 122(7):071601, 2019.

[64] Nima Arkani-Hamed, Andrew G. Cohen, and Howard Georgi. Electroweak symmetry breaking from dimensional deconstruction. *Phys. Lett. B*, 513:232–240, 2001.

[65] N. Arkani-Hamed, A.G. Cohen, E. Katz, A.E. Nelson, T. Gregoire, and Jay G. Wacker. The Minimal moose for a little Higgs. *JHEP*, 08:021, 2002.

[66] N. Arkani-Hamed, A.G. Cohen, E. Katz, and A.E. Nelson. The Littlest Higgs. *JHEP*, 07:034, 2002.

[67] Roberto Contino, Yasunori Nomura, and Alex Pomarol. Higgs as a holographic pseudoGoldstone boson. *Nucl. Phys. B*, 671:148–174, 2003.

[68] Kaustubh Agashe, Roberto Contino, and Alex Pomarol. The Minimal composite Higgs model. *Nucl. Phys. B*, 719:165–187, 2005.

[69] Guido Altarelli and Ferruccio Feruglio. Discrete Flavor Symmetries and Models of Neutrino Mixing. *Rev. Mod. Phys.*, 82:2701–2729, 2010.

[70] Ferruccio Feruglio. *Are neutrino masses modular forms?*, pages 227–266. 2019.

[71] Nathaniel Craig, Simon Knapen, and Pietro Longhi. Neutral Naturalness from Orbifold Higgs Models. *Phys. Rev. Lett.*, 114(6):061803, 2015.

[72] Maxim Perelstein, Michael E. Peskin, and Aaron Pierce. Top quarks and electroweak symmetry breaking in little Higgs models. *Phys. Rev. D*, 69:075002, 2004.

[73] Maxim Perelstein. Little Higgs models and their phenomenology. *Prog. Part. Nucl. Phys.*, 58:247–291, 2007.

[74] Sidney Coleman and Erick Weinberg. Radiative corrections as the origin of spontaneous symmetry breaking. *Phys. Rev. D*, 7:1888–1910, Mar 1973.

[75] Stephen P. Martin. Two Loop Effective Potential for a General Renormalizable Theory and Softly Broken Supersymmetry. *Phys. Rev.*, D65:116003, 2002.

[76] Alexander Merle and Roman Zwicky. Explicit and spontaneous breaking of su(3) into its finite subgroups. *Journal of High Energy Physics*, 2012(2), Feb 2012.

[77] David Hilbert. Ueber die theorie der algebraischen formen. *Mathematische Annalen*, 36(4):473–534, Dec 1890.

[78] Emmy Noether. Der endlichkeitssatz der invarianten endlicher gruppen. *Mathematische Annalen*, 77(1):89–92, Mar 1915.

[79] Larry Smith. Polynomial invariants of finite groups. a survey of recent developments. *Bulletin of The American Mathematical Society - BULL AMER MATH SOC*, 34:211–251, 07 1997.

[80] Th. Molien. Ueber die Invarianten der linearen Substitutionsgruppen. *Berl. Ber.*, 1897:1152–1156, 1897.

[81] H. S. M. Coxeter. The product of the generators of a finite group generated by reflections. *Duke Math. J.*, 18(4):765–782, 12 1951.

[82] G. C. Shephard and J. A. Todd. Finite unitary reflection groups. *Canadian Journal of Mathematics*, 6:274–304, 1954.

[83] A. Cayley Esq. Vii. on the theory of groups, as depending on the symbolic equation n =1. *The London, Edinburgh, and Dublin Philosophical Magazine and Journal of Science*, 7(42):40–47, 1854.

[84] William Burnside. *Theory of groups of finite order*. The University press, Cambridge, 1911. xxiv, 512 p., [1] col. plate.

[85] B. P. Abbott et al. Observation of Gravitational Waves from a Binary Black Hole Merger. *Phys. Rev. Lett.*, 116(6):061102, 2016.

[86] Kazunori Akiyama et al. First M87 Event Horizon Telescope Results. I. The Shadow of the Supermassive Black Hole. *Astrophys. J. Lett.*, 875:L1, 2019.

[87] Andrei D. Linde. Hybrid inflation. *Phys. Rev. D*, 49:748–754, 1994.

[88] Juan Garcia-Bellido, Andrei D. Linde, and David Wands. Density perturbations and black hole formation in hybrid inflation. *Phys. Rev. D*, 54:6040–6058, 1996.

[89] Juan Garcia-Bellido and Andrei D. Linde. Preheating in hybrid inflation. *Phys. Rev. D*, 57:6075–6088, 1998.

[90] David H. Lyth. Primordial black hole formation and hybrid inflation, 2011.

[91] Edgar Bugaev and Peter Klimai. Formation of primordial black holes from non-Gaussian perturbations produced in a waterfall transition. *Phys. Rev. D*, 85:103504, 2012.

[92] Sébastien Clesse and Juan García-Bellido. Massive Primordial Black Holes from Hybrid Inflation as Dark Matter and the seeds of Galaxies. *Phys. Rev. D*, 92(2):023524, 2015.

[93] Masahiro Kawasaki and Yuichiro Tada. Can massive primordial black holes be produced in mild waterfall hybrid inflation? *JCAP*, 08:041, 2016.

[94] Masahiro Kawasaki, Alexander Kusenko, Yuichiro Tada, and Tsutomu T. Yanagida. Primordial black holes as dark matter in supergravity inflation models. *Phys. Rev. D*, 94(8):083523, 2016.

[95] Matt Crawford and David N. Schramm. Spontaneous Generation of Density Perturbations in the Early Universe. *Nature*, 298:538–540, 1982.

[96] S. W. Hawking, I. G. Moss, and J. M. Stewart. Bubble collisions in the very early universe. *Phys. Rev. D*, 26:2681–2693, Nov 1982.

[97] Ben Freivogel, Gary T. Horowitz, and Stephen Shenker. Colliding with a crunching bubble. *JHEP*, 05:090, 2007.

[98] Ian G. Moss. Black hole formation from colliding bubbles. 6 1994.

[99] Matthew C. Johnson, Hiranya V. Peiris, and Luis Lehner. Determining the outcome of cosmic bubble collisions in full General Relativity. *Phys. Rev. D*, 85:083516, 2012.

[100] K. Jedamzik and Jens C. Niemeyer. Primordial black hole formation during first order phase transitions. *Phys. Rev. D*, 59:124014, 1999.

[101] Michael J. Baker, Moritz Breitbach, Joachim Kopp, and Lukas Mittnacht. Primordial Black Holes from First-Order Cosmological Phase Transitions. 5 2021.

[102] Marek Lewicki and Ville Vaskonen. On bubble collisions in strongly supercooled phase transitions. *Phys. Dark Univ.*, 30:100672, 2020.

[103] Christian Gross, Giacomo Landini, Alessandro Strumia, and Daniele Teresi. Dark Matter as dark dwarfs and other macroscopic objects: multiverse relics? *JHEP*, 09:033, 2021.

[104] Jing Liu, Ligong Bian, Rong-Gen Cai, Zong-Kuan Guo, and Shao-Jiang Wang. Primordial black hole production during first-order phase transitions. 6 2021.

[105] S. W. Hawking. Black Holes From Cosmic Strings. *Phys. Lett. B*, 231:237–239, 1989.

[106] Alexander Polnarev and Robert Zembowicz. Formation of Primordial Black Holes by Cosmic Strings. *Phys. Rev. D*, 43:1106–1109, 1991.

[107] Stephen Hawking. Gravitationally collapsed objects of very low mass. *Mon. Not. Roy. Astron. Soc.*, 152:75, 1971.

[108] George F. Chapline. Cosmological effects of primordial black holes. *Nature*, 253(5489):251–252, 1975.

[109] Bernard Carr, Florian Kuhnel, and Marit Sandstad. Primordial Black Holes as Dark Matter. *Phys. Rev. D*, 94(8):083504, 2016.

[110] Bernard Carr and Florian Kuhnel. Primordial Black Holes as Dark Matter: Recent Developments. *Ann. Rev. Nucl. Part. Sci.*, 70:355–394, 2020.

[111] Anne M. Green and Bradley J. Kavanagh. Primordial Black Holes as a dark matter candidate. *J. Phys. G*, 48(4):4, 2021.

[112] Pablo Villanueva-Domingo, Olga Mena, and Sergio Palomares-Ruiz. A brief review on primordial black holes as dark matter. *Front. Astron. Space Sci.*, 8:87, 2021.

[113] Sam Young and Christian T. Byrnes. Signatures of non-gaussianity in the isocurvature modes of primordial black hole dark matter. *JCAP*, 04:034, 2015.

[114] S. W. Hawking. Black hole explosions. *Nature*, 248:30–31, 1974.

[115] S. W. Hawking. Particle Creation by Black Holes. *Commun. Math. Phys.*, 43:199–220, 1975. [Erratum: Commun.Math.Phys. 46, 206 (1976)].

[116] Don N. Page. Particle Emission Rates from a Black Hole: Massless Particles from an Uncharged, Nonrotating Hole. *Phys. Rev. D*, 13:198–206, 1976.

[117] Anne M. Green. Supersymmetry and primordial black hole abundance constraints. *Phys. Rev. D*, 60:063516, 1999.

[118] B. J. Carr, Kazunori Kohri, Yuuiti Sendouda, and Jun'ichi Yokoyama. New cosmological constraints on primordial black holes. *Phys. Rev. D*, 81:104019, 2010.

[119] Olivier Lennon, John March-Russell, Rudin Petrossian-Byrne, and Hannah Tillim. Black Hole Genesis of Dark Matter. *JCAP*, 04:009, 2018.

[120] Dan Hooper, Gordan Krnjaic, and Samuel D. McDermott. Dark Radiation and Superheavy Dark Matter from Black Hole Domination. *JHEP*, 08:001, 2019.

[121] Anson Hook. Baryogenesis from Hawking Radiation. *Phys. Rev. D*, 90(8):083535, 2014.

[122] Iason Baldes, Quentin Decant, Deanna C. Hooper, and Laura Lopez-Honorez. Non-Cold Dark Matter from Primordial Black Hole Evaporation. *JCAP*, 08:045, 2020.

[123] Celeste Keith, Dan Hooper, Nikita Blinov, and Samuel D. McDermott. Constraints on Primordial Black Holes From Big Bang Nucleosynthesis Revisited. *Phys. Rev. D*, 102(10):103512, 2020.

[124] Paul Adrien Maurice Dirac. Quantised singularities in the electromagnetic field,. *Proc. Roy. Soc. Lond. A*, 133(821):60–72, 1931.

[125] Alan H. Guth and S. H. H. Tye. Phase Transitions and Magnetic Monopole Production in the Very Early Universe. *Phys. Rev. Lett.*, 44:631, 1980. [Erratum: Phys.Rev.Lett. 44, 963 (1980)].

[126] H. Georgi and S. L. Glashow. Unity of All Elementary Particle Forces. *Phys. Rev. Lett.*, 32:438–441, 1974.

[127] H. Georgi, Helen R. Quinn, and Steven Weinberg. Hierarchy of Interactions in Unified Gauge Theories. *Phys. Rev. Lett.*, 33:451–454, 1974.

[128] T. W. B. Kibble. Topology of Cosmic Domains and Strings. *J. Phys. A*, 9:1387–1398, 1976.

[129] W. H. Zurek. Cosmological Experiments in Superfluid Helium? *Nature*, 317:505–508, 1985.

[130] Hitoshi Murayama and Jing Shu. Topological Dark Matter. *Phys. Lett. B*, 686:162–165, 2010.

[131] Gia Dvali, Lukas Eisemann, Marco Michel, and Sebastian Zell. Black hole metamorphosis and stabilization by memory burden. *Phys. Rev. D*, 102(10):103523, 2020.

[132] Michael S. Turner, Eugene N. Parker, and T. J. Bogdan. Magnetic Monopoles and the Survival of Galactic Magnetic Fields. *Phys. Rev. D*, 26:1296, 1982.

[133] Fred C. Adams, Marco Fatuzzo, Katherine Freese, Gregory Tarle, Richard Watkins, and Michael S. Turner. Extension of the Parker bound on the flux of magnetic monopoles. *Phys. Rev. Lett.*, 70:2511–2514, 1993.

[134] Yoel Rephaeli and Michael S. Turner. The Magnetic Monopole Flux and the Survival of Intracluster Magnetic Fields. *Phys. Lett. B*, 121:115–118, 1983.

[135] Edward W. Kolb, Stirling A. Colgate, and Jeffrey A. Harvey. Monopole Catalysis of Nucleon Decay in Neutron Stars. *Phys. Rev. Lett.*, 49:1373, 1982.

[136] Savas Dimopoulos, John Preskill, and Frank Wilczek. Catalyzed Nucleon Decay in Neutron Stars. *Phys. Lett. B*, 119:320, 1982.

[137] Katherine Freese, Michael S. Turner, and David N. Schramm. Monopole Catalysis of Nucleon Decay in Old Pulsars. *Phys. Rev. Lett.*, 51:1625, 1983.

[138] Bernard J. Carr. Some cosmological consequences of primordial black-hole evaporations. *Astrophys. J.*, 206:8–25, 1976.

[139] Michael S. Turner. BARYON PRODUCTION BY PRIMORDIAL BLACK HOLES. *Phys. Lett. B*, 89:155–159, 1979.

[140] John D. Barrow, Edmund J. Copeland, Edward W. Kolb, and Andrew R. Liddle. Baryogenesis in extended inflation. ii. baryogenesis via primordial black holes. *Phys. Rev. D*, 43:984–994, Feb 1991.

[141] A. S. Majumdar, P. Das Gupta, and R. P. Saxena. Baryogenesis from black hole evaporation. *Int. J. Mod. Phys. D*, 4:517–529, 1995.

[142] Niraj Upadhyay, Patrick Das Gupta, and R. P. Saxena. Baryogenesis from primordial black holes after electroweak phase transition. *Phys. Rev. D*, 60:063513, 1999.

[143] Daniel Baumann, Paul J. Steinhardt, and Neil Turok. Primordial Black Hole Baryogenesis. 3 2007.

[144] Tomohiro Fujita, Masahiro Kawasaki, Keisuke Harigaya, and Ryo Matsuda. Baryon asymmetry, dark matter, and density perturbation from primordial black holes. *Phys. Rev. D*, 89(10):103501, 2014.

[145] Yuta Hamada and Satoshi Iso. Baryon asymmetry from primordial black holes. *PTEP*, 2017(3):033B02, 2017.

[146] Dan Hooper and Gordan Krnjaic. GUT Baryogenesis With Primordial Black Holes. *Phys. Rev. D*, 103(4):043504, 2021.

[147] V. De Luca, G. Franciolini, A. Kehagias, and A. Riotto. Standard model baryon number violation seeded by black holes. *Phys. Lett. B*, 819:136454, 2021.

[148] Misao Sasaki, Teruaki Suyama, Takahiro Tanaka, and Shuichiro Yokoyama. Primordial black holes—perspectives in gravitational wave astronomy. *Class. Quant. Grav.*, 35(6):063001, 2018.

[149] Bernard Carr, Kazunori Kohri, Yuuiti Sendouda, and Jun'ichi Yokoyama. Constraints on Primordial Black Holes. 2 2020.

[150] George Rybicki and Alan Lightman. *Radiative Processes in Astrophysics*. Wiley-VCH, 2004.

[151] N. Aghanim et al. Planck 2018 results. VI. Cosmological parameters. *Astron. Astrophys.*, 641:A6, 2020.

[152] Lars Bergström. Nonbaryonic dark matter: Observational evidence and detection methods. *Rept. Prog. Phys.*, 63:793, 2000.

[153] Gianfranco Bertone, Dan Hooper, and Joseph Silk. Particle dark matter: Evidence, candidates and constraints. *Phys. Rept.*, 405:279–390, 2005.

[154] Mariangela Lisanti. Lectures on Dark Matter Physics. In *Theoretical Advanced Study Institute in Elementary Particle Physics: New Frontiers in Fields and Strings*, pages 399–446, 2017.

[155] Asimina Arvanitaki, Savas Dimopoulos, Sergei Dubovsky, Nemanja Kaloper, and John March-Russell. String Axiverse. *Phys. Rev. D*, 81:123530, 2010.

[156] Lam Hui, Jeremiah P. Ostriker, Scott Tremaine, and Edward Witten. Ultralight scalars as cosmological dark matter. *Phys. Rev. D*, 95(4):043541, 2017.

[157] Wayne Hu, Rennan Barkana, and Andrei Gruzinov. Cold and fuzzy dark matter. *Phys. Rev. Lett.*, 85:1158–1161, 2000.

[158] Vid Iršič, Matteo Viel, Martin G. Haehnelt, James S. Bolton, and George D. Becker. First constraints on fuzzy dark matter from Lyman-α forest data and hydrodynamical simulations. *Phys. Rev. Lett.*, 119(3):031302, 2017.

[159] Mona Dentler, David J. E. Marsh, Renée Hložek, Alex Laguë, Keir K. Rogers, and Daniel Grin. Fuzzy dark matter and the Dark Energy Survey Year 1 data. *Mon. Not. Roy. Astron. Soc.*, 515(4):5646–5664, 2022.

[160] Lam Hui. Wave Dark Matter. *Ann. Rev. Astron. Astrophys.*, 59:247–289, 2021.

[161] Andrei Khmelnitsky and Valery Rubakov. Pulsar timing signal from ultralight scalar dark matter. *JCAP*, 02:019, 2014.

[162] Peter W. Graham, Igor G. Irastorza, Steven K. Lamoreaux, Axel Lindner, and Karl A. van Bibber. Experimental Searches for the Axion and Axion-Like Particles. *Ann. Rev. Nucl. Part. Sci.*, 65:485–514, 2015.

[163] Peter W. Graham, David E. Kaplan, Jeremy Mardon, Surjeet Rajendran, and William A. Terrano. Dark Matter Direct Detection with Accelerometers. *Phys. Rev. D*, 93(7):075029, 2016.

[164] Asimina Arvanitaki, Junwu Huang, and Ken Van Tilburg. Searching for dilaton dark matter with atomic clocks. *Phys. Rev. D*, 91(1):015015, 2015.

[165] Andrew A. Geraci, Colin Bradley, Dongfeng Gao, Jonathan Weinstein, and Andrei Derevianko. Searching for Ultralight Dark Matter with Optical Cavities. *Phys. Rev. Lett.*, 123(3):031304, 2019.

[166] Igor G. Irastorza and Javier Redondo. New experimental approaches in the search for axion-like particles. *Prog. Part. Nucl. Phys.*, 102:89–159, 2018.

[167] Y. V. Stadnik and V. V. Flambaum. Enhanced effects of variation of the fundamental constants in laser interferometers and application to dark-matter detection. *Phys. Rev. A*, 93:063630, Jun 2016.

[168] Luca Di Luzio, Belen Gavela, Pablo Quilez, and Andreas Ringwald. Dark matter from an even lighter QCD axion: trapped misalignment. *JCAP*, 10:001, 2021.

[169] Luca Di Luzio, Belen Gavela, Pablo Quilez, and Andreas Ringwald. An even lighter QCD axion. *JHEP*, 05:184, 2021.

[170] Peter W. Graham and Surjeet Rajendran. New Observables for Direct Detection of Axion Dark Matter. *Phys. Rev. D*, 88:035023, 2013.

[171] Dmitry Budker, Peter W. Graham, Micah Ledbetter, Surjeet Rajendran, and Alex Sushkov. Proposal for a Cosmic Axion Spin Precession Experiment (CASPEr). *Phys. Rev. X*, 4(2):021030, 2014.

[172] A. Wagner et al. A Search for Hidden Sector Photons with ADMX. *Phys. Rev. Lett.*, 105:171801, 2010.

[173] Saptarshi Chaudhuri, Peter W. Graham, Kent Irwin, Jeremy Mardon, Surjeet Rajendran, and Yue Zhao. Radio for hidden-photon dark matter detection. *Phys. Rev. D*, 92(7):075012, 2015.

[174] Stefan Knirck, Takayuki Yamazaki, Yoshiki Okesaku, Shoji Asai, Toshitaka Idehara, and Toshiaki Inada. First results from a hidden photon dark matter search in the meV sector using a plane-parabolic mirror system. *JCAP*, 11:031, 2018.

[175] Haipeng An, Maxim Pospelov, Josef Pradler, and Adam Ritz. Direct Detection Constraints on Dark Photon Dark Matter. *Phys. Lett. B*, 747:331–338, 2015.

[176] Itay M. Bloch, Rouven Essig, Kohsaku Tobioka, Tomer Volansky, and Tien-Tien Yu. Searching for Dark Absorption with Direct Detection Experiments. *JHEP*, 06:087, 2017.

[177] Daniel Carney, Anson Hook, Zhen Liu, Jacob M. Taylor, and Yue Zhao. Ultralight dark matter detection with mechanical quantum sensors. *New J. Phys.*, 23(2):023041, 2021.

[178] Aaron Pierce, Keith Riles, and Yue Zhao. Searching for Dark Photon Dark Matter with Gravitational Wave Detectors. *Phys. Rev. Lett.*, 121(6):061102, 2018.

[179] Marco Fabbrichesi, Emidio Gabrielli, and Gaia Lanfranchi. The Dark Photon. 5 2020.

[180] Hooman Davoudiasl, Gopolang Mohlabeng, and Matthew Sullivan. Galactic Dark Matter Population as the Source of Neutrino Masses. *Phys. Rev. D*, 98(2):021301, 2018.

[181] Jiajun Liao, Danny Marfatia, and Kerry Whisnant. Light scalar dark matter at neutrino oscillation experiments. *JHEP*, 04:136, 2018.

[182] Francesco Capozzi, Ian M. Shoemaker, and Luca Vecchi. Neutrino Oscillations in Dark Backgrounds. *JCAP*, 07:004, 2018.

[183] Guo-Yuan Huang and Newton Nath. Neutrinophilic Axion-Like Dark Matter. *Eur. Phys. J. C*, 78(11):922, 2018.

[184] Yasaman Farzan. Ultra-light scalar saving the 3 + 1 neutrino scheme from the cosmological bounds. *Phys. Lett. B*, 797:134911, 2019.

[185] James M. Cline. Viable secret neutrino interactions with ultralight dark matter. *Phys. Lett. B*, 802:135182, 2020.

[186] Guo-yuan Huang and Newton Nath. Neutrino meets ultralight dark matter: $0\nu\beta\beta$ decay and cosmology. *JCAP*, 05(05):034, 2022.

[187] Eung Jin Chun. Neutrino Transition in Dark Matter. 12 2021.

[188] Marta Losada, Yosef Nir, Gilad Perez, Inbar Savoray, and Yogev Shpilman. Parametric resonance in neutrino oscillations induced by ultra-light dark matter and implications for KamLAND and JUNO. 5 2022.

[189] Abhish Dev, Gordan Krnjaic, Pedro Machado, and Harikrishnan Ramani. Constraining Feeble Neutrino Interactions with Ultralight Dark Matter. 5 2022.

[190] K. Abe et al. Atmospheric neutrino oscillation analysis with external constraints in Super-Kamiokande I-IV. *Phys. Rev. D*, 97(7):072001, 2018.

[191] Gonzalo Alonso-Álvarez and James M. Cline. Sterile neutrino dark matter catalyzed by a very light dark photon. *JCAP*, 10:041, 2021.

[192] R. Acciarri et al. Long-Baseline Neutrino Facility (LBNF) and Deep Underground Neutrino Experiment (DUNE): Conceptual Design Report, Volume 2: The Physics Program for DUNE at LBNF. 12 2015.

[193] B. Abi et al. Long-baseline neutrino oscillation physics potential of the DUNE experiment. *Eur. Phys. J. C*, 80(10):978, 2020.

[194] M. G. Aartsen et al. Measurement of Atmospheric Neutrino Oscillations at 6–56 GeV with IceCube DeepCore. *Phys. Rev. Lett.*, 120(7):071801, 2018.

[195] M. G. Aartsen et al. Search for Nonstandard Neutrino Interactions with IceCube DeepCore. *Phys. Rev. D*, 97(7):072009, 2018.

[196] K. Abe et al. The Hyper-Kamiokande Experiment - Snowmass LOI. 9 2020.

[197] M. Honda, T. Kajita, K. Kasahara, and S. Midorikawa. Improvement of low energy atmospheric neutrino flux calculation using the JAM nuclear interaction model. *Phys. Rev. D*, 83:123001, 2011.

[198] A. M. Dziewonski and D. L. Anderson. Preliminary reference earth model. *Phys. Earth Planet. Interiors*, 25:297–356, 1981.

[199] Patrick Huber, M. Lindner, and W. Winter. Simulation of long-baseline neutrino oscillation experiments with GLoBES (General Long Baseline Experiment Simulator). *Comput. Phys. Commun.*, 167:195, 2005.

[200] Patrick Huber, Joachim Kopp, Manfred Lindner, Mark Rolinec, and Walter Winter. New features in the simulation of neutrino oscillation experiments with GLoBES 3.0: General Long Baseline Experiment Simulator. *Comput. Phys. Commun.*, 177:432–438, 2007.

[201] Ivan Esteban, M. C. Gonzalez-Garcia, Alvaro Hernandez-Cabezudo, Michele Maltoni, and Thomas Schwetz. Global analysis of three-flavour neutrino oscillations: synergies and tensions in the determination of θ_{23}, δ_{CP}, and the mass ordering. *JHEP*, 01:106, 2019.